

# Scanning tunneling microscopy on large bio-molecular systems on surfaces

THIS IS A TEMPORARY TITLE PAGE  
It will be replaced for the final print by a version  
provided by the service academique.

Thèse n. 1234 2017  
présenté xxxxxx 2017  
à la Faculté des Sciences de Base  
laboratoire de sciences à l'échelle nanométrique  
programme doctoral en Physique  
École Polytechnique Fédérale de Lausanne  
pour l'obtention du grade de Docteur ès Sciences  
par

Sebastian Koslowski



acceptée sur proposition du jury:

Prof Cécile Hébert, président du jury

Prof Klaus Kern, directeur de thèse

Dr. Uta Schlickum, co-directeur de thèse

Prof Giovanni Dietler, rapporteur

Prof Alexander Schneider, rapporteur

Prof Axel Enders, rapporteur

Lausanne, EPFL, 2017





There is a theory which states that if ever anyone discovers exactly what the Universe is for and why it is here, it will instantly disappear and be replaced by something even more bizarre and inexplicable. There is another theory which states that this has already happened.

— **The Hitchhiker's Guide to the Galaxy, Douglas Adams**



# Abstract

The ever growing demand for the development of new technologies and materials has led to extensive studies inspired by biological functional complexes. Peptides with their outstanding ability to efficiently self-assemble can express a broad spectrum of intriguing functionalities. A key question in mimicking their assembly and function is the precise understanding of the specific interactions between the contained amino acids on the level of a sub-molecular length scale. An excellent tool to probe samples at these length scales is available with scanning tunneling microscopy (STM) and its operation under the controlled conditions of ultra-high vacuum (UHV) and low temperature. Within this thesis it is demonstrated how high-resolution studies by STM in combination with a controlled sample preparation by electrospray ion beam deposition (ES-IBD) under UHV conditions allows for the structural determination of peptides on surfaces. Furthermore the results presented here contribute to the development of a method capable of directly identifying individual amino acids within a peptide sequence. The structural and electronic properties of molecules on surfaces crucially depend on their interaction with the underlying substrate. Implementing a thin dielectric layer on the metallic surface, electronically decouples molecules from the substrate and enables an unperturbed observation of the molecular electronic structure. In Chapter 2 the properties of hexagonal boron nitride (h-BN) on Rh(111) as decoupling layer are assessed on behalf of the structural and electronic properties of the molecular model system pentacene adsorbed on it. In a second part of this chapter the discovery and the characterization of a new phase of h-BN/Rh(111) is described. In Chapter 3, we gained insight into the properties of amino acids on metal surfaces by utilizing the capability of the STM to probe the structure and the electronic characteristics in high resolution imaging and scanning tunneling spectroscopy (STS). As a second important aspect of this chapter, the modification of STM tips with amino acids is investigated as a method to enhance the structural and electronic resolution. An experimental protocol allowing to adhere amino acids on the STM tip be could developed. Using functional STM tips in STS experiments on amino acids enabled the observation of specific molecular resonances.

An obstacle in investigating large bio-polymers, such as natural peptides, is their high struc-

---

tural complexity and conformational freedom. Therefore the utilization of custom designed synthetic sequences tailored towards a specific property is a good approach. In Chapter 4 studies performed on two synthetic peptide sequences deposited by ES-IBD on an Au(111) surface are discussed. The first sequence assembled in ordered two-dimensional networks. A folded gas-phase conformation could be utilized to rationalize the observed structures in the networks. Subsequently it was shown that the self-assembly behavior of the peptide could be steered towards chain-like assemblies by modifying the sequence at the peptide C-terminal. Using specific amino acid functionalized STM tips a sensitivity towards an amino acid of the same type in the peptide sequence could be observed. Thereby a partial sequencing of the synthetic peptide was enabled.

**Keywords:** Scanning Tunneling Microscopy (STM), Scanning Tunneling Spectroscopy (STS), Electrospray-Ion Beam Deposition (ES-IBD), Ultra-high vacuum (UHV), Peptides, Synthetic peptides, Nanostructures, Self-assembly, Hexagonal Boron-nitride (h-BN)

# Zusammenfassung

Der stetig steigende Anspruch an die Entwicklung neuer Technologien führte zu einer großen Zahl an Studien, welche von funktionalen biologischen Molekülen inspiriert sind. Dabei sind in besonderem Maße Peptide durch ihr breites Spektrum an einzigartigen Funktionalitäten und die besondere Fähigkeit zur Selbst-Assemblierung hervorzuheben. Einer der Kernaspekte in der Nachahmung der darin beteiligten Prozesse, ist das Verständnis der spezifischen Wechselwirkungen der Aminosäuren auf sub-molekularen Längenskalen. Die Technik des Rastertunnelmikroskops (STM) in Verbindung mit der definierten Umgebung des Ultrahochvakuums (UHV) und dem Einsatz tiefer Temperaturen, hat sich als exzellente Methode bewiesen, Proben auf diesen Längenskalen zu untersuchen. Im Rahmen dieser Arbeit wird gezeigt, dass hoch aufgelöste STM Untersuchungen in Verbindung mit einer kontrollierten Probenpräparation mittels Elektrospray-Ionenstrahl Deponierung (ES-IBD) es ermöglichen, die Struktur von Peptiden auf Oberflächen aufzuklären. Des Weiteren tragen die hier präsentierten Resultate zur Entwicklung einer Methode bei, welche es ermöglicht einzelne Aminosäuren in einer Peptidsequenz auf einer Oberfläche direkt zu identifizieren. Die strukturellen und elektronischen Eigenschaften von Molekülen auf Oberflächen hängen maßgeblich von der Wechselwirkung mit der unterliegenden (Metall-) Oberfläche ab. Durch den Einsatz von dünnen dielektrischen Schichten zwischen Metall und Molekül, ist es möglich die molekulare elektronische Struktur zu entkoppeln und somit die ungestörte elektronische Struktur von Molekülen mittels Rastertunnelspektroskopie (STS) zu messen. In Kapitel 2 wird die Eignung von hexagonalem Bornitrid (h-BN) als Entkopplungsschicht auf Rh(111) mittels der strukturellen und elektronischen Eigenschaften von darauf adsorbiertem Pentazen untersucht. In einem zweiten Teil dieses Kapitels wird Beobachtung und Charakterisierung einer neuen Phase von h-BN/Rh(111) beschrieben.

In Kapitel 3 konnten wir durch STM und STS die strukturellen und elektronischen Eigenschaften von verschiedenen Aminosäuren auf Metalloberflächen analysieren und charakteristische Merkmale identifizieren. Ein weiterer Aspekt dieses Kapitels befasst sich mit der gezielten Modifikation der STM Spitze mit Aminosäuren, um die strukturelle und elektronische Auflösung zu erhöhen. Durch den Einsatz solcher funktionaler STM Spitzen war die Beobachtung

---

spezifischer molekularer Resonanzen möglich. Ein Hindernis bei der Untersuchung großer Bio-Polymere, wie etwa natürliche Peptide, ist deren strukturelle Komplexität und konformelle Freiheit. Für Peptide können spezifische Eigenschaften durch synthetische Modellsequenzen mit reduzierter Komplexität modelliert werden. In Kapitel 4 werden die Resultate von Studien an zwei synthetischen Peptidsequenzen präsentiert, welche mittels ES-IBD auf eine Au(111) Oberfläche deponiert wurden. Es wurde gezeigt, dass die Selbstassemblierung des Peptids auf der Oberfläche durch Modifizierung der Sequenz gesteuert werden kann. In einem weiteren Experiment konnte durch den Einsatz von aminosäure-modifizierten STM Spitzen eine spezifische Sensitivität für die Aminosäuren desselben Typs im Peptid erreicht werden. Dies erlaubte eine partielle Sequenzierung des synthetischen Peptids auf der Oberfläche.

**Stichwörter:** Rastertunnelmikroskopie, Rastertunnelspektroskopie, Elektrospray-Ionenstrahl Deponierung, Ultrahochvakuum, Peptide, Synthetische Peptide, Nanostrukturen, Selbstassemblierung, hexagonales Bornitrid

# Contents

<b>Abstract (English/Deutsch)</b>	<b>ii</b>
<b>List of figures</b>	<b>vii</b>
<b>Introduction</b>	<b>1</b>
<b>List of acronymes</b>	<b>1</b>
<b>1 Theoretical and Experimental Background</b>	<b>7</b>
1.1 Theory of scanning tunneling microscopy (STM) . . . . .	7
1.2 Experimental set-up: Homebuilt STM . . . . .	16
1.3 Electrospray ion beam deposition (ES-IBD) . . . . .	19
1.4 Amino Acids and peptides . . . . .	20
<b>2 Pentacene on Different Types of Decoupling Layers</b>	<b>23</b>
2.1 Hexagonal boron nitride (h-BN) on Rh(111) . . . . .	24
2.2 Pentacene on h-BN/Rh(111) . . . . .	28
2.3 Conclusion part I . . . . .	38
2.4 Intercalated carbon h-BN/Rh(111) . . . . .	40
2.5 Conclusion part II . . . . .	55
<b>3 The building blocks of peptides -</b>	
<b>Single amino acids on surfaces</b>	<b>57</b>
3.1 Phenylalanine . . . . .	58
3.2 Tryptophan . . . . .	63
3.3 Arginine . . . . .	68
3.4 Proline . . . . .	71
3.5 Multiple amino acids on Au(111) . . . . .	73
3.6 Conclusion . . . . .	76

## Contents

---

<b>4</b>	<b>Towards sequencing of peptides on surfaces</b>	<b>77</b>
4.1	Model system - WWPPPPWW on Au(111) . . . . .	80
4.2	Modifying the sequence - WWPPPPRR on Au(111) . . . . .	85
4.3	Conclusion . . . . .	102
<b>5</b>	<b>Conclusion and Outlook</b>	<b>105</b>
5.1	Conclusion . . . . .	105
5.2	Outlook . . . . .	107
5.2.1	Combined STM/AFM . . . . .	110
	<b>Acknowledgements</b>	<b>113</b>
	<b>Bibliography</b>	<b>115</b>
	<b>Curriculum Vitae</b>	<b>131</b>



# List of Figures

1	Biomimetic bacterial photosynthetic reaction center complex and its natural counterpart . . . . .	2
2	Schematic of ATP-synthase . . . . .	3
1.1	Schematic description of quantum tunneling . . . . .	8
1.2	Schematic visualization of a STM setup . . . . .	9
1.3	Schematic visualization of STS . . . . .	11
1.4	STM images of PTCDA with various functionalized tips . . . . .	13
1.5	Imaging of molecular orbitals of pentacene with a metallic and a pentacene functionalized STM tip . . . . .	14
1.6	Schematic drawing of the home-built STM set-up . . . . .	16
1.7	STM head and sampleholder . . . . .	17
1.8	UHV suitcase . . . . .	19
1.9	Schematic of ES-IBD . . . . .	20
1.10	Formation of the peptide bond . . . . .	21
1.11	Overview over the 20 canonical amino acids . . . . .	22
2.1	Structure and formation of h-BN . . . . .	24
2.2	DFT models of h-BN/Rh(111) . . . . .	26
2.3	STS on h-BN/Rh(111) . . . . .	27
2.4	Atomic resolution STM topographs of the h-BN/Rh(111) Moiré-pattern. . . . .	28
2.5	Pentacene adsorbed on h-BN/Rh(111) . . . . .	29
2.6	STS of pentacene on h-BN/Rh(111) . . . . .	30
2.7	Spatial mapping of the molecular orbitals of pentacene . . . . .	31
2.8	Tip modification with pentacene . . . . .	32
2.9	Mapping of the molecular orbitals of pentacene with and without pentacene functionalized STM tip . . . . .	32
2.10	Simulation of the DOS of the frontier orbitals of pentacene . . . . .	33

## List of Figures

---

2.11 Energy level diagram depicting the relations between $E_a$ , $E_i$ , $\phi$ and the energies measured in STS for the HOMO and LUMO of pentacene. . . . .	36
2.12 STS measurements of pentacene on various decoupling layers . . . . .	37
2.13 Experimentally determined energies for $E_a$ and $E_i$ of pentacene versus the workfunction of the respective decoupling layers . . . . .	38
2.14 STM topography of IC-h-BN . . . . .	40
2.15 Overview STM topography image of IC-h-BN . . . . .	42
2.16 High resolution STM topography image of h-BN patch surrounded by IC-h-BN	43
2.17 STM image of IC-h-BN acquired in point contact mode . . . . .	43
2.18 Schematic visualization of the location of carbon underneath the IC-h-BN layer	44
2.19 IPS on Ag(111) and FER on Cu(111) . . . . .	45
2.20 FER of h-BN/Rh(111) . . . . .	46
2.21 Line profiles of the energetic position of the FER on h-BN and IC-h-BN . . . . .	47
2.22 $dz/dV$ spectrum of FER on the position of the bright triangle of IC-h-BN . . . . .	48
2.23 Spatial mapping of the FER of IC-h-BN in $dI/dV$ maps . . . . .	49
2.24 Spectrum of the kinetic energy acquired by XPS on a IC-h-BN sample. . . . .	51
2.25 Binding energy of the characteristic elements of a IC-h-BN sample measured by XPS . . . . .	52
2.26 DFT model of IC-h-BN . . . . .	53
2.27 Comparison of experimental data and model of IC-h-BN . . . . .	54
2.28 Pentacene on IC-h-BN . . . . .	54
3.1 Phe on Cu(111) . . . . .	59
3.2 Orientation of Phe trimers . . . . .	60
3.3 $C_{60}$ on Ag(111) . . . . .	61
3.4 Phe on $C_{60}$ /Ag(111) . . . . .	62
3.5 Tryp on Au(111) . . . . .	64
3.6 STS of Tryp on Au(111) . . . . .	65
3.7 STS of Tryp on Au(111) . . . . .	65
3.8 Tryp dimers on Au(111) . . . . .	67
3.9 STS with Tryp functionalized STM tip . . . . .	68
3.10 Arg on Au(111) . . . . .	69
3.11 STS of Arg on Au(111) . . . . .	70
3.12 Proline on Au(111) . . . . .	72
3.13 STS of Proline on Au(111) . . . . .	73
3.14 Tryp, Arg and pentacene on Au(111) . . . . .	74

4.1	Chemical structure of the synthetic peptide with the sequence WWPPPPWW . . . . .	80
4.2	Networks of WWPPPPWW on Au(111) . . . . .	82
4.3	Simulated structure of WWPPPPWW . . . . .	83
4.4	WWPPPPWW dimer on Au(111) . . . . .	84
4.5	Chemical structure of the synthetic peptide WWPPPPRR . . . . .	86
4.6	WWPPPPRR on Au(111) . . . . .	86
4.7	WWPPPPRR dimer . . . . .	87
4.8	Splitting of WWPPPPRR dimer . . . . .	88
4.9	DFT relaxation of WWPPPPRR on Au(111) . . . . .	89
4.10	Simulated STM topography of WWPPPPRR in comparison with experimental data	91
4.11	STS on WWPPPPRR with Arg functionalized tip . . . . .	93
4.12	dI/dV map of Arg state in WWPPPPRR with Arg functionalized tip . . . . .	94
4.13	Simulation of the frontier orbitals of WWPPPPRR . . . . .	95
4.14	Manually summed occupied orbitals for Arg as calculated by DFT based on the structure relaxed on a Au(111) surface in comparison with the experimentally observed DOS at -1.64 V with an Arg functionalized STM tip. . . . .	96
4.15	Determination of the Arg position within WWPPPPRR dimer by acquisition of dI/dV maps with Arg functionalized tip . . . . .	98
4.16	WWPPPPRR chain superimposed with cartoon visualizing its repeating building blocks . . . . .	99
4.17	Topography of WWPPPPRR chain imaged with Ar-functionalized tip . . . . .	101
4.18	Spatial mapping of characteristic STS resonance recorded with proline tip on WWPPPPRR dimer . . . . .	102
5.1	Synthetic peptides with various sequences . . . . .	107
5.2	AT-II deposited on h-BN/Rh(111) . . . . .	109
5.3	Simultaneous STM/AFM measurements of organic molecules on surfaces using a q-Plus sensor . . . . .	111





## List of acronymes

<b>AFM</b>	Atomic force microscopy
<b>Arg</b>	L-Arginin
<b>ATP</b>	Adenosine tri-phosphate
<b>DFT</b>	Density functional theory
$E_a$	Electron affinity
$E_F$	Fermi energy
$E_i$	Ionization potential
<b>ES-IBD</b>	Electrospray ion-beam deposition
$E_{vac}$	Vacuum level
<b>FER</b>	Field emission resonance
$f_{mod}$	Modulation frequency of the reference signal used in a lock-in technique
<b>h-BN</b>	hexagonal boron nitride
<b>HOMO</b>	Highest occupied molecular orbital
<b>IC-h-BN</b>	Intercalated carbon hexagonal boron nitride
<b>LDOS</b>	Local density of states
<b>lHe</b>	liquid helium
$lN_2$	liquid nitrogen
<b>LUMO</b>	Lowest unoccupied molecular orbital
<b>MD</b>	Molecular dynamics
<b>MO</b>	Molecular Orbital
<b>Phe</b>	L-Phenylalanine
<b>SEM</b>	Scanning electron microscopy
<b>STM</b>	Scanning tunneling microscope
<b>STS</b>	Scanning tunneling spectroscopy
<b>Tryp</b>	L-Tryptophane
$U_B$	Bias voltage applied between tip and sample of an STM
<b>UHV</b>	ultra high vacuum
$U_{mod}$	Peak amplitude of the modulation voltage used in a lock-in technique
<b>XPS</b>	X-ray photoelectron spectroscopy
$\phi$	Work function

# Introduction

In 2013 M. Levitt began his Nobel prize lecture with the famous quote “standing on the shoulders of giants”. He was among M. Karplus and A. Warshel awarded with the Nobel prize in chemistry for the “development of multiscale models for complex chemical systems”. Their work in the field of biochemistry and theoretical chemistry significantly contributed to the development of techniques suitable to model and understand large biological systems. With his initial quote Levitt was referring to his predecessors in science, who by their outstanding experimental and theoretical work, such as the discovery of the DNA alpha helix by L. Pauling in 1951 and the determination of the hemoglobin structure by X-ray-diffraction by M. Perutz (Nobel Prize for Chemistry in 1962), laid the foundations of our current understanding of the biological machinery enabling life as we know it. An aim of modern research and development of technology is to understand and mimic the exquisite functionalities that could be observed in the cellular machinery of organisms.

One approach in experimental science, which is currently pursued is the identification of reactive centers in biological complexes and to mimic them in nano-scale experiments by simple organic or metal-organic model systems. An example for such an imitation is shown in Fig.1 for the mimicry of the reactive center of a bacterial photosystem [1–3] with the aid of synthetic chemistry.

This approach of mimicking and implementing specific functionalities using small molecular model systems is especially relevant for surface chemistry, e.g. the basic understanding of catalysis [6–8], chirality [9–11], self-assembly [12–15], molecular electronics [16, 17] and even the development of molecular "machines" capable of specific motion [18, 19].

An important aspect in the development of novel materials is to find ways to efficiently and reproducibly generate specific structures on the nano-scale. In the context of material science, self-assembly can be seen as an efficient and convenient bottom-up fabrication method capable of producing functional supramolecular compounds from simple building blocks [20]. In general self-assembly can be defined as the spontaneous organization of molecules mediated by their mutual non-covalent interaction into ordered structures [21].

As a new approach, the imitation of the outstanding self-assembly capabilities of biological

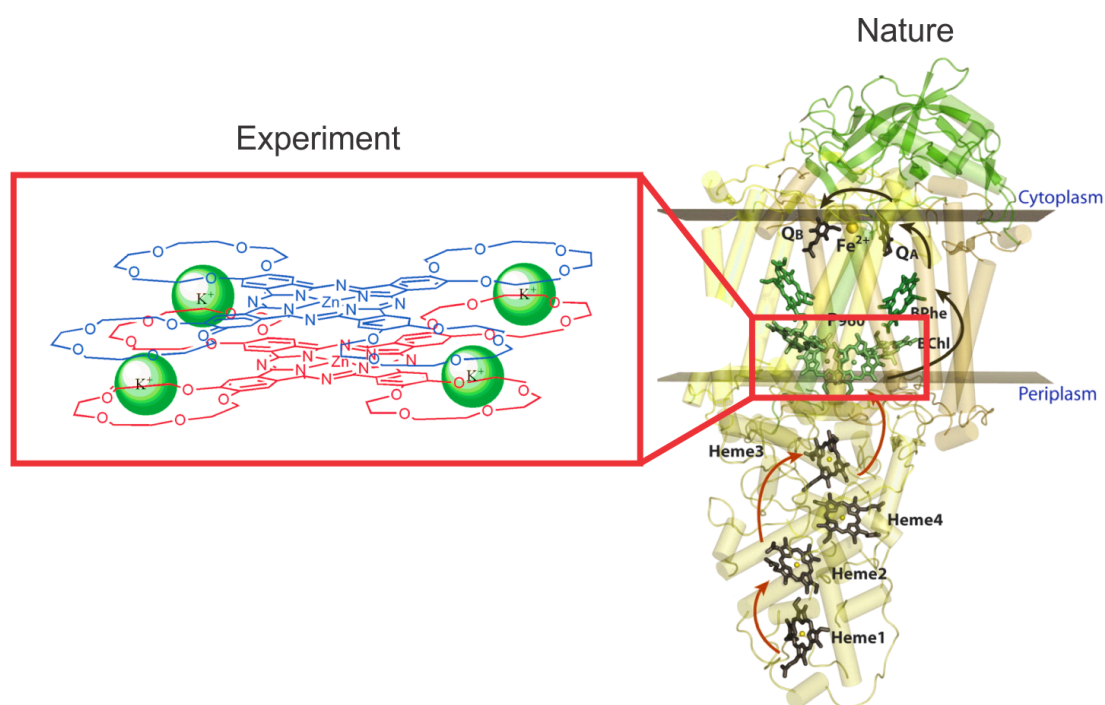


Figure 1 – Experimental realization of the reactive center of a biomimetic bacterial photosynthetic reaction center complex and the natural counterpart as it is found in *Blastochloris viridis*. The images have been adapted from [4] and [5]

structures based on peptides and proteins is an interesting alternative to find ways for the generation of novel materials [22].

Naturally occurring peptides and proteins base on a set of 20 amino acids initially interconnect to linear chains via amino bonds to the so called primary structure of peptides [23]. Due to their high chemical diversity, amino acids can interact via an entire ensemble of noncovalent forces and thus making them prime candidates for building blocks [24] for the generation of self-assembled, functional structures. In a highly hierarchical process governed by the various long- and short range interactions of the individual amino acids and following complex potential landscapes [22], the primary structures are transformed by folding and assembly into secondary and ultimately ternary or quaternary structures. The functionality of the terminal structure is eventually determined by the 3d shape of the fully assembled protein complex.

The ATP synthase protein [25, 26] is a good example for the high level of structural complexity that can be generated via the self-assembly process, which was encoded in an initially linear protein sequence. Its structure is depicted schematically in Fig.2a). One can see in Fig.2b) that the structure exhibits a functionality on the nanoscale closely resembling the one of a machine from the macroscopic world. The ATP-synthase contains a rotating section powered



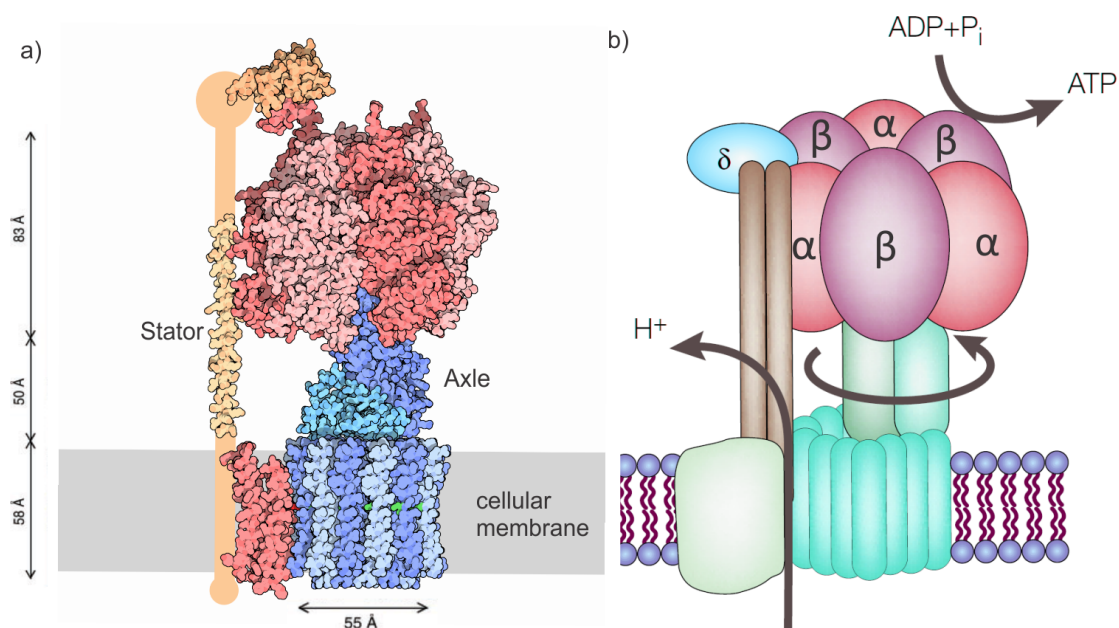


Figure 2 – a) Visualization of the structural model of the ATP synthase protein complex embedded in a cellular membrane (adapted from: Protein-data-base (<https://pdb101.rcsb.org/motm/72>) b) Schematic visualization of the functionality of ATP-synthase (adapted from:[25]).

by the protons moving through the cellular membrane and thus providing the energy for the synthesis of adenosine-tri-phosphate (ATP) [26].

The synthesis of certain building blocks for the self-assembly of functional nano architecture is already possible today. However, the generation of a level of complexity from a linear sequence of amino acids, as shown on the example of ATP synthase, is far beyond the state of the art of modern technology. Transferring these outstanding self assembly capabilities of proteins and peptides to a possible future application in the generation of novel materials and devices requires a fundamental knowledge of the structural properties of the respective building blocks and their constituents [22] as well as the mechanisms involved in the self-assembly process. So far numerous techniques have been used to characterize these properties. The determination of the 3D structure of many proteins could be performed using X-ray scattering techniques [27, 28]. As another important information the sequence of peptides and proteins could be analyzed using for instance the technique of tandem-mass-spectrometry [29, 30]. To study the self-assembly of peptides and to specifically analyze their conformation in solution circular dichroism (CD) [31], nuclear magnetic resonance (NMR) [32] and X-ray scattering techniques (small angle X-ray scattering, wide angle X-ray scattering)[33] were utilized. In the recent years high-resolution atomic-force-microscopy (AFM) and transmission-electron microscopy at

low temperatures (cryo-TEM) allowed for high resolution imaging of peptide nanostructures such as nanofibers and enabled the analysis of their morphology and their size [31, 33].

An important statement M. Levitt made in his Nobel prize lecture is: "Biology is detailed interactions" [34]. He was referring to the specific functionality and the distinct structure of very large protein complexes arising from very detailed interactions of individual amino acids. Not only the theoretical models explaining the structure of proteins were further refined over time but also the experimental techniques were aiming at even smaller scales to access these details of peptide conformations. An interesting approach is to investigate proteins and peptides on a single molecular level with the two key tasks of direct structure determination and identification of the individual amino acids. An excellent tool capable of probing the electronic and structural properties of molecules on surfaces with unprecedented resolution has been scanning-tunneling microscopy (STM) [12, 35]. Together with the upcoming technology of electrospray-ion beam deposition (ES-IBD) a completely new field of research was opened up and it was possible to bring non-volatile bio-polymers such as proteins and peptides into the controlled environment of UHV and thus make them available for studies with high-resolution STM [36]. By STM and ES-IBD, first works investigating the conformation and the assembly of natural peptides and proteins on various surfaces were performed in the recent years [13, 36–38]. A major obstacle for natural peptides and proteins on surfaces is their high complexity and resulting large conformational freedom. This hampers the structural determination and often makes the direct identification of individual building blocks impossible. In order to overcome the high structural complexity and the often complicated isolation of natural peptides, an interesting alternative is the molecular class of synthetic peptide sequences. Synthetic peptides are generated for instance by solid-phase synthesis [39]. This class of molecules offers a powerful toolbox for the straightforward generation of arbitrary structures inheriting specifically tailored properties to mimic the functionality of natural proteins and peptides on a surface. An important aspect, which is still missing in the direct identification of amino acids within the peptide sequences on a surface with nanoscale precision and thereby to directly pinpoint the interactions between the respective amino acids. The work presented within this thesis is touching exactly this aspect of sequencing of peptides on surfaces. In the first chapter an introduction into the theoretical framework and the experimental methods of this work is given. The second chapter describes the investigation of the electronic structure of a simple organic molecule (pentacene) commonly used as a model system to study the organic/inorganic interface [35] and relevant for organic electronics [40] on thin insulating films such as h-BN/Rh(111). In a second part the steered modification of h-BN/Rh(111) facilitating the growth of a novel phase comprised of carbon and h-BN is studied. In chapter 3 STM and scanning tunneling spectroscopy (STS) investigations of various amino acids on

metal surfaces are presented focussing at the individual structural and electronic properties of the amino acids. Most importantly the possibility of utilizing functional STM tips, modified by amino acids adhered at their apex, is investigated to access specific electronic features of the amino acids on the surface.

In a first part of chapter 4 the self-assembly of a synthetic peptide sequence comprised of two amino acid species into regular 2D-networks is investigated by high resolution STM. In a second part the impact on the self-assembly upon modifying the sequence is analyzed. Furthermore, chapter 4 describes the experimental approach of utilizing distinct amino acid functionalized STM tips to enable the identification of individual amino acids within a synthetic peptide sequence.



# 1 Theoretical and Experimental Background

In this chapter a short overview over the essential physical backgrounds and the experimental concept. In addition the experimental setup used is described.

## 1.1 Theory of scanning tunneling microscopy (STM)

Within this work STM is utilized as major experimental methods. In this section the basic physical principles of quantum tunneling and their experimental application in a STM setup are described.

### Quantum tunneling

In classical physics, a potential barrier, e.g. a region of a potential energy above the current energy of the object, defines an impenetrable obstacle for a solid object. The object has a finite probability to be in front of the barrier but never within the barrier, leading to a mere reflection of the object at the barrier. This description holds for so called macro scale objects. For nanoscale objects a potential barrier as described above is no longer a solid obstacle but can be passed in a process known as quantum tunneling [41]. The effect of quantum tunneling was discovered around 1930 to be responsible for alpha decay in radioactive materials [42] enabling the exit of a  $He^{2+}$  nucleus from the potential barrier created by the attractive nuclear force.

Within the framework of quantum mechanics the existence of tunneling can be demonstrated by solving the Schrödinger equation in one dimension for systems with a potential barrier of height  $V$  and width  $d$  as depicted in Fig.1.1. A particle described by a wave-function  $\psi_A$  with an energy  $E < V$  placed in front of the barrier (on the left) has the wave-function  $\Psi_B$  behind the barrier (on the right). The relation between  $\psi_A$  and  $\psi_B$  is described by equation 1.1.

$$\Psi_A \approx \psi_B \cdot e^{\kappa d} \quad (1.1)$$

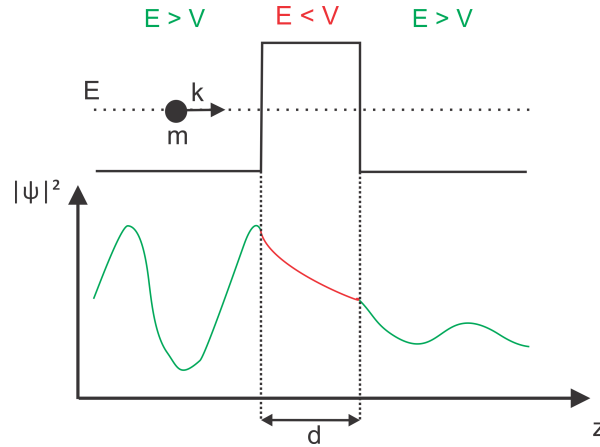


Figure 1.1 – Quantum tunneling through a rectangular barrier with finite height

One can see that the amplitude of the wave-function is decaying exponentially within the barrier governed by the decay constant  $\kappa = \sqrt{2m(V - E)}/\hbar$ , with  $m$  corresponding to the particle's mass and  $\hbar$  being the Planck's constant. This effect is without counterpart in classical physics, where a particle would be restricted to be either on one or the other side of the barrier but never being able to pass it or to be at the barrier. In solid state devices this effect can be exploited by realizing conductive contacts separated by a thin gap or insulating barrier such as tunneling diodes [43].

### Physical principle of STM

The invention of the STM in 1981 by Gerd Binnig and Heinrich Rohrer [44] (IBM labs, Zürich), created a new approach for the direct observation of the atomic structure at the surface of solids. For their invention, they were awarded the Nobel prize in 1986.

Up to this time, microscopy methods either relied on the interaction of the sample with far-field photons (standard optical microscopy), ions (field-ion microscopy) [45] or far-field electrons [46] (scanning electron microscopy (SEM)). The STM however, employs the entirely different principle of quantum tunneling of electrons between a sharp metal tip and a conductive sample surface. Since a tunneling current between two electrodes decays exponentially with the spatial width of the tunnel barrier, typical distances between tip and sample are of the order of a few Å [47]. In order to measure a tunneling current a bias voltage  $U_B$  is applied between tip and sample Fig.1.2. Using piezoelectric positioners, realized for example by stacks of tubular piezoceramics it is possible to position the STM tip in all three spatial coordinates with sub-nanometer precision. A  $z$ -positioner adjusts the tip sample distance (e.g. the spatial width of the tunnel barrier), the  $x$ - and  $y$ - positioners allow to laterally scan over the sample surface.

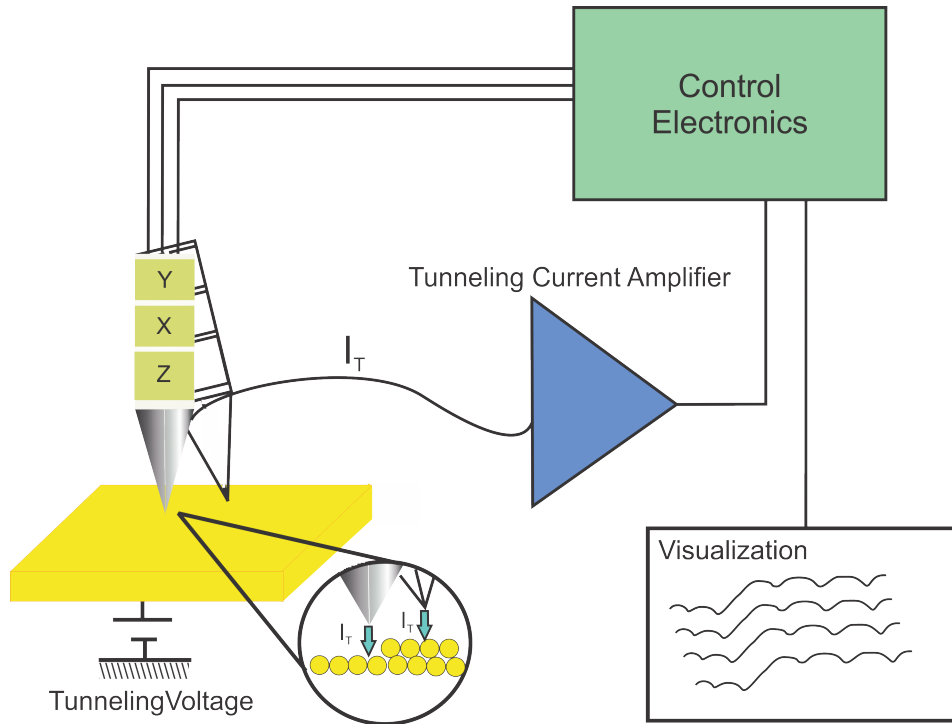


Figure 1.2 – Schematic visualization of a STM setup

A STM can be operated in two basic operation modi, constant current and constant height mode. For the constant current operation, a predetermined tunneling current set-point is set in the control hardware. Subsequently,  $U_B$  is applied and the tip is brought within a proximity to the sample surface so that the desired tunneling current is measurable. While laterally scanning over the sample surface, the measured tunneling current is kept constant by continuously regulating the tip height using the z-piezo positioner. Thereby the tunneling current is amplified (typical amplification factors are  $10^8$  V/A to  $10^9$  V/A) and translated to an analog voltage signal which is the input signal for a negative feedback loop controlling the voltage of the z-piezo positioner. The voltage of the z-piezo positioner is translated to a length value describing the tip displacement and recorded for each coordinate. Thus a map of  $z$  is acquired and will be referred to as STM topography in the following. In constant height operation the STM tip is kept at a fixed distance (feedback loop turned off) to the sample, while laterally scanning over the surface. Without the restriction of the minimal time constant of the feedback loop, high scan frequencies (up to 10 kHz) can be realized. A major limitation of this operation mode is the requirement of an atomically flat sample to avoid crashing the tip into the surface [47]. Constant height operation of the STM can be utilized to investigate samples at constant electric field or fixed tip-sample distance. Furthermore, constant height operation can be used in high resolution imaging to probe the orbital geometry at a specific height.

## Chapter 1. Theoretical and Experimental Background

---

In order to describe the tunneling process in a STM theoretically, Tersoff and Hamman's approximations [48] are a good approach based on perturbation theory in a 3-dimensional model. For a tip which terminates in a single metal atom expressing a radially symmetric (s-wave) electron density and a similar work function  $\phi$  for tip and sample this approach yields for zero temperature:

$$I \propto \frac{2\pi e U_B}{\hbar} \rho_{sample}(E_F) \quad (1.2)$$

$\rho_{sample}(E_F)$  is the local density of states of the sample at the position of the tip apex and  $U_B$  the bias-voltage between tip and sample. Since the tunneling current decays exponentially with distance, about 90% of the current flows through the apex-atom of the tip, leading to the high spatial resolution of the STM.

Further important characteristics of a tunnel-junction are:

- For small values of  $U_B$  the tunnel junction has ohmic behavior ( $I \propto U_B$ ) [47]
- In a first approximation  $I \propto \exp(\sqrt{\phi})$ . Thus the work function can be measured by a variation of  $z$ , since  $d(\ln(I))/dz \propto \sqrt{\phi}$  [49].
- The electronic and geometric characteristics of the STM tip might influence the channels contributing to the tunnel current. This is further discussed in the following sections

Furthermore equation 1.2 and figure 1.2 imply, that STM topographs are to be seen as surfaces of constant local density of states (LDOS). The measured tunneling current always contains mixed contributions of height information and the LDOS and thus should be interpreted carefully. For flat metal surfaces, such as the famous example of the observation of the Au(111) herringbone surface reconstruction [50] or flat lying molecules [35] the interpretation of the STM topography is straight forward. Examples for STM data, where electronic effects influence the observed topographic information and thus cannot be interpreted in a straight forward manner, are for instance standing wave patterns of surface states [51] or inside nano-scale structures, such as the famous "quantum-coral" [52]. In these cases, effects such as the confinement of electron surface states creates additional features observable in STM topography, which do not originate from a variation in the position of the surface atoms.

Also STM topography acquired with non-metallic STM tips has to be treated in a more careful way. This will be discussed in the following sections in more detail.



### Scanning tunneling spectroscopy (STS)

In order to obtain a full description of the tunnel junction in a STM, one has to take the tip and the sample DOS into account. This is schematically visualized in Fig.1.3. One can see that the Fermi levels on both sides of the vacuum barrier are shifted with respect to each other due to the applied  $U_B$ . In the depicted example a positive bias is applied to the tip, causing electrons to tunnel from the sample into unoccupied states of the tip.

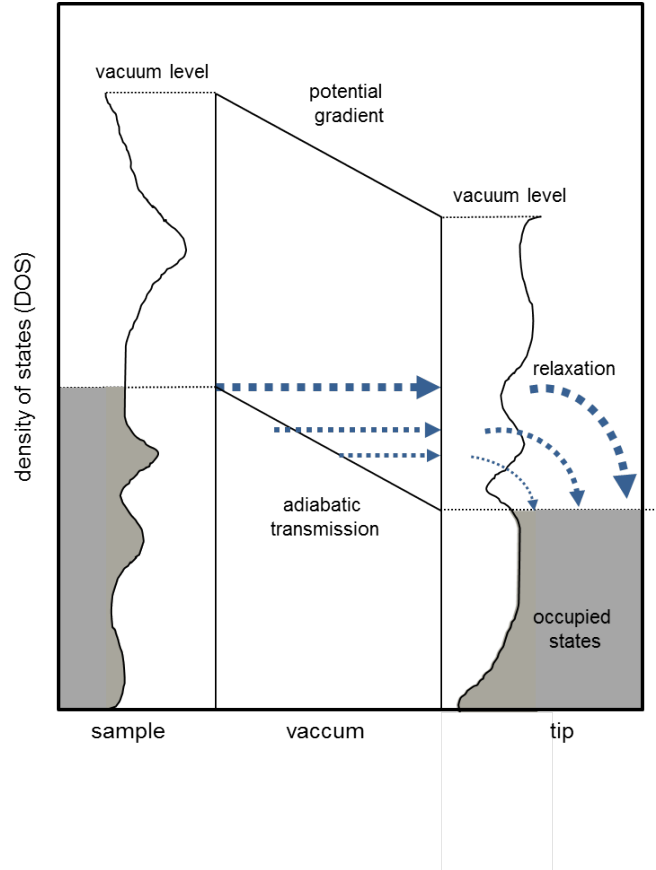


Figure 1.3 – Schematic visualization of the principle of tunneling in a STM tunnel junction from sample to tip.

Using Bardeen's approach [53] one can find an expression for the total current by integrating over the entire DOS of tip and sample (Equation 1.3) between  $E_F$  and  $U_B$ ,

$$I = \frac{2\pi e}{\hbar} \sum_{\mu, \nu} f(E_\mu) [1 - f(E_\nu + eV)] |M_{\mu\nu}^2| \delta(E_\mu - E_\nu), \quad (1.3)$$

where  $f(E)$  is the distribution function of the states indicated with  $\mu$  and  $\nu$  of tip and sample and  $E_\mu$  and  $E_\nu$  the electrochemical potentials on both sides of the junction. The  $\delta$ -function

limits the description to elastic tunneling processes.  $M_{\mu\nu}$  is the so called transition matrix element and is determined by the overlap of the wavefunctions of tip and sample ( $\psi_\mu$  and  $\psi_\nu$ ):

$$M_{\mu\nu} = \frac{\hbar^2}{2m_e L} \int_S dS (\psi_\mu^* \nabla \psi_\nu - \psi_\nu \nabla \psi_\mu^*) \quad (1.4)$$

For the approximation of small  $U_B$  and a constant DOS of the tip it is possible to derive a relation between the differential conductance and the DOS of the sample to:

$$\frac{dI}{dV} \propto \frac{2\pi e}{\hbar} \rho_{sample}(E_F + eV) \quad (1.5)$$

The limitations for the maximal values of  $U_B$  usually are determined by factors like the stability of the tip and the investigated system and the workfunction  $\phi$  of the sample. For energies greater than  $\phi$  the measurement does no longer take place in the tunneling but in the field-emission regime. As equation 1.5 implies, the measurement of the differential conductance in a STM gives direct access to the DOS of the sample at an energy which corresponds to  $U_B$  with respect to the Fermi energy. Within the actual experiment the differential conductance ( $dI/dV$ ) can be obtained by directly differentiating an  $I(V)$  curve. A major drawback of this method is a bad signal-to-noise ratio. A better way, is the direct acquisition of the differential conductance using a lock-in technique [47]. A small periodic voltage (in the mV range or below) is superimposed with  $U_B$  and used as a reference signal. A modulation frequency above the bandwidth of the feedback loop is chosen to not interfere with the z-feedback. Then  $U_B$  is ramped within a previously defined window, while the  $dI/dV$  is recorded. The result is  $dI/dV$  as a function of  $U_B$ . Defined states, such as the surface states of certain (111) surfaces of noble metals [54] or molecular orbitals [55] appear as steps or peaks in the  $dI/dV$  curves. Apart from localized scanning tunneling spectroscopy (STS), the DOS can also be mapped out spatially giving a powerful tool to directly image the spatial distribution of specific states such as the spatial extension of molecular orbitals [35]. Thus the frontier orbitals, the highest occupied molecular orbital (HOMO) and the lowest unoccupied molecular orbital (LUMO), of molecular species are directly accessible.

### STM with functionalized tips

In order to enhance the resolution in a STM, that can be achieved with an atomically sharp apex of a metal tip, a well established approach is the application of functional STM tips generated by the controlled decoration of the tip apex with small atoms or molecules [56]. Initial works by Eigler et al. [57] dealt with the manipulation of small atomic and molecular species such as

Xe. In 1998 Bartels et al. [58] first discussed the concept of experiments with functionalized tips by picking up CO from a Cu(111) surface and performing STS measurements with a CO decorated tip. For a broad variety of small atoms and molecules attached to STM tips, remarkable resolutions upon imaging flat lying organic molecules such as PTCDA could be achieved [56]. Especially noted should be here the case of  $H_2$  modified STM tips leading to very high spatial resolutions.  $H_2$  adsorbed on cold STM junctions was studied by Gupta et al. in 2005 [59] and used for high resolution imaging in 2008 by Temirov et al. [60].

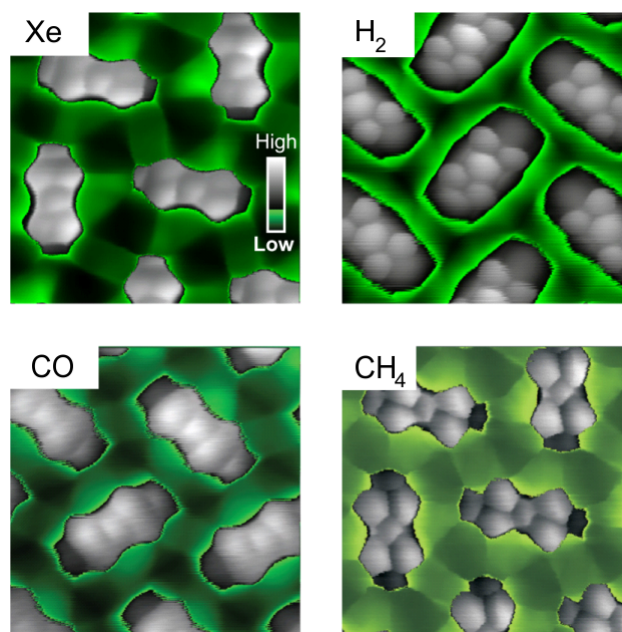


Figure 1.4 – High resolution constant height STM images of PTCDA utilizing various functional tips (modified from: Wagner, Prog Surface Science 2015 [56])

High resolution imaging was also reported for Xe [61], CO [61] and  $CH_4$  [61]. The molecules used for tip functionalization could be transferred in a reproducible way by setting  $U_B$  to specific voltages (depending on the molecular species to be picked up) and gradually approaching the STM tip to the surface until a jump in the tunneling current is noted. Examples for STM images with various functional STM tips are depicted in Fig.1.4. It should be noted, that this is not possible for  $H_2$  since it is not possible to directly image it in a STM. The tip decoration process in this case has more statistical character. One can see that these decorated tips lead to STM images closely resembling the actual chemical structure of the investigated molecule and thus not being limited to the mere observation of extended molecular orbitals.

Although not understood completely up to now, it is assumed that the mechanism responsible for the increased resolution are forces acting on the molecule adsorbed at the tip apex. These forces arise due to pauli repulsion between the sample surface and the adsorbed molecule[56].

The adsorbed molecule is not attached in a fixed geometry to the STM tip but rather possesses some degrees of freedom. While scanning over the sample, the molecule at the tip always tries to reside in a minimum of the surface potential created by the corrugation of the surface. Thus the adsorbed molecule is slightly displaced in relation to the tip and can act as force sensor. This effect could be shown by measuring force-curves in non-contact atomic force microscopes (nc-AFM) with decorated tips [62]. It has to be noted, that the molecule on the tip does not purely act as force sensor, but also as electronic transducer modifying the DOS of the tip near the Fermi level. By this, also STS measurements are affected. Alternative approaches utilizing functional STM tips do not aim at maximizing structural resolution but rather enhancing specific electronic states. Good examples for this are the results presented by Kelly et al. in 1996 [63] on the imaging of the electronic scattering on defects with  $C_{60}$  functionalized tips and the imaging of molecular orbitals (MO) of pentacene on a NaCl-layer by Repp et al. in 2005 [35].

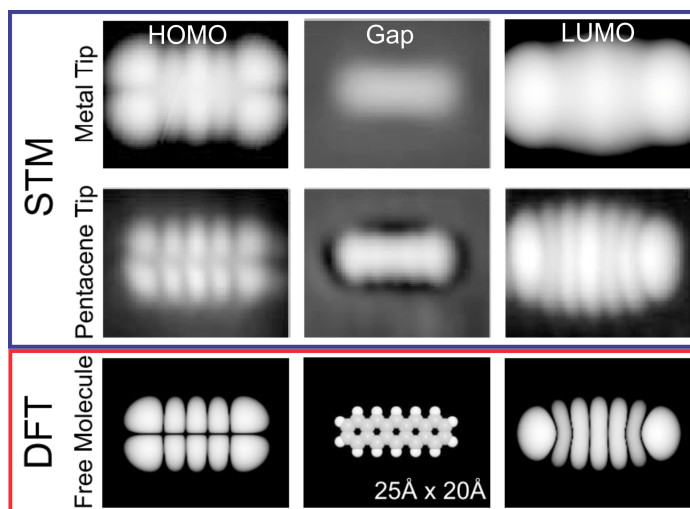


Figure 1.5 – Imaging of molecular orbitals of pentacene on NaCl(100)/Cu(111) with a metallic and a pentacene functionalized STM tip(modified from: Repp, PRL 2005 [35])

It was shown that the application of a pentacene decorated STM tip greatly enhances the resolution for the MO of a pentacene molecule on the surface in comparison to a metal tip. This is depicted in Fig.1.5. The pentacene functionalized STM tip is capable of imaging the structure of MOs of pentacene in close resemblance to the structure obtained by DFT calculations for free molecules. The studies were performed on a thin insulating NaCl layer with adsorbed pentacene molecules. As described in the previous section Tersoff and Hamann stated, that for STM tips exhibiting an s-wave character the acquired topography images resemble the local DOS corresponding to the modulus squared of the sample wavefunctions [48]. However for a STM tip with p-wave character the theoretical work of Chen [64][65] stated, that the

### **1.1. Theory of scanning tunneling microscopy (STM)**

---

resulting STM image corresponds to the spatial derivative of the sample wavefunctions. This was experimentally proven by Gross et al. [66] by imaging the frontier orbitals of pentacene with s- and p-wave STM tips. The increased resolution of p-wave tips, such as pentacene and CO-tips, for the imaging of the frontier MOs of planar organic molecules with closely spaced nodal planes was explained by the high lateral gradient of the wavefunction.

### 1.2 Experimental set-up: Homebuilt STM

The principles described in the previous sections were realized in a home-built STM set-up operating at 5 K in ultra-high vacuum (UHV) which was used to perform the experiments within this work. A schematic 3D-drawing of the set-up is depicted in Fig.1.6. The utilized UHV chamber is divided in two major parts. A preparation chamber and an individual STM chamber. The preparation chamber includes equipment for in-situ sample preparation, such

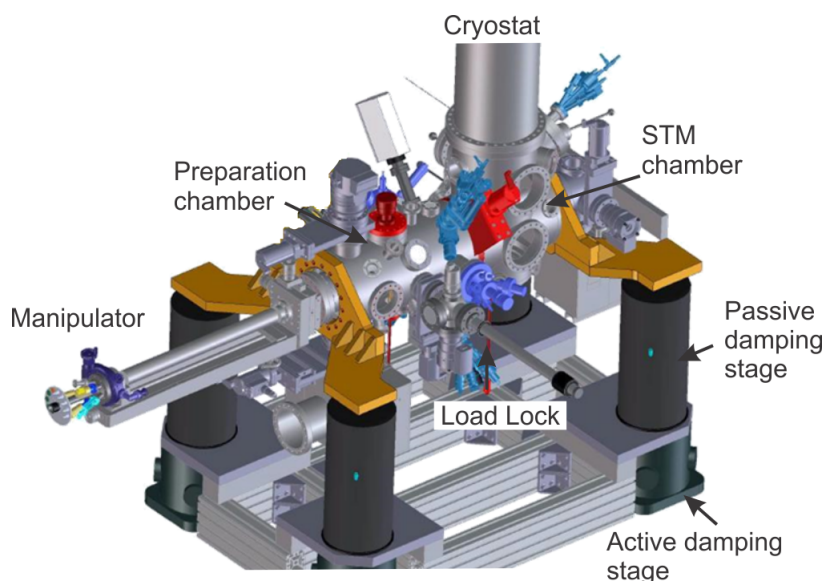


Figure 1.6 – Schematic drawing of the home-built STM set-up with its major components indicated.

as a sputter gun operable with various gases (Type: Specs IQE 11/35), a portable filament for electron-beam heating (Home-built), Mass-Spectrometer (Type: Pfeiffer QMG 220 M3, Prisma Plus) for residual gas analysis and a 4-fold molecular evaporator (Dodecon) for the direct sublimation of volatile molecular species in UHV. Furthermore the preparation chamber is connected to a small load-lock chamber offering a fast way of introducing samples into the UHV. The preparation chamber is pumped by a combination of turbo-molecular pumps (Type: Pfeiffer HiPace 300, Pfeiffer HiPace 80) and an ion-pump (Type: Varian Diode and StarCell), reaching a base pressure of approx.  $2 \cdot 10^{-10}$  mbar.

## 1.2. Experimental set-up: Homebuilt STM

The STM chamber, usually separated by a UHV-valve from the preparation chamber, contains a liquid nitrogen( $lN_2$ )/liquid helium( $lHe$ ) bath cryostat (Type: Cryovac) and the home-built STM head attached to it. The vacuum in this UHV chamber is maintained by a ion-pump and the pumping speed of the cryostat acting as a cryo pump. The internal design of the STM head and its interface with the cryostat is depicted in Fig.1.7

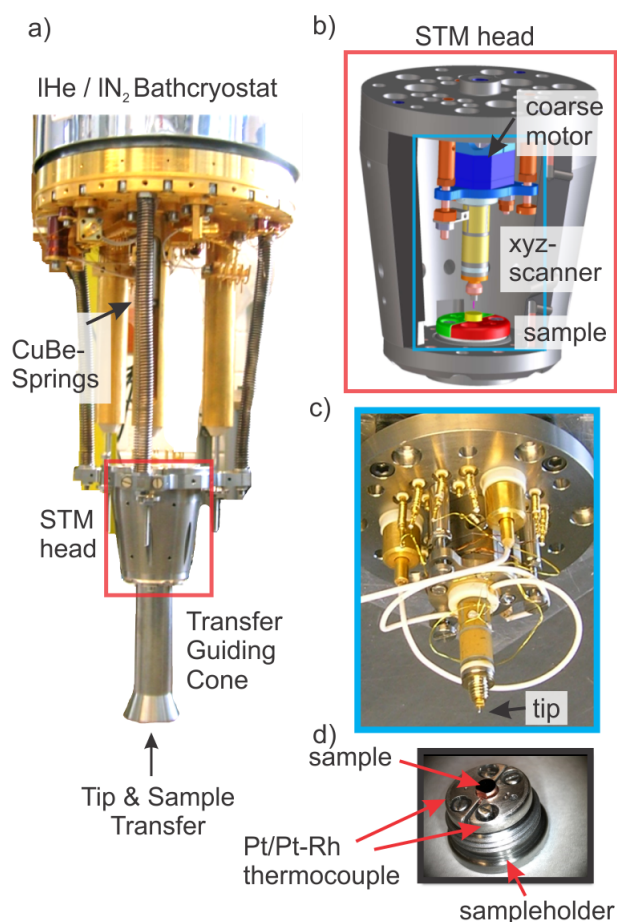


Figure 1.7 – a) STM head and interface to lHe-bathcryostat. b) Schematic drawing of the internal design of the STM head and photograph of the actual STM assembly (c). d) Typical sample on sampleholder.

The STM head is based on a design principle described by Assig et al. [67]. The exchangeable STM tip and the sample are introduced to the STM head from below. The scanner assembly consists of a z-coarse approach realized by a slip-stick type nano-positioner (Attocube, ANPz51eXT/LT/UHV) with a travel range of 5 mm and a tubular piezo scanner providing fine-positioning of the tip in x-, y- and z-direction (c.f. Fig.1.7b)). In Fig.1.7c) a photograph of the assembly of the coarse motor, the scanner tube and the STM tip is depicted. Typically Pt-Ir or W tips were applied within the scope of this work. Pt-Ir tips were cut from UHV grade

## Chapter 1. Theoretical and Experimental Background

---

wire under ambient conditions. W tips were prepared by electro-chemically etching in NaOH using a three electrode setup and a potentiostat. The so prepared tips were assembled into a tip assembly consisting of the tip itself, a Cu-tube with an outer thread fixing the tip and a tip holder with a banana plug acting as a carry and electrical interface. The tip assembly can be introduced to the UHV via the load lock and in-situ introduced to the STM head.

The sample-assembly (Fig.1.7d)) consists of a circular sampleholder, with an outer thread to fix the sample in the manipulator or the STM head. The sample itself is a hat-shaped monocrystalline metal sample (Diameter (bottom): 6.2 mm, diameter (top): 4.2 mm, height: 5.5 mm) with a polished surface oriented in a specific crystal orientation. The sample is fixed by two metal-plates, one platinum and the other one a platinum-rhodium alloy. These plates are a thermocouple type S used to monitor the sample temperature. In order to maximize the signal-to-noise ratio of the STM, the set-up provides three damping stages. The first one is realized with active piezoelectric feet, carrying the entire set-up. As a second stage passive air dampers are used. As a third stage the STM head itself is suspended on damped Cu-Be-springs, while STM is in operation. The STM is operated using a Nanonis RC4 (Specs) control electronics.

### **Vacuum suitcase**

In order to extend the possibilities for sample preparation and characterization and maintain the advantage of the controlled environment of UHV, a UHV-suitcase can be attached to the load lock of the preparation chamber. The applied suitcase (Ferrovac) was equipped with a magnetic manipulator compatible to the sample holder design utilized in the 4K STM. A schematic drawing and a photograph of the employed suitcase attached to the load-lock of the UHV chamber is depicted in Fig.1.8.



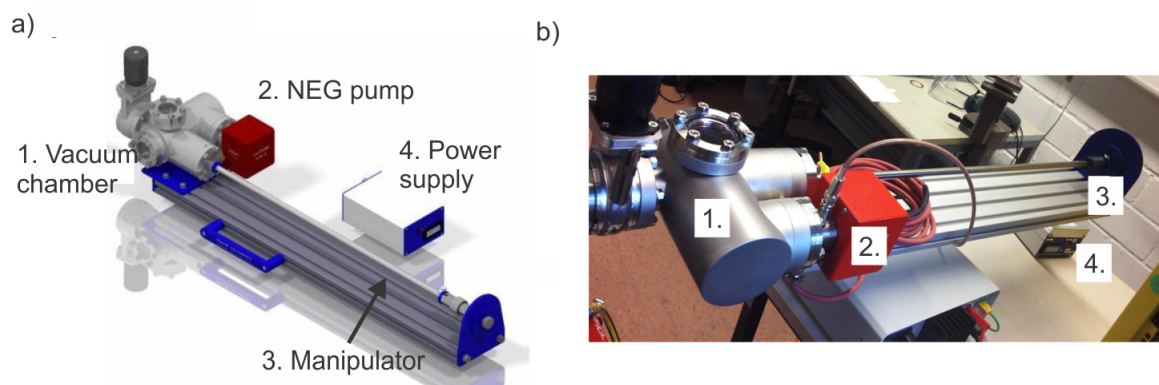


Figure 1.8 – a) Schematic 3D visualization of the utilized UHV suitcase and its main components. b) Photograph of the utilized suitcase. The numbering corresponds to the one used in a).

This allows for fast and easy transfer of samples to and from the preparation chamber to other UHV set-ups, while maintaining a constant base pressure of approx.  $2 \cdot 10^{-10}$  mbar. The UHV suitcase is equipped with a small UHV-chamber, which is pumped by a compact Ion-Getter pump (NEG pump (NexTorr)) and powered by a portable power-supply lasting for several days without direct power connection. Currently the suitcase design is modified to contain a small liquid nitrogen reservoir, which allows for sample transfer at low temperatures (100 K).

### 1.3 Electrospray ion beam deposition (ES-IBD)

In an all UHV sample preparation process a common limitation is the restriction to small volatile molecular systems, which can be brought to the sample surface by thermal sublimation, for instance in a molecular evaporator. Especially when dealing with large non-volatile molecular systems, such as peptides an alternative way for the sample preparation has to be found, since they tend to fragment or undergo chemical reaction before reaching sublimation temperature [68].

One way is to prepare the sample ex-situ by for example dropcasting, causing an exposition of the sample to ambient conditions and relatively poor control over purity and coverage. A good alternative is electrospray ion beam deposition (ES-IBD) in combination with UHV preparation techniques of samples. The electrospray ionization (ESI) method was developed by John Fenn [69] and awarded with a Nobel prize in chemistry 2002. ESI is a powerful technique, which allows to bring charged molecular systems from liquid to gas-phase in a very gentle way [38]. This technique does not pose any restriction to the molecular systems in terms of mass or volatility, the only limitation is the solubility in any solvent [70].

Once the dissolved molecules have been extracted from the solution and turned into a beam

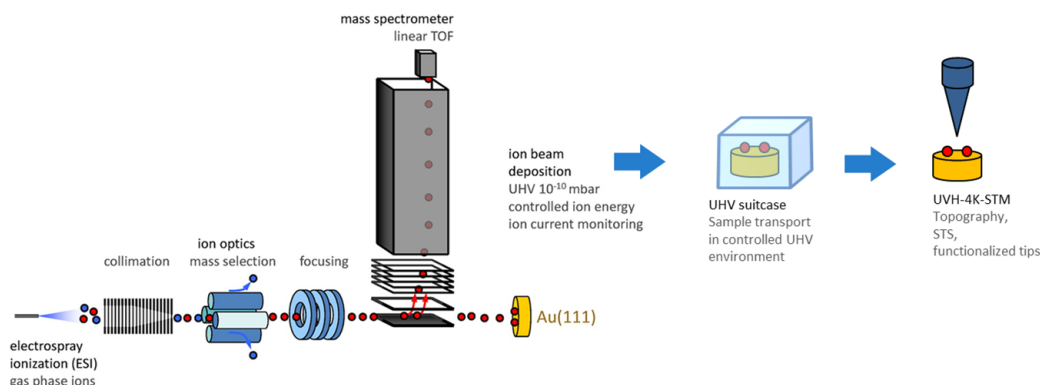


Figure 1.9 – Schematic visualization of a sample preparation under continuous UHV conditions at the ES-IBD setup with consecutive transfer to a 4K-UHV STM via a UHV-suitcase (modified from: [36]).

of molecular ions by means of dispersing them under the influence of a high electric field, they can be analyzed in a mass spectrometer giving access the structure and composition of the molecules. For peptides, this was demonstrated with a determination of their sequence [70]. Employing suitable ion-optics, the molecular ions can be guided and deposited towards a sample surface in UHV. In the set-up utilized in this work the ion-beam is guided through six differentially pumped chambers. By using RF-quadrupole ion optics and electrostatic lenses the ions are mass-selected and can be guided into a time-of-flight mass-spectrometer for further analysis (Fig.1.9). By applying a deceleration voltage with respect to the sample surface, the molecular ions can be "soft-landed" avoiding fragmentation upon the impact [38].

In the actual experiment as it was performed in this work the samples, e.g. atomically flat metal surfaces, were prepared under UHV conditions. A vacuum suitcase was then utilized to transfer the sample under UHV conditions to the ES-IBD setup. After completing the deposition process, the sample was moved back to the 4K STM in a similar way. By this, the purity of the sample could be controlled and guaranteed.

### 1.4 Amino Acids and peptides

Amino acids are a class of biologically relevant chiral, organic compounds which mainly contain an amine- ( $-NH_2$ ) and a carboxyl- ( $-COOH$ ) group as well as a functional residue. A general structure of an amino acid is depicted in Fig.1.10 a). In total over 500 amino acids are known [71] but among them only 20, the so called canonical or proteinogenic amino acids, are encoded in the genetic code for the production of proteins and peptides. All of these canonical amino acids are L-amino acids. In biology amino acids play a crucial role as the building blocks of peptides and proteins. As shown in Fig. 1.10b) amino acids can condensate upon

subtraction of a water molecule to a linear peptide sequence. Sequences of up to 50 amino acids are referred to as peptides, larger sequences are generally classified as proteins. This linear sequence starting from an N-terminal (e.g. the leftover amino group of the first amino acid in the sequence) and terminating in the so called C-terminal (e.g. the residual carboxylic group of the terminal amino acid in the sequence) is referred to as the primary structure. The principal chain of peptide bonds is the peptide backbone.

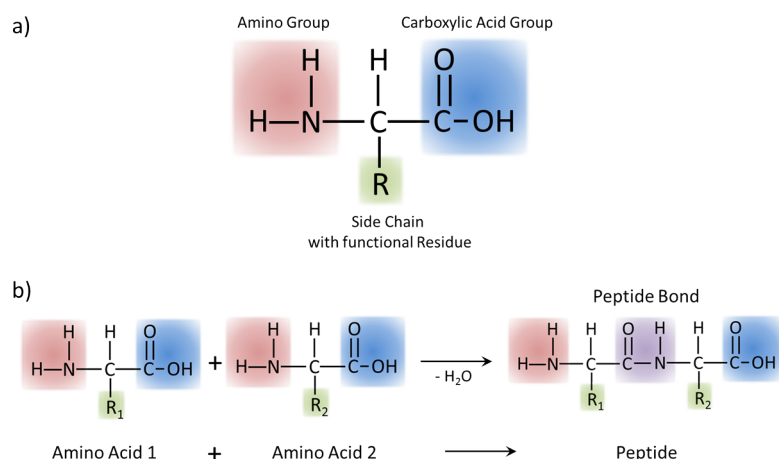


Figure 1.10 – a) General chemical structure motif of an amino acid b) Formation of a peptide by condensating two amino acids and interconnecting them with a peptide bond

In a next step, the three dimensional conformation of the peptide backbone develops by the formation of hydrogen bonds in between amine hydrogens and carbonyl oxygen atoms of the peptide backbone. The conformation can be described by the dihedral bonding angles in a so called Ramachandran plot [72] making it possible to evaluate energetically favorable bonding angles for a given peptide sequence. Two common examples for secondary structures are the  $\alpha$ -helix and the  $\beta$ -sheet. In this step also the steric properties of the individual amino acids is of importance as they can inhibit folding or turning (bulky amino acids). In a third step, the interaction of the individual amino acid residues defines the overall three dimensional shape of the protein. Among the 20 canonical amino acids a broad variety of chemical characteristics, ranging from hydrophobic to polar is present defined by the amino acids individual moieties (Fig.1.11). These properties become of great importance within the peptide sequence, by defining specific interaction between the individual building blocks. Amino acids, such as arginine and glutamic acid are polar and thus can interact via hydrogen bonding and polar interactions. Aromatic and non-polar amino acids, such as phenylalanine mainly interact through dispersive forces (e.g. van der Waals forces). Furthermore the peptide structure is stabilized by salt-bridges and disulfide bonds. It should be noted that the formation of

## Chapter 1. Theoretical and Experimental Background

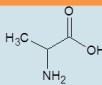
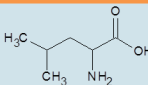
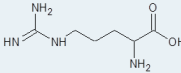
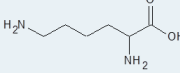
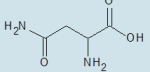
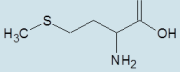
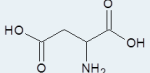
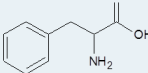
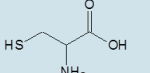
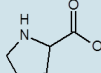
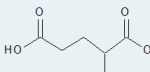
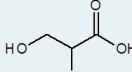
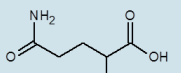
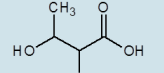
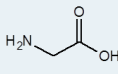
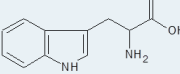
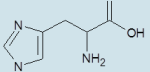
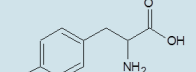
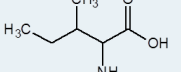
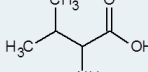
Amino Acid	Structure	Nature	Amino Acid	Structure	Nature
L-Alanine Ala (A)		Hydrophobic Aliphatic	L-Leucine Leu (L)		Hydrophobic Aliphatic
L-Arginine Arg (R)		Hydrophilic Basic (+)	L-Lysine Lys (K)		Hydrophilic Basic (+)
L-Asparagine Asn (N)		Polar Neutral	L-Methionine Met (M)		Hydrophobic Aliphatic
L-Aspartic Acid Asp (D)		Hydrophilic Acidic (-)	L-Phenylalanine Phe (F)		Hydrophobic Aromatic
L-Cystein Cys (C)		Polar Can form disulfide bond	L-Proline Pro (P)		
L-Glutamic Acid Glu (E)		Hydrophilic Acidic (-)	L-Serine Ser (S)		Polar Neutral
L-Glutamine Gln (Q)		Polar Neutral	L-Threonine Thr (T)		Polar Neutral
Glycine Gly (G)			L-Tryptophan Trp (W)		Hydrophobic Aromatic
L-Histidine His (H)		Hydrophilic Basic (+)	L-Tyrosine Tyr (Y)		Hydrophobic Aromatic
L-Isoleucine Ile (I)		Hydrophobic Aliphatic	L-Valine Val (V)		Hydrophobic Aliphatic

Figure 1.11 – Overview over the 20 canonical amino acids and their respective chemical characteristics

a specific ternary structure arises by the interplay with the native environment, e.g. an aqueous solution governing the orientation of hydrophilic and hydrophobic moieties. In a superordinate step multiple ternary structures can assemble to the quaternary structure and thus generate a unit with a specific biological function such as the hemoglobin heterotetramer [73]. This process, known for proteins is referred to as folding [23]. In the context of STM experiments amino acids and peptides/proteins became of great interest in the recent time, because of their outstanding functionalities and their biologic relevance. A broad variety of studies were performed from single amino acids, like Cysteine [74] and small peptides as diphenylalanine [75] to big proteins as Cytochrome-C [36].

## 2 Pentacene on Different Types of Decoupling Layers

A key objective in many studies when investigating individual molecules with STM is the observation of their molecular orbitals (MO). First studies performed by Ohtani et al. on benzene on Rh(111) [76] and by Lee et al. [77] on alkylcyanobiphenyl on graphite discussed their results in terms of the influence of molecular orbitals. One obstacle in the observation of molecular species adsorbed on conductive substrates is the interplay between the reactivity of the substrate and the observation of the unperturbed electronic structure of the molecules. Highly reactive substrates might facilitate the observation of individual isolated molecules as it was demonstrated for Cu-phthalocyanine on Cu(100) by Lippel et al. [78]. The strong interaction with the electron bath of the metal substrate however broadens the discrete molecular levels and furthermore due to hybridization with the substrate the levels are shifted and mixed and thus multiple orbitals can contribute to the STM contrast as observed in the experiment [79].

A solution to this problem was proposed by utilizing thin insulating films as spacer layers (decoupling layers) between the metallic substrate and the molecular adsorbate in combination with low temperature STM [35, 80]. These layers only have little DOS near the Fermi level and it has been shown that already layers of the thickness of a few atoms provide sufficient electronic decoupling of the molecule from the substrate to enable the observation of the unperturbed molecular DOS in STS. It was shown that examples for suitable decoupling layers are, amongst others, alkali halides like NaCl [81][80] and oxides like  $Al_2O_3$  [82][83]. A very prominent example for the observation of unperturbed MO was shown by Repp et al. for pentacene on a NaCl layer deposited on a Cu(111) surface[35]. Further experiments on naphthalocyanine on NaCl/Cu(111) and RbI/Cu(111) enabled the observation of a current-induced hydrogen tautomerization by inelastic scanning tunneling spectroscopy (IETS) [84].

## 2.1 Hexagonal boron nitride (h-BN) on Rh(111)

Although thin insulators enable the observation of electronic features of adsorbed molecules and atoms in STS a common drawback for many insulating layers is their low capability to immobilize adsorbates. This leads for example to increased diffusion and thereby causing clustering or manipulation of molecules during the measurement [85]. In order to overcome these peculiarities a considerably increased effort in the sample preparation needs to be undergone involving most commonly a deposition at low temperatures to limit the diffusion length of molecular adsorbates [35].

An interesting approach here is to exchange flat spacer layers by such layers providing intrinsic features, which act as diffusion barriers for molecules. It was shown by Dil et al. in 2008 [86], that a surface with such properties can be realized by growing a mono-atomic layer of h-BN on Rhodium (111) (Rh(111)). It was possible to immobilize molecules at room-temperature (Cu-Pthalocyanine) and Xe atoms (below 81 K). This was explained by circular dipole-rings formed at the outer rims of the h-BN valleys acting as trapping potential for the adsorbates. Additionally h-BN is an excellent dielectric with a band gap of  $\approx 6$  eV [87] and close structural relation to graphene [88] making it an interesting candidate for device fabrication. h-BN can be grown on various transition metal surfaces (Cu [89], Ir [90], Ag [91], Pt [92], Ni [93], Pd [92], Rh [94]) in a chemical vapour deposition (CVD) process, which utilizes the heated metal surface as catalyst. Unless high partial pressures of the precursor molecule borazine ( $(\text{HBNH})_3$ ) are applied [88], the growth process of h-BN grows is self-terminating and thus limited to one monolayer. The reaction from  $(\text{HBNH})_3$  to h-BN follows the reaction depicted schematically in Fig. 2.1.

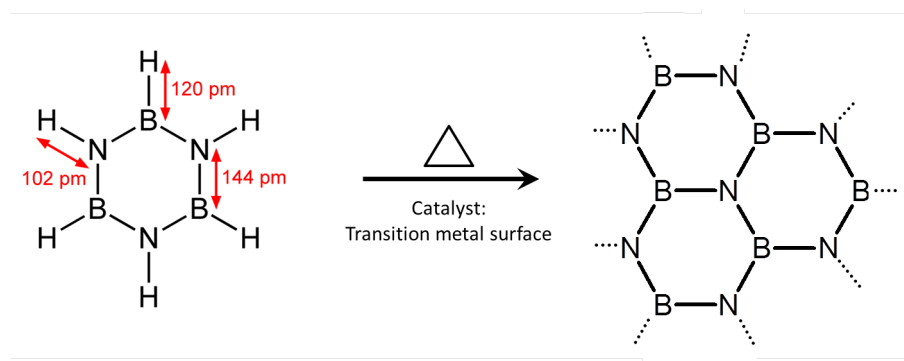


Figure 2.1 – Structural formula of the h-BN precursor borazine  $(\text{HBNH})_3$  (left) and the reaction pathway leading to h-BN (right).

Depending on the underlying metal-substrate, the atomic registry and the interaction strength between the h-BN superstructure and the metal, the resulting topography of the surface can

vary. The observed h-BN Moiré pattern range from topographically flat as for h-BN/Ni [95], merely electronically corrugated as for h-BN/Cu(111) [89] to a buckled superstructures as it was reported for h-BN/Rh(111) [86].

### **h-BN on Rh(111): Sample preparation and structure observed by STM**

A clean Rh(111) substrate was prepared by alternating bombardment of the surface with accelerated  $Ar^+$ -ions (sputtering) and heating cycles (annealing). A total ion current of about  $1-3\mu A$  and a kinetic energy of the ions of 1.2 keV was used. Typical sputter times were 30 min. Subsequently the sample was annealed to  $800^\circ C$  for 5 min to restore an atomically flat crystal surface. As an additional cleaning step to the standard procedure the sample was initially sputtered with  $Ar^+$  ions ( $I_{sputter} \approx 1-3\mu A$ ) for 1 h at a temperature of  $830^\circ C$  ("hot-sputtering"). This created a surface depletion layer for the intrinsic carbon contaminants of the Rhodium crystal.

h-BN on Rh(111) was prepared by chemical vapor deposition (CVD) of Borazine on a Rh(111) surface kept at  $800^\circ C$ . The hot metal surface was then exposed to 110 L of Borazine leading to the growth of a full monolayer of h-BN. The Borazine was cleaned in a so called freeze-pump method, involving repeated cycles of freezing with liquid nitrogen ( $LN_2$ ) and pumping of the volatile contaminants. The Borazine was dosed into the UHV-preparation chamber using a leak-valve. The 110 Langmuir amount to an actual exposure of the sample to a partial pressure of Borazine of  $\approx 1.2 \cdot 10^{-6}$  mbar for 3 min. Small fluctuations in the partial pressure do not affect the growth of the single layered h-BN, since the preparation parameters are chosen as such, that the h-BN grows in a self terminating process.

On a Rh(111) surface a lattice mismatch of 6.7 % [94] leads to a growth of a buckled hexagonal Moiré superstructure of the h-BN lattice with a periodicity of 3.2 nm. The buckling results from areas of close proximity ( $\approx 2.2\text{\AA}$ ) to the Rh(111) substrate (Valleys) surrounded by areas with bigger substrate-h-BN spacing ( $\approx 3.4\text{\AA}$ ) (Rims) [96]. This is depicted in Fig. 2.2 a), showing a density-functional-theory (DFT) simulation of the h-BN/Rh(111) superlattice. The DFT calculation of the h-BN/Rh(111) Moiré were performed by Z. Hooshmand and T. Rahman (University of Central Florida) in a joint collaboration. The results are in good agreement with other DFT simulations, as for example reported by Gómez Díaz et al. [96]. In literature the valley areas of the h-BN are also often referred to as "holes" or "pores" [94, 97]. From the DFT calculations it is possible to simulate a STM topography image (Fig. 2.2b), which shows that the h-BN valleys exhibit quasi-hexagonal shapes with lower apparent height. The lower apparent height of the valleys originates from the increased interaction of the h-BN with the substrate, partially depleting the electrons of the underlying rhodium, that contribute to the conduction near the Fermi-level. This corresponds well to the STM topography observed in

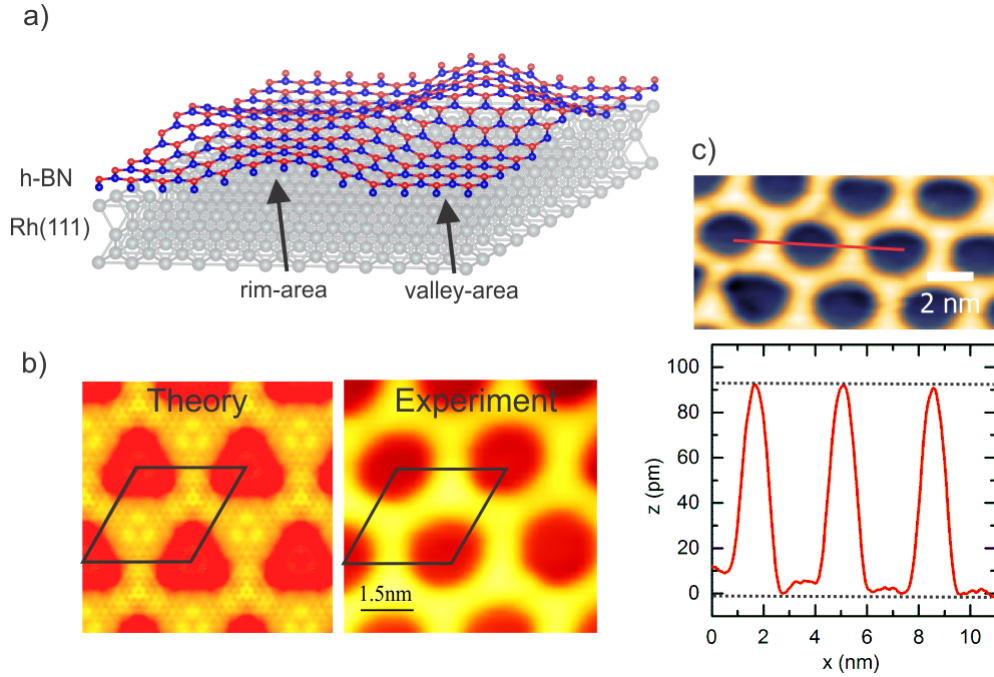


Figure 2.2 – a) DFT simulation of the buckled h-BN superstructure on Rh(111). b) Simulated STM topography image of the h-BN/Rh(111) Moiré-pattern in comparison to an experimentally determined STM topography image of h-BN/Rh(111) (Acquisition parameters:  $I = 50$  pA,  $U_B = -0.5$  V) (c). STM topography image and profile of apparent height corresponding to the red line. ( $I = 50$  pA,  $U_B = -0.5$  V)

the experiment (c.f. Fig. 2.2 b), c) ), although the shape of the valley is more rounded than in the simulation. This might be caused by the shape of the tip. Experimentally a difference in apparent height of about 90 pm between valley and rim is observed which is in good agreement with literature [94].

STS measurements on the valley and rim regions of the h-BN show, that the single h-BN sheet has insulating character with a band gap of  $\approx 7$  eV in the valley and  $\approx 5$  eV on the rim positions (Fig. 2.3). These values are in good agreement with literature values [87].

With typical measurement parameters of  $U_B \approx 0.5$  V and  $I \approx 50$  pA, the periodic structure of the Moiré pattern of h-BN on Rh(111) is observable. However the poor resolution does not allow any conclusions about the atomic structure, especially inside the valley region. In order to resolve the atomic structure, measurements with more extreme parameters ( $U_B = 0.005$  V,  $I = 90$  nA,  $G \approx 1.8 \cdot 10^{-5}$ ) were performed. These values correspond to conductance values comparable to those of  $G_0 = \frac{e^2}{h} \approx 3.87 \cdot 10^{-5} \Omega^{-1}$ , implying a point contact between tip and the h-BN surface. The results of these measurements are depicted in Fig. 2.4. One can see, that it was possible to resolve the atomic structure of the h-BN. A cartoon of the chemical structure of h-BN is superimposed with the experimental data for comparison. Additionally a



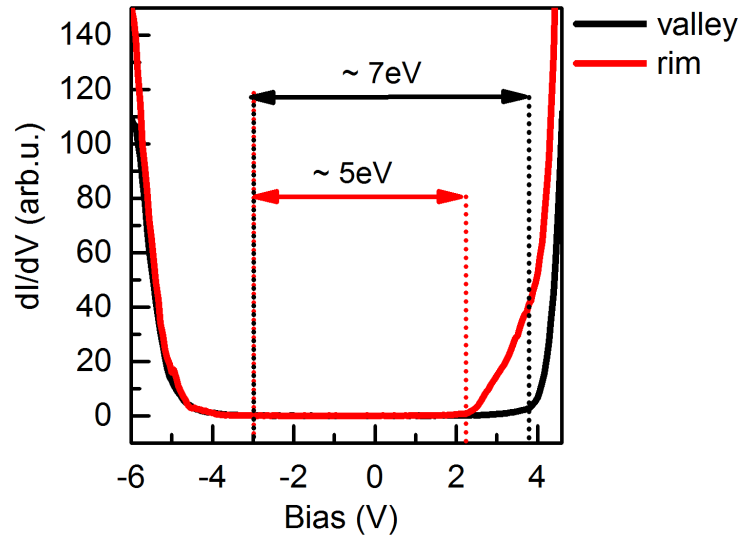


Figure 2.3 – STS measurement on h-BN valley and rim position. The observed band gap is indicated in the graph. Lock-in parameters: Modulation voltage  $U_{Mod} = 50\text{mV}$ , modulation frequency:  $f_{mod} = 832\text{Hz}$ .

difference in contrast between every other atomic position in the h-BN hexagons (e.g. between B and N sites) is observable at the highest magnification. Unfortunately an unambiguous assignment of the high and low contrast region to Boron or Nitrogen cannot be performed.

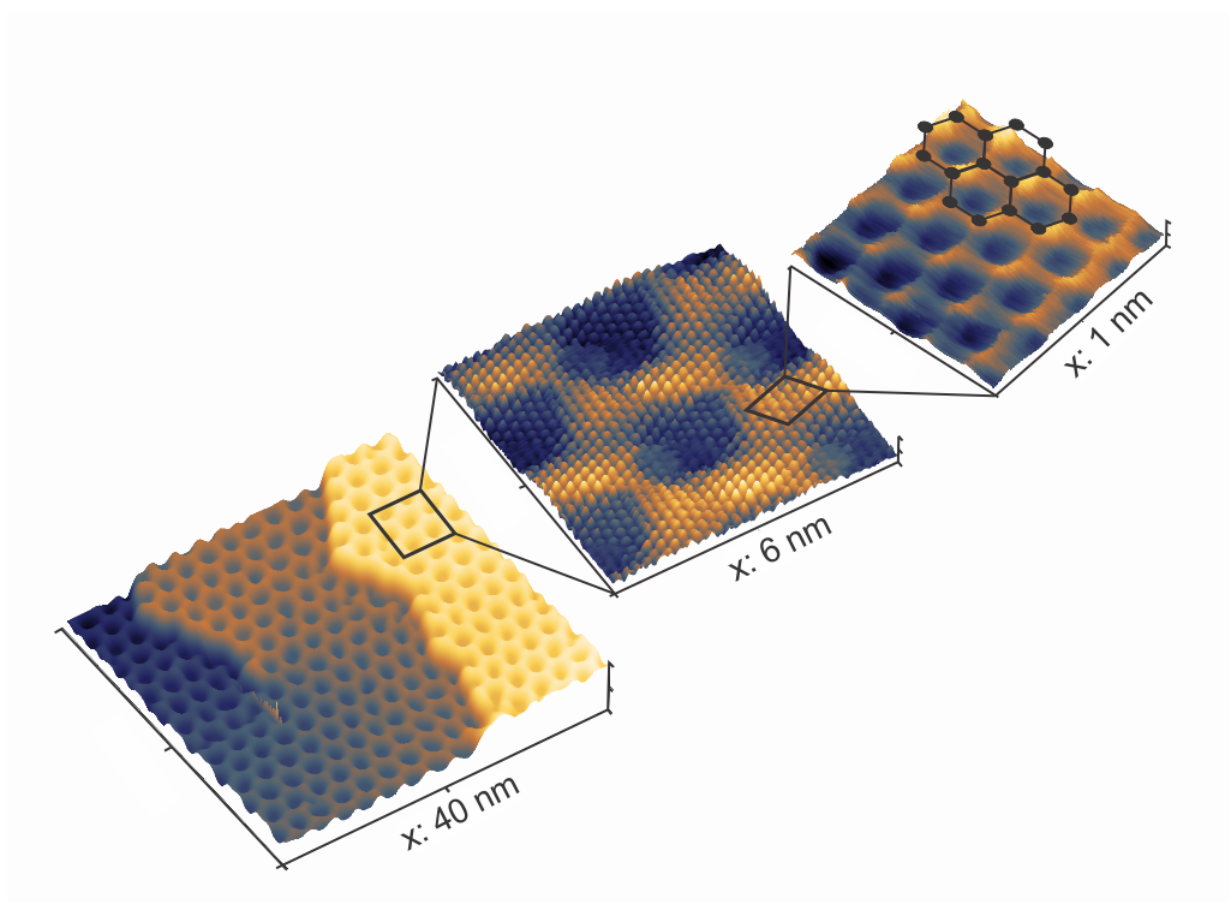


Figure 2.4 – Atomic resolution STM topographs of the h-BN/Rh(111) Moiré-pattern.

### 2.2 Pentacene on h-BN/Rh(111)

The following section is based on our recent publication (Kosłowski et al., Pentacene adsorption and electronic properties on thin dielectric decoupling layers, Submitted to: Beilstein Journal of Nanotechnology, December 2016).

As already motivated in the introduction of this chapter, a thin spacer layer with a large band gap of several eV can be used to electronically decouple molecules from a metal substrate and study them by STS. Various thin insulating layers have so far been used as decoupling layers in STM experiments [85]. However, it was stated that a weak interaction between the metal substrate and the ad molecule is still present, due to the observation of a deviation of the orbital energies from their unperturbed state. Therefore it is desirable to classify these systems according to their capability to effectively decouple an organic adsorbate from the underlying metal substrate. In this section pentacene ( $C_{22}H_{14}$ ) is used as a model system and its structural and electronic properties on a monoatomic layer of hexagonal boron nitride (h-BN) are investigated and compared to its properties on KCl layers grown on various low-index

noble-metal surfaces.

### Sample preparation of pentacene on h-BN/Rh(111)

A Rh(111) single crystal was cleaned and h-BN was prepared according to the procedure described in previous section. Pentacene molecules were deposited by thermal sublimation at 185°C. The deposition time was adjusted to achieve submonolayer coverage with individual pentacene molecules on the sample surface. During the pentacene deposition, the substrate was kept at room temperature.

### Structural and electronic properties of pentacene on h-BN/Rh(111)

A Rh(111) single crystal was cleaned and h-BN was prepared according to the procedure described in previous section. The pentacene molecules deposited onto h-BN on Rh(111) are preferentially found at the edges of the valleys of the h-BN Moiré superstructure (Fig. 2.5), similarly to what was observed for the Xe/h-BN/Rh(111) system [86] that was explained by dipole rings inside the valleys. This resulting in-plane electric field attracts the adsorbed molecules to the edges of the valleys.

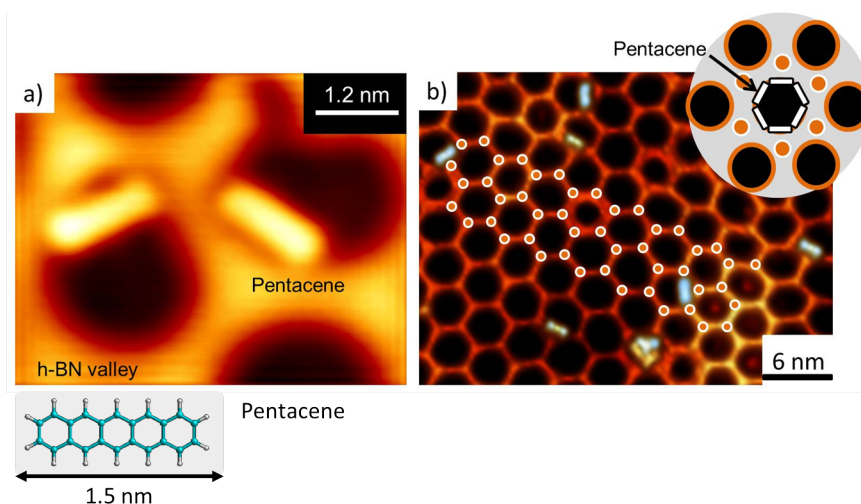


Figure 2.5 – a) STM topography image of pentacene on h-BN. b) Large-scale STM topography image of pentacene on h-BN. The white circles indicate the preferential adsorption sites illustrated in the inset. Inset: Illustration of the six possible pentacene adsorption geometries inside the h-BN valley.

The pentacene molecules appear as 1.5 nm long rod-like objects with an apparent height of about 1 Å when scanned in a bias range of  $\pm 1$  V below the lowest molecular state (Fig. 2.5 a)). An overall preferential 6-fold adsorption geometry can be observed. The pentacene molecules preferentially adsorb with their long axis facing an intersection of rims (orange dots in inset Fig.

2.5 b)). Molecules perpendicular to the h-BN rim are not observed. Geometric conditions, e.g. energy minimization due to best alignment with the hexagonal valley, might hinder additional adsorption geometries. Defects or multiple pentacene molecules adsorbed in the same valley, however, break this scheme and cause adsorptions in alternative geometries.

The electronic properties of the pentacene molecules were probed by measuring the differential conductance ( $dI/dV$ ) in STS experiments. In STS, pentacene reveals two molecular orbitals near the substrate Fermi energy, one at negative (-2.1 V) and one at positive bias voltages (+1.2 V) (Fig. 2.6). The absolute peak positions showed some variation from molecule to molecule, presumably due to slightly different adsorption geometries. The typical gap between the peaks amounts to  $3.39 \pm 0.31$  V. The positions of the peaks were determined to be  $-2.16 \pm 0.16$  V and  $+1.22 \pm 0.22$  V. The error was obtained as standard deviation from statistical evaluations of the measured molecules. Repp et al. [35] stated for experiments on pentacene on NaCl/Cu(111) that tunneling through these states of pentacene results in a temporary charging of the molecule prior to the dissipation of the charge into the substrate. The peaks observed in STS on pentacene are therefore also referred to as the positive- and negative-ion resonances (PIR and NIR). Thereby, the NIR corresponds to the HOMO and the PIR to the LUMO.

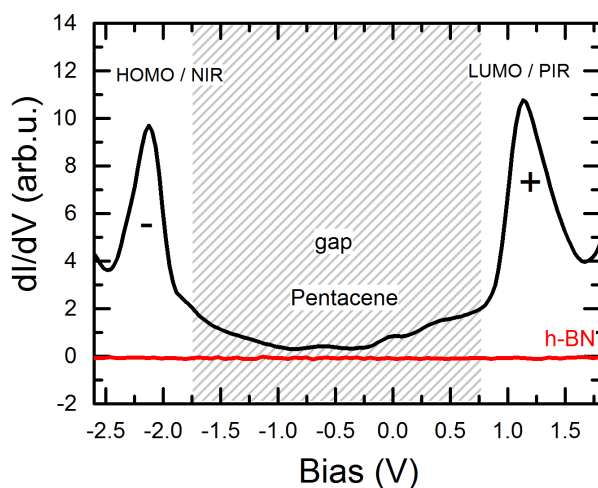


Figure 2.6 – STS of pentacene on h-BN/Rh(111) showing the resonances of the frontier molecular orbitals. The red curve depicts the  $dI/dV$  of bare h-BN. Zero bias refers to the Fermi energy of the Rh substrate.

Spatial imaging at the energies of the orbitals observed in STS yields the shape of the DOS of the frontier orbitals of pentacene [98][35][99]. For +1.2 V, two prominent lobes connected by a series of dimmer lobes are observed (Fig. 2.7a)). This structure can be ascribed to the LUMO.

For voltages within the HOMO-LUMO gap between -1.75 V to +0.75 V, the molecule appears as a featureless rod with low apparent height (Fig. 2.7 b)). At -2.16 V, we observe the structure of the HOMO (Fig. 2.7 c)), with 4 prominent lobes connected by a row of smaller lobes. The differences in apparent height along the short axis of the molecule can be attributed to the local slope of the adsorption position at the edges of the valley of the h-BN mesh underneath the molecule.

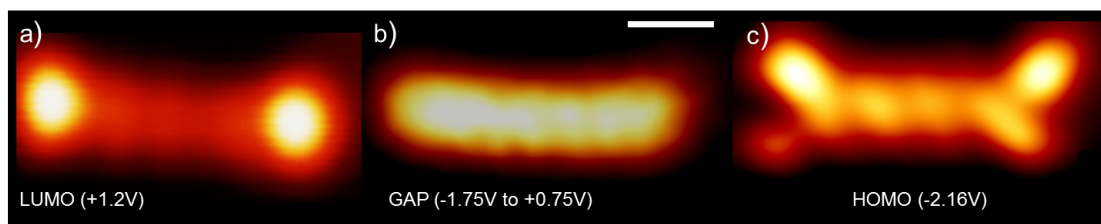


Figure 2.7 – Spatial mapping of the molecular orbitals of pentacene. a) at positive (LUMO), b) inside the gap and b) at negative (HOMO) bias voltages (bias voltages are indicated in the image). The scale bar equals 0.5 nm.

In order to improve the spatial resolution, the tip is functionalized with a pentacene molecule, as it has been shown for pentacene on NaCl [35]. Accordingly the functionalization is achieved by positioning a metallic tip over the endpoint of the pentacene molecule. While monitoring the current, the tip is lowered until an abrupt change in the tunnel current is measured, marking the jump of the molecule to the tip apex. A successful tip functionalization can be observed by the vanishing of the pentacene molecule from the surface (c.f. Fig. 2.8a)) and the appearance of additional resonances in STS mainly at negative  $U_B$  (c.f. Fig. 2.8b)). These changes might be attributed to the molecular resonance of the pentacene adsorbed on the tip. Using a functionalized tip, the LUMO is now imaged as a structure with two bright lobes at the ends separated by 5 smaller elongated lobes with slightly varying shapes. The HOMO exhibits 4 prominent lobes at the edges and 6 minor lobes. The structure has a node along its long axis (Fig. 2.9). This observation is in good agreement with the results published in [100] stating, that a p-wave tip increases the sensitivity towards orbital structures with high spatial gradients in their orbital structure [35]. Furthermore, a pentacene-functionalized STM tip might express a considerably smaller effective tip apex due to scanning with one of the  $\pi$ -orbitals of the attached pentacene molecule and thereby improves spatial resolution.

The assignment of HOMO and LUMO is further supported by Hückel calculations which yield nodal structures similar to the ones observed by STS.

The calculated orbital structure consists of a sequence of orbital lobes with alternating sign of the wave function  $\phi$ , indicated by the color code (violet, green) in Fig. 2.10. The experimental

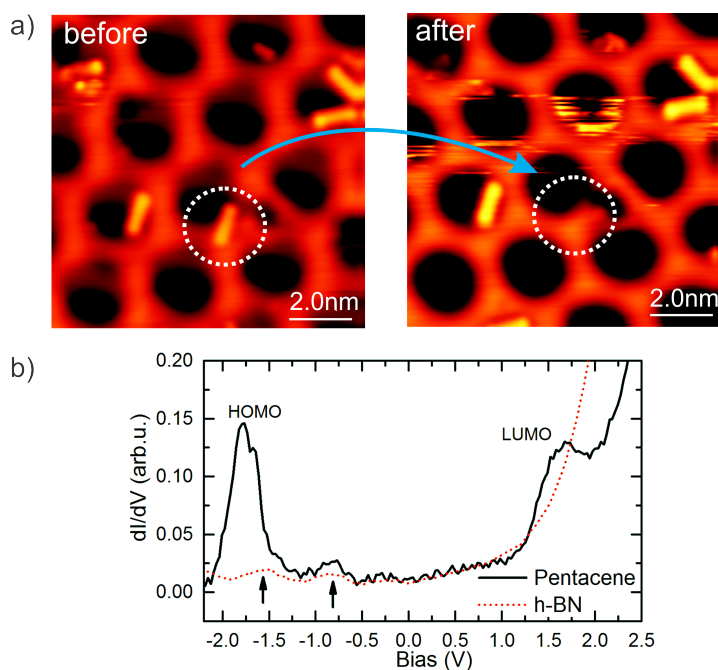


Figure 2.8 – a) STM topography image before and after picking up of a pentacene molecule by the tip (dotted circle). (Acquisition parameters:  $U_B = -1$  V,  $I = 50$  pA) b) STS measurement on h-BN (red dotted line) and pentacene (black line) with a pentacene molecule at the tip (Acquisition parameters:  $I = 50$  pA,  $U_{mod} = 50$  mV,  $f_{mod} = 832$  Hz)

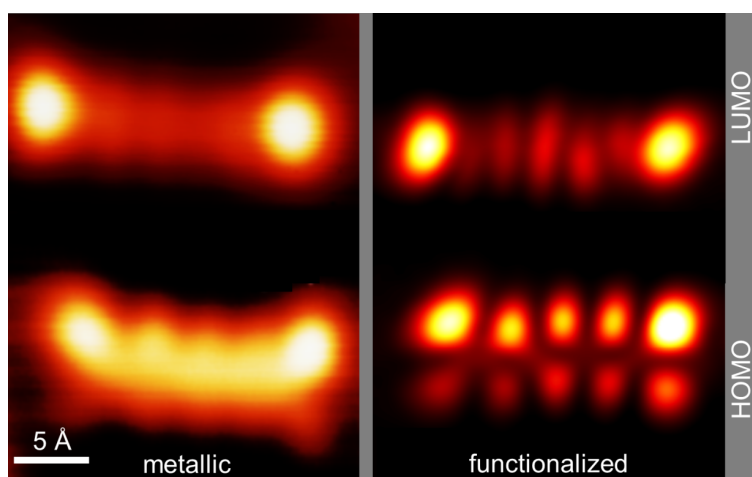


Figure 2.9 – Spatial mapping of the molecular orbitals of pentacene by employing an STM tip without (left) and with (right) pentacene functionalization.

observation is in good agreement with the structures obtained from Hückel calculations of the free molecule.

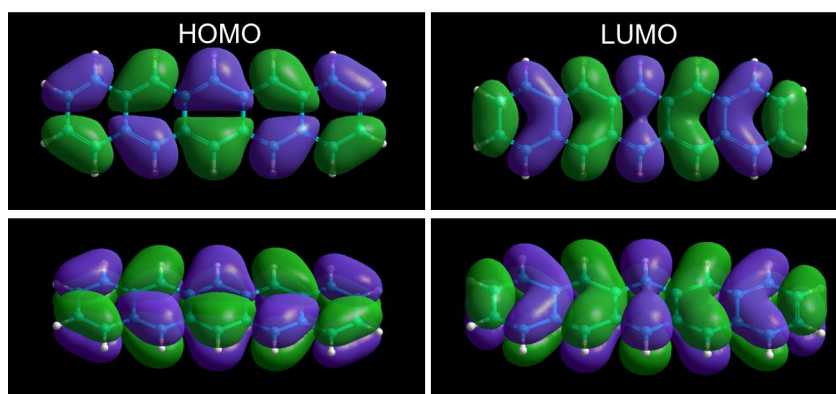


Figure 2.10 – Hückel calculations of the DOS of the frontier molecular orbitals (HOMO and LUMO) of pentacene in the gas phase superimposed with a ball and stick model of the molecular structure (Calculated using HyperChem).

### Level alignment of organic - insulator interfaces

In order to quantify the values observed for the HOMO and LUMO in terms of their energy position, one has to relate them with other measurable quantities of the investigated system. Two well-suited quantities for molecules are the electron affinity ( $E_a$ ), i.e. the energy cost of adding an electron to the neutral molecule, and the ionization energy ( $E_i$ ), the energy needed to remove an electron from a neutral molecule [101]. For various molecular species, including pentacene, these values are well known from photoemission and inverse photoemission experiments [102].

In a first approximation, the physical quantity connecting  $E_a$  and  $E_i$  with the measured energetic positions of the HOMO and LUMO, respectively, is the work function  $\phi$  of the underlying h-BN/Rh(111) substrate, namely the energy difference between the vacuum level and the Fermi energy. The specific relation between these quantities is depicted in the scheme in Fig. 2.11.

$\phi$  of a surface is defined as the energy, which is required to remove an electron from  $E_F$  into the vacuum at infinite distance.  $\phi$  influences the reactivity, the adsorption geometry of adsorbates or catalysis reactions [103].  $\phi$  of a material is a surface property and can furthermore vary depending on the termination of the surface. This was demonstrated on the example of Ag. Ag(111) has a  $\phi$  of 4.74 eV, Ag(110) 4.52 eV and Ag(100) 4.64 eV [104]. This can be explained by the different surface properties of each termination regarding surface dipoles or the distribution of charge density.  $\phi$  can moreover also vary laterally due to adsorbates such as clusters of metal atoms or molecules [105] [106]. Also thin dielectric adlayers such as salt-layers [107], graphene [108] or h-BN [96] modify  $\phi$  laterally via spatial variations of the adsorption geometry (in general caused by lattice mismatches between the supporting



substrate and the adlayer). These influence locally properties as the charge transfer between the metal substrate and the dielectric.

$\phi$  of a surface can be determined by photoemission [109] or transport-based techniques [103] on large scales. For atomic scales the Kelvin probe technique [110] or the measurement of field-emission states (FER) [107] can be used to locally probe  $\phi$  utilizing an atomic force microscope (AFM) or STM.

The underlying h-BN substrate can be described with  $\phi = 4.15$  eV [97]<sup>1</sup> as a literature value for  $\phi$  for a single layer of h-BN on Rh(111). With this, the HOMO at -2.16 V can be attributed to a bound state with an energy of 6.31 eV, respectively the LUMO at 1.2 V to a bound state with an energy of 2.95 eV. These energies can be related to the electron affinity of 1.35 eV [101] and the ionization energy of gas-phase pentacene at 6.58 eV [102]. The deviation of the gas-phase energies from the energies found on the surface can be explained by the screening of the underlying substrate during the temporary charging of the molecule [111][112]. In the presented measurements a decrease of the HOMO/LUMO gap by 1.87 eV (e.g. an average shift of 0.85 eV for HOMO and LUMO) in comparison to the gas-phase value for pentacene was observed. Thus the molecular ion (positive/negative) is stabilized with respect to the gas-phase ion due to screening of the molecular ions' charge, induced by the formation of image charges in the topmost layers of the metal substrate, as described by Willenbockel et al. [113]. This is in agreement with photoelectron spectroscopy measurements on pentacene molecules in the gas phase. Measurements on molecules adsorbed on metal surfaces showed that the energies of both the HOMO and the LUMO were shifted towards the Fermi energy, reducing the HOMO/LUMO gap of the molecule.

To estimate the expected reduction of the gap, a point-charge model is utilized assuming a flat h-BN layer on a planar metal substrate. A single charge ( $q_1 = q_2 = e$ ) at a distance  $2d$  from its image charge is assumed. The distance  $d$  between the charge (ion) and the metal surface (reflection plane) was estimated to be 2.8 Å using calculations for the h-BN/Rh(111) system based on the local distance of the h-BN layer at the position of the pentacene molecule from the metal substrate [96]. A value of  $\epsilon_R = 4$  is assumed for the dielectric constant of h-BN, as proposed by Kim et al. [114] for 2-5 nm thin h-BN films. Using the following formula, the resulting energy shift can be estimated:

$$E_{el} = -\frac{q_1 q_2}{4\pi\epsilon_0 2d\epsilon_R} \quad (2.1)$$

---

<sup>1</sup>This value is a theory value based on DFT, because no reliable experimental data was available for single layer h-BN/Rh(111).



Pentacene on:	$E_a$ (eV)	$E_i$ (eV)	$E_{gap}/E_{gap,0}$	$\phi$ (eV)
KCl/Au(111)	1.7	6.15	0.85	3.8
KCl/Cu(111)	0.95	5.14	0.8	2.7
h-BN/Rh(111)	2.75	6.3	0.68	4.15[97]
KCl/Cu(110)	1.67	4.09	0.46	2.2

Table 2.1 – Experimental values for  $E_a$ ,  $E_i$ ,  $E_{gap}/E_{gap,0}$  for pentacene as well as the values for  $\Phi$ .  $\Phi$  has been determined experimentally for the KCl layers on the various substrates by I(z) measurements. For h-BN, a literature value is presented.

Approximating the ion as a point charge at the center of a pentacene molecule yields an estimate for the energy shift of about 0.64 eV, compared to the measured shift of 0.85 eV.

One can see that this model gives a good estimate for the energy shift and thus for the screening energy stabilizing the molecular ion on the surface. It should be noted that this can only to be seen as a rough approximation for the energy, because of the uncertainties of the molecular distance  $d$  from the effective metal surface and the dielectric constant of a single sheet of h-BN. To compare and rationalize the results obtained for pentacene on h-BN/Rh(111), measurements on a different metal/insulator system need to be performed. In literature alkali halides such as KCl and NaCl [81][115] have been described to be suitable decoupling layers growing in atomically flat epitaxial films on metal substrates. Therefore STS measurements of pentacene were carried out on KCl/Au(111), KCl/Cu(111) and KCl/(Cu110). The resulting STS data are depicted in Fig. 2.12. The respective metal substrates were cleaned in an analogous way as the Au(111). The KCl layers on various metal surfaces were generated by thermal evaporation of KCl at 380°C for 20 min. During this process, the substrates were kept at room temperature. The HOMO/LUMO gap can be used as a measure of the efficiency of an insulating layer to electronically decouple an adsorbate from the metal substrate. The ratios between the on-surface  $E_i-E_a$  gaps and the unperturbed gas-phase gaps are listed in Table 2.1. For a similar decoupling layer (KCl), but various substrates, the decoupling strength decreases with the work function of the substrate. Willenbockel et al. stated that higher workfunctions tend to lead to a larger molecule-substrate spacing upon adsorption [113]. Furthermore the remaining interaction of the pentacene with the respective metal plays an additional role in the decoupling, since the inert Au(111) substrate perturbs the molecular states less than the more reactive Cu(110) substrate.

The values for  $E_a$  and  $E_i$  were calculated for all the investigated material systems according to the scheme shown in Fig. 2.11 (Table 2.1). Plotting  $E_a$  and  $E_i$  versus the work function of the respective substrate yields the graph depicted in Fig. 2.13.

As suggested by Willenbockel et al. [113], HOMO and LUMO do not necessarily interact equally

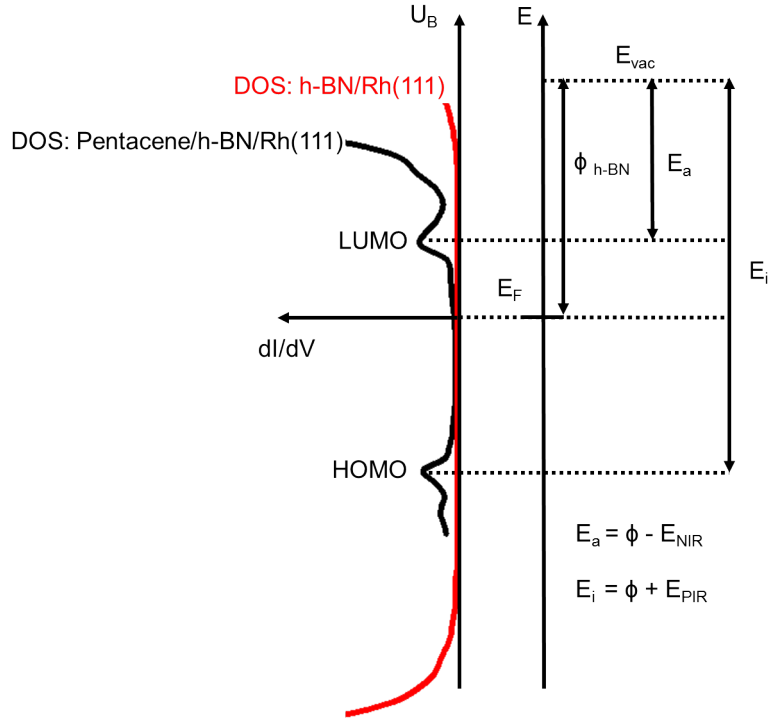


Figure 2.11 – Energy level diagram depicting the relations between  $E_a$ ,  $E_i$ ,  $\phi$  and the energies measured in STS for the HOMO and LUMO of pentacene.

with the substrate. The suggested parameter  $S = \frac{dE_B}{d\Phi}$ , the derivative of the binding energy with respect to the work function is an indicator for the binding strength. Molecular orbitals which interact weakly with the metal will maintain a fixed binding energy with respect to the vacuum level, and thus a value of  $S$  close to zero. Orbitals which are strongly bound to the metal will be energetically fixed with respect to the Fermi level, and since the Fermi level decreases linearly with the work function, this results in a value of  $S$  close to -1. A value of  $S < -1$  suggests a stabilization mechanism beyond the model, such as bond stabilization due to the shift of binding orbitals towards higher energies [113]. The values of  $S_{HOMO} = \frac{dE_i}{d\Phi}$  and  $S_{LUMO} = \frac{dE_a}{d\Phi}$  were obtained by fitting the data points for  $E_a$  and  $E_i$  of the pentacene/KCl/metal substrates to a linear function. The energy levels of pentacene/h-BN/Rh(111) were not included in the fit due to the different nature of molecule-substrate adsorption in this case, which is discussed below. For  $S_{HOMO} = -0.12 \pm 0.5$ , a value close to 0 reveals the vacuum level pinning of  $E_a$ , which implies a weak coupling of this orbital to the substrate. On the other hand,  $E_i$  decreases with increasing work function, with a slope  $S_{HOMO} = -1.22 \pm 0.28$ . In this case, the value of  $S_{HOMO}$  is close to -1 (within less than a standard deviation of -1), which suggests that the HOMO is Fermi-level pinned and therefore more strongly coupled to the substrate. In

summary, this implies that the LUMO is vacuum-level pinned and the HOMO is Fermi-level pinned.

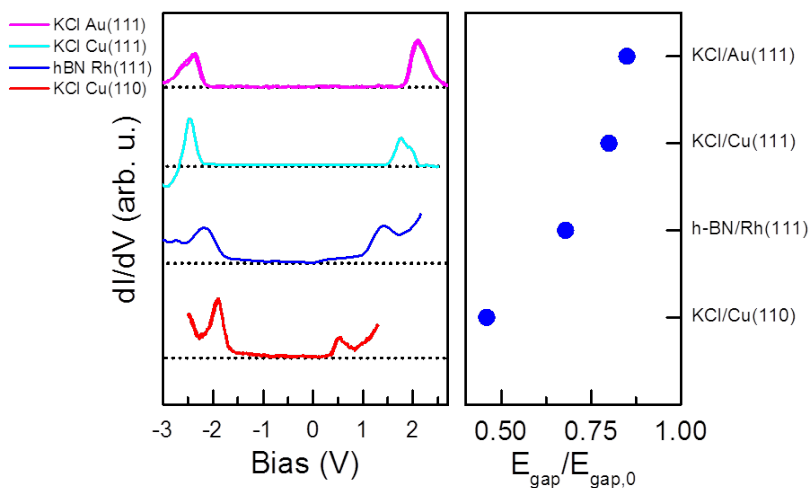


Figure 2.12 – STS measurements of pentacene on various decoupling layers (see legend). In the case of Au(111) and Cu(111), KCl grows as a bilayer, whereas on Cu(110), a monolayer growth was observed. The right graph indicates the deviation of the HOMO-LUMO gap of pentacene on the respective surfaces ( $E_{\text{gap}}$ ) from its unperturbed gas-phase gap ( $E_{\text{gap},0}$ ).

The results suggest that the approach of Willenbockel et al. for determining the mechanism of orbital pinning for HOMO and LUMO [113] is not limited to molecules adsorbed onto bare metals, but is also valid for single molecules on metals covered with a thin decoupling layer having homogeneous properties. An exception is found for the HOMO on h-BN where the intrinsic dipole moment of the molecule within the depressions in the h-BN superstructure modifies the coupling strength between molecule and substrate. The observations show, how the energies of the molecular orbitals of pentacene adsorbed on h-BN/Rh(111) deviate from the trend set by pentacene on KCl/metal (Figure 2.13). This deviation reflects the unique characteristics of the adsorption of molecules on h-BN/Rh(111), namely the corrugated surface and attraction by local electric fields parallel to the surface. Lateral electric fields have a stabilizing effect on the molecular orbitals, which, for a symmetric orbital, depend on its polarizability [116]. In addition, the molecules appear curved as a result of both, the h-BN curvature and the curved geometry of the attractive electric field. These unique properties of h-BN/Rh(111) can explain why the HOMO of pentacene deviates from the trend set by pentacene on KCl/metal.

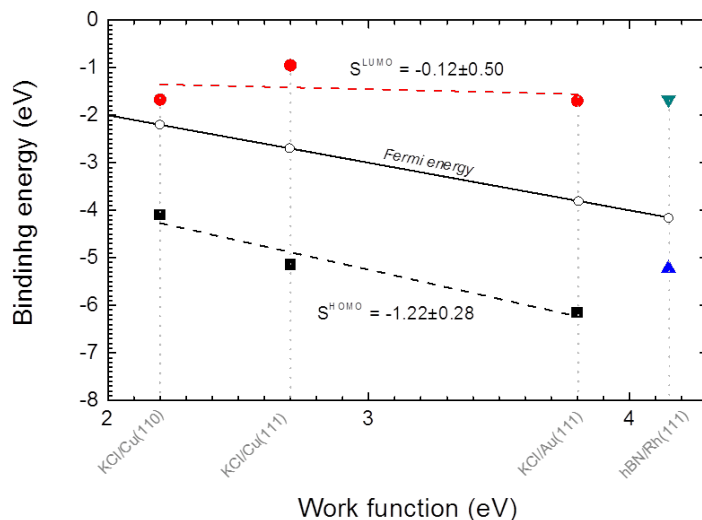


Figure 2.13 – Experimentally determined energies for  $E_a$  (red circles) and  $E_i$  (black squares) of pentacene versus the workfunction of the respective KCl/metal substrates. Separately indicated are the values for h-BN/Rh(111). Dashed lines indicate linear fits of  $E_a$  and  $E_i$ . The open circles indicate the position of the Fermi-energy (black line).

## 2.3 Conclusion part I

As a conclusion, the effective decoupling properties of h-BN could be confirmed for the system of pentacene on h-BN/Rh(111). The h-BN layer offers a desirable capacity to immobilize molecules inside the valleys on the surface, even at room temperature. The trapping capacity most likely originates from an interaction with in-plane electric fields present on the substrate. This enhances the molecule-substrate interaction, which decreases the HOMO-LUMO gap in comparison to the same molecule adsorbed on KCl/metal surfaces. In spite of this interaction, h-BN/Rh(111) provides sufficient electronic decoupling to allow the clear observation of pentacene HOMO and LUMO peaks by STS. Furthermore, STS mapping at the peak energies reveals the shapes of the corresponding molecular orbitals, and tip functionalization further improves the contrast of these structures. In order to further rationalize the results obtained by STS on pentacene on the h-BN/Rh(111) substrate, comparative studies using a different decoupling layer, namely KCl on varying metal substrates, were performed. For pentacene on KCl/metals, it is surprising that in spite of the complexities of molecule-metal adsorption, the work function of the surface plays a decisive role in determining the energies of the binding molecular orbitals. The observed trends indicate that HOMO and LUMO participate to different extents in binding to the surface. The binding energy of the HOMO is unchanged

with respect to the Fermi energy on all three KCl surfaces, indicating an enhanced degree of interaction with the metallic substrate. The LUMO, on the other hand, keeps a fixed position with respect to the vacuum level, suggesting a weaker interaction with the metal. The results reported here illustrate the benefits of comparing spectroscopic data from the same molecule on similar substrates. Thus, a trend can be observed in the relation between orbital energies and work function, which reveals the physical properties of the molecule and the substrates which are relevant to adsorption. In addition, a deviation from this trend for hBN/Rh(111) helps rationalize its enhanced trapping capacity and its uncommon interaction mechanism. This study might be of special interest for the field of molecular electronics, where a precise knowledge of the energetic positions of the available states is of great importance.

## 2.4 Intercalated carbon h-BN/Rh(111)

When growing h-BN on Rh(111) according to the experimental procedure described in the previous sections, the Rh crystal is submitted to a "hot-sputtering". This preparation step allows to grow clean h-BN on the crystal surface due to the generation of a sub-surface depletion layer for the intrinsic contaminants of the Rh-crystal. The amount of the subsurface impurities can be controlled by cycles of subsequent  $Ar^+$ -bombardment and annealing, which are thinning the sub-surface depletion layer. Depending on the thickness of the depletion layer, it is possible to observe three structures which are depicted in Fig. 2.14. For a small concentrations of impurities, isolated triangular defects located at every other rim site of the h-BN Moiré pattern as shown in Fig. 2.14a) can be observed. These defects appear as regular triangles with a size of about 2 nm and three corners with increased apparent height. Each of these corners corresponds to the area of about three atomic hexagons of the h-BN layer. The triangles are surrounded by sharp lines of low contrast.

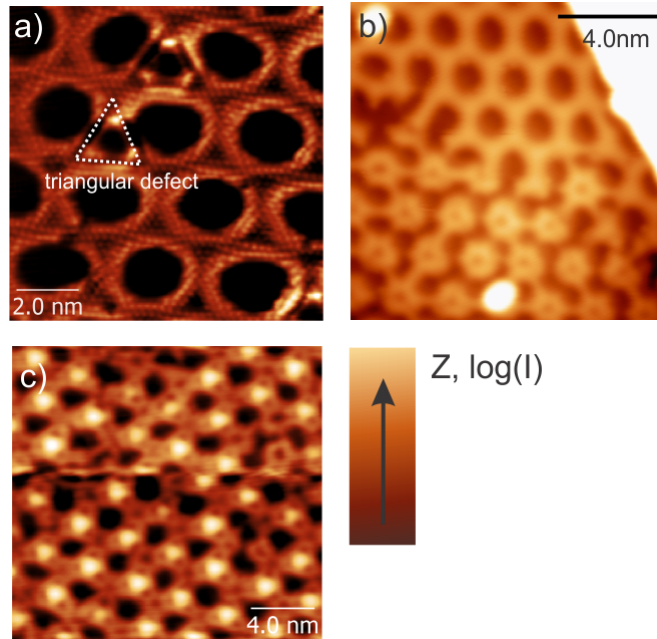


Figure 2.14 – a) High resolution STM image in constant height mode of individual triangular defects in h-BN layer.  $U_B = 5$  mV,  $I = 5$  pA b) Overview STM topography image of h-BN next to IC-h-BN. ( $U_B = -1$  V, Setpoint:  $I = 50$  pA) c) STM image of graphene/Rh(111). ( $U_B = -2$  V,  $I = 10$  pA)

Interestingly for higher contamination concentrations (e.g. a thinner depletion layer) present at the crystal surface, we observed large continuous domains of a new phase with an altered Moiré pattern so far not reported in literature to our knowledge (Fig. 2.14 b)). For simplicity this new phase will be referred to as "intercalated carbon h-BN" (IC-h-BN). The choice of this

name will become apparent in the course of this chapter.

This phase consists of an ordered arrangement of star-shaped structures. In several cases the appearance of a third pattern depicted in Fig. 2.14 c) can be detected alongside the IC-h-BN. This structure can be related to the Moiré-pattern of graphene on Rh(111) [117][118] and appears for very high carbon concentrations within the topmost atomic layers of the substrate. The reproducible observation of the three additional structures shown in Fig. 2.14 along the h-BN depend on the thickness of the Rh surface depletion layer. This hints at the fact, that carbon diffusing to the Rh(111) surface during the h-BN preparation are the origin of the IC-h-BN. Adsorbents on the Rh(111) surface prior to the h-BN preparation are unlikely to be involved in the formation of the IC-h-BN. The catalytic decomposition of borazine and its interconnection to h-BN involves the generation of radical hydrogen as intermediate step. Along with the elevated temperatures of  $\approx 800^\circ\text{C}$  this would cause typical contaminants such as carbon compounds to react to small volatile molecules and leave the surface. Furthermore the catalytically active Rh(111) surface is necessary for the formation of h-BN. A closed layer of contaminants would inhibit this process as it can be seen for the example of the formation of graphene (Phase diagram of C-Rh: segregation of C and Rh into graphite and fcc-phase for high C concentrations [119]). The abundance of graphene additionally hints at carbon being one of the dominant contaminants in the present case. Furthermore it has been shown that carbon has a temperature dependent solubility (Phase diagram of C-Rh: lowest solubility in bulk-Rh at  $\approx 730^\circ\text{C}$  for low C concentrations [118, 119] and thus is likely to segregate to the crystal surface. In the following the focus is laid on a detailed discussion of IC-h-BN. Complementary techniques and theoretical descriptions of the structure were utilized to gain deeper understanding of the initial effect observed by STM topography imaging.

### High resolution STM imaging of IC-h-BN

Investigations of IC-h-BN by high resolution STM imaging gave insight into the periodicity and the structure of the Moiré-pattern. A high resolution image is depicted in Fig. 2.15. The respective parts of the Moiré-pattern are denominated in the inset. The high resolution scans reveal, that the continuous layer of IC-h-BN seems to consist of a long range ordered arrangement constructed from the individual triangular defects depicted in Fig. 2.14. If the triangles form at every other rim site of the h-BN Moiré-pattern the remaining Moiré-pattern is altered in contrast to the normal h-BN. Additional structures in the IC-h-BN are areas of low apparent height and hexagonal shape ("hexagon") as well as elevated triangular regions ("bright triangles"). The line profile depicted in Fig. 2.15 shows, that the hexagons have a periodicity of about 3 nm.

Performing scans on areas where both phases are present (Fig. 2.16a)) it can be seen that there

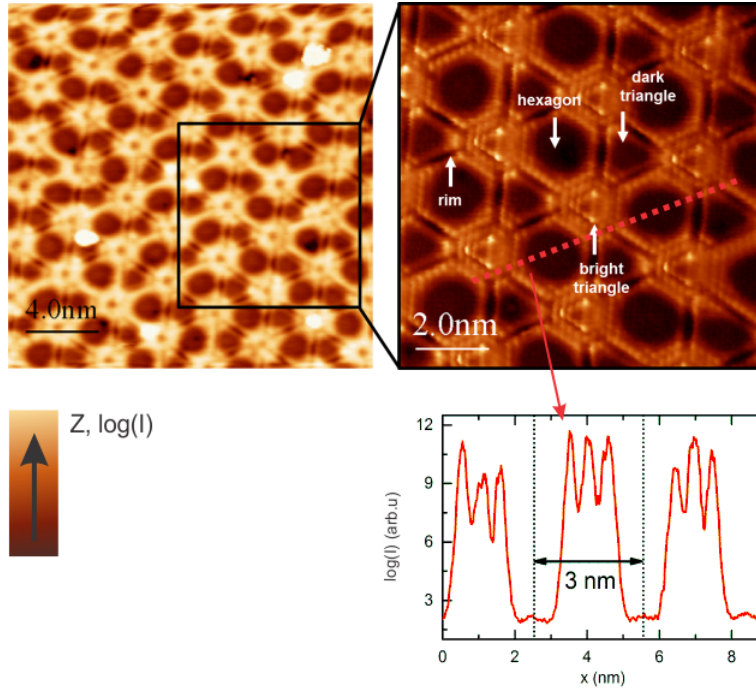


Figure 2.15 – Overview STM topography image of IC-h-BN.  $U_B = -1$  V,  $I = 50$  pA. Inset: high resolution STM image of the Moiré-pattern of IC-h-BN. The respective areas of the Moiré-pattern are denominated on the right STM topograph.  $U_B = 5$  mV,  $I = 5$  pA (Constant height). The red line indicates the position of the depicted profile.

is no interruption of the h-BN film but an epitaxial transition from pure h-BN to IC-h-BN. As we will discuss later in detail we can state that the areas indexed as "hexagon" correspond to the former h-BN valleys. This is for example supported by similar periodicity of the hexagons and the valleys (Fig. 2.16b)). Additionally it can be seen that the area of the hexagons reduced by about 20%.

Even in high resolution STM images the dark triangles are surrounded by structures with low apparent height in STM topography denominated as "rim". Performing scans in point contact mode, yields STM images where the atomic bonds of the IC-h-BN are visible (Fig. 2.17). These scans show, that the h-BN surface consists of one continuous atomic layer and does not contain structural defects such as rifts or broken bonds. This implies, that the modification of the h-BN Moiré takes place by modifying the space between the h-BN and the Rh(111) substrate.

An incorporation of additional elemental species into the h-BN lattice itself is also rather unlikely because of the partly ionic bonding character of the h-BN lattice [120]. However, it was shown that the intercalation of hydrogen in the space between the metal substrate and the h-BN layer is possible and results in a modification of the Moiré pattern observed in STM



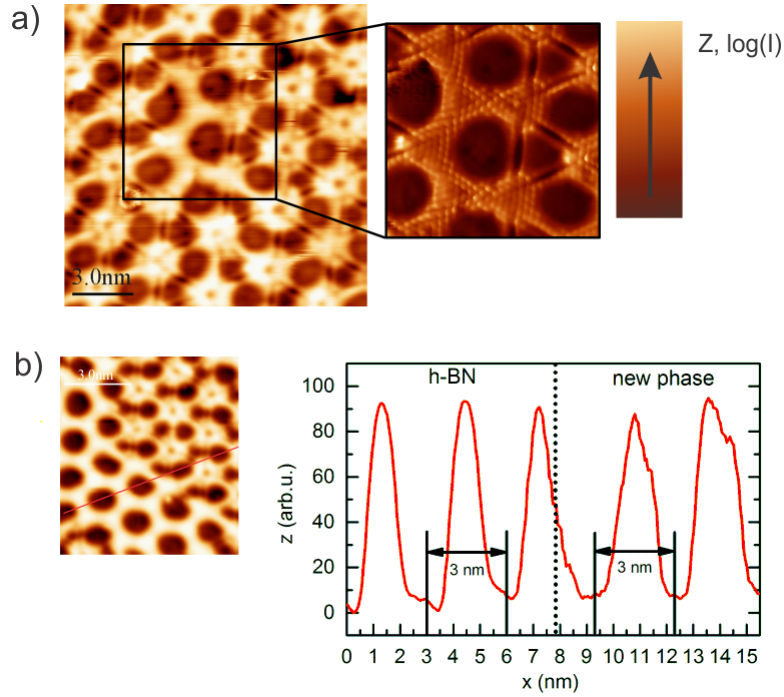


Figure 2.16 – a) High resolution STM topography image of h-BN patch surrounded by IC-h-BN ( $U_B = 5$  mV, Setpoint:  $I = 5$  pA (Constant height)). b) Line profile of  $\log(I)$  comparing the periodicities of IC-h-BN and h-BN.

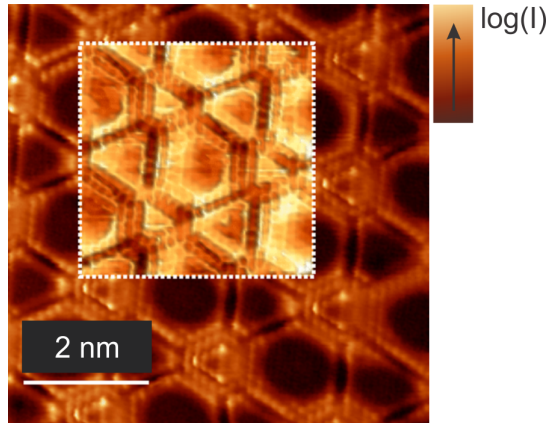


Figure 2.17 – Overview STM topography of IC-h-BN superimposed with STM image of IC-h-BN acquired in point contact mode (inset indicated by dotted line)  $U_B = 10$  mV,  $I = 90$  nA

[121]. DFT simulations of the h-BN layer predict an area of maximal distance of about  $3\text{\AA}$  between the h-BN monolayer and the metallic substrate at every other rim site, e.g. at the positions of the dark triangles. It has been shown in [122], that Ar-sputtering of h-BN/Rh(111) can lead to a trapping of Ar- atoms under exactly these h-BN rim sites. These then appear as elevated "tent-like" regions in STM images. The h-BN valleys have the shortest distance

to the metal substrate of about  $2\text{\AA}$ , and thus also have the highest interaction strength. DFT calculation suggest that the valley areas of the h-BN superlayer contribute strongly to the total adsorption energy of h-BN on Rh substrate [96]. A reduction of this area (as observed for the hexagons) would be unfavorable, if not mediated by additional atoms accumulating under the h-BN causing it to lift partially off the metal surface. A similar effect as reported for the trapping of Ar might be possible for carbon atoms diffusing from subsurface layers to the surface during the annealing. The structure of the possibly accumulating carbon is suggested in a toy model as depicted in Fig. 2.18.

The amount of carbon impurities in the subsurface layers can be used as an experimental tool to tune between samples with pure h-BN and samples with the IC-h-BN. A large depletion layer, e.g. a sample submitted to a "hot sputtering" cleaning procedure directly before the CVD growth of h-BN, will result in clean h-BN due to a lack of subsurface contaminants. Thinning this depletion layer by subsequent sputtering and annealing cycles will enhance the growth of IC-h-BN.

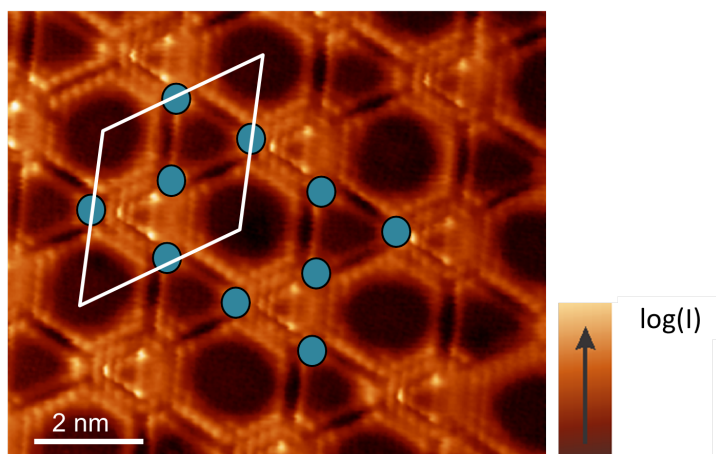


Figure 2.18 – Schematic visualization of the location of carbon (blue circles) underneath the h-BN layer. The unit cell of the Moiré-pattern indicated in white.

### Variation of $\phi$ of IC-h-BN probed by field-emission resonances (FER)

In order to gain further understanding of the electronic properties of the surface the FER of the IC-h-BN were measured and by this the spatial variation of the workfunction ( $\phi$ ) probed. For many metal surfaces, the projection of the bulk band structure to the surface leads to a projected band gap, which generates a potential barrier hindering the entrance of electrons into the bulk [123]. A negative charge, e.g. an electron, near a metal surface, will induce a positive image charge inside the metal, causing an attractive force pulling the electron towards the surface. The potential barrier of the projected band gap in combination with the attractive

force of the electron creates a well-like potential for electrons near the surface. This potential well can host a series of hydrogen-atom-like electronic states, located a few Å outside the metal surface (Fig. 2.19a) [124]. These are called image potential states (IPS) and since they are unoccupied states, they can be probed with inverse photoemission or 2-photon photoelectron spectroscopy [125][126].

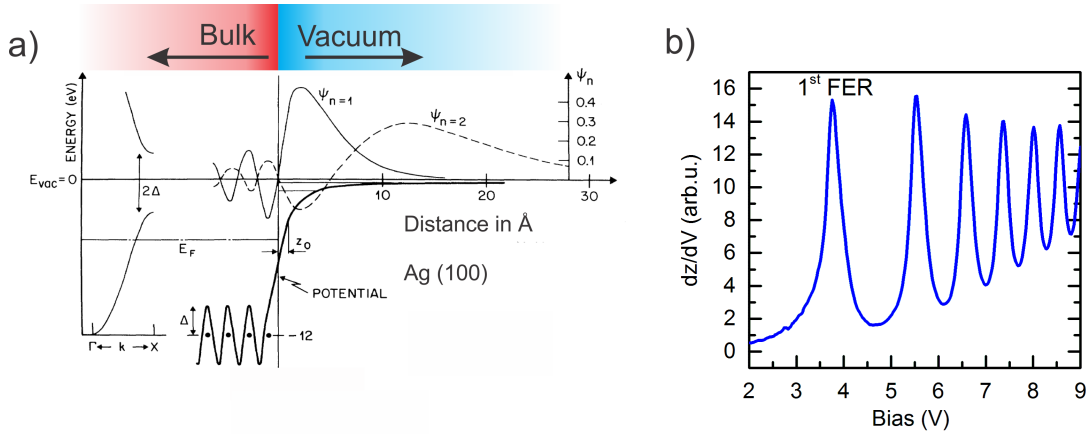


Figure 2.19 – a) Projected band gap (left) and potential structure confining the IPS on a Ag(100) surface (bold solid line). The thin and dashed lines indicate the wavefunction amplitude for the first two IPS. Modified from [127]. b)  $dz/dV$  spectrum of FER acquired with an STM on Cu(111). ( $I = 50$  pA (Constant current)).

Measuring the IPS of a surface is also possible within a STM experiment by acquiring a spectrum of the variation of the tip-sample distance as a function of  $U_B$  ( $dz/dV$  spectrum). This is done by recording variations of the  $z$  value using a lock-in technique while ramping  $U_B$ . The feedback loop is activated during this measurement and keeps the current constant. As soon as the energy level of an IPS is reached the tip retracts about 2-3 Å, leading to a peak in the  $dz/dV$  spectrum. Such a spectrum is depicted in Fig. 2.19 b) for Cu(111). When probed with STM, the strong electric field within the tunnel junction causes a Stark shift of the IPS [128]. Thus these states are referred to as field emission resonances (FER) in the context of STM experiments as described by Binnig et al. [129]. FER energies are determined with respect to the position of the vacuum level and thus are influenced by the local variations of  $\phi$  [107]. This gives a way to probe the local variation of  $\phi$  by measuring the FER as it is described in [107].

A characteristic  $dz/dV$  spectrum measured on a h-BN/Rh(111) valley and rim respectively is depicted in Fig. 2.20. It can be seen, that the spectra show distinctive differences between h-BN valley and h-BN rim in terms of the FWHM of the individual peaks. This effect is assumed to be caused by variations in the lifetimes of the respective states and is discussed extensively

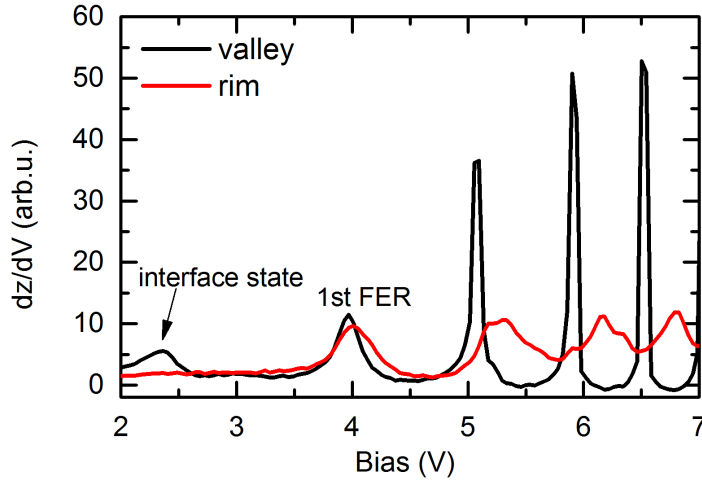


Figure 2.20 –  $dz/dV$  spectra of FER acquired with an STM on h-BN/Rh(111) on valley and rim. ( $I = 50$  pA (Constant current)). The position of the interface state and the first FER are indicated.

in the Ph.D Thesis of D. Rosenblatt from 2015 [130] and will not be discussed here. Another interesting effect is the occurrence of a peak at around +2.3 V when measuring in a valley position. This peak can be assigned to an interface state of the h-BN/Rh(0001) interface. A similar state was already reported in the literature for graphene/Ru(0001) [108]. It is, similarly to the case of graphene/Ru(0001) most prominent in the areas, which have the smallest distance to the metal substrate e.g. the valleys of the Moiré superstructure. The first FER resonance is thereby located at about + 4 V. From the FER on h-BN, a work function variation between valley and rim of about  $258 \pm 14$  meV could be extracted, which is in good agreement with results from photoemission [86]. It has to be noted, that for higher bias the Stark-shift is stronger, which might influence quantities like  $\phi$ . A strong dependence of the Stark-shift on the STM tip could be observed in the experiments. This might be caused by a modification of the effective electric field created in the tunnel junction due to different tip geometries.

In order to observe local changes in the FER, a series of  $dz/dV$  spectra were acquired in a line profile across a set of three valleys (h-BN) and analogous for two dark triangles and hexagons (IC-h-BN). The results are depicted as  $dz/dV$  maps (Fig. 2.21). For the standard h-BN phase one can see the interface state predominantly present at the valley region. The field emission resonances are modulated periodically with the valleys and rims. This is caused by the variations of the work function of about 260 meV between the respective areas of the Moiré pattern. For a similar line profile on IC-h-BN one can clearly observe a strong modification of the FER in the map. On the position of the hexagon, e.g. the position of the former valley of the

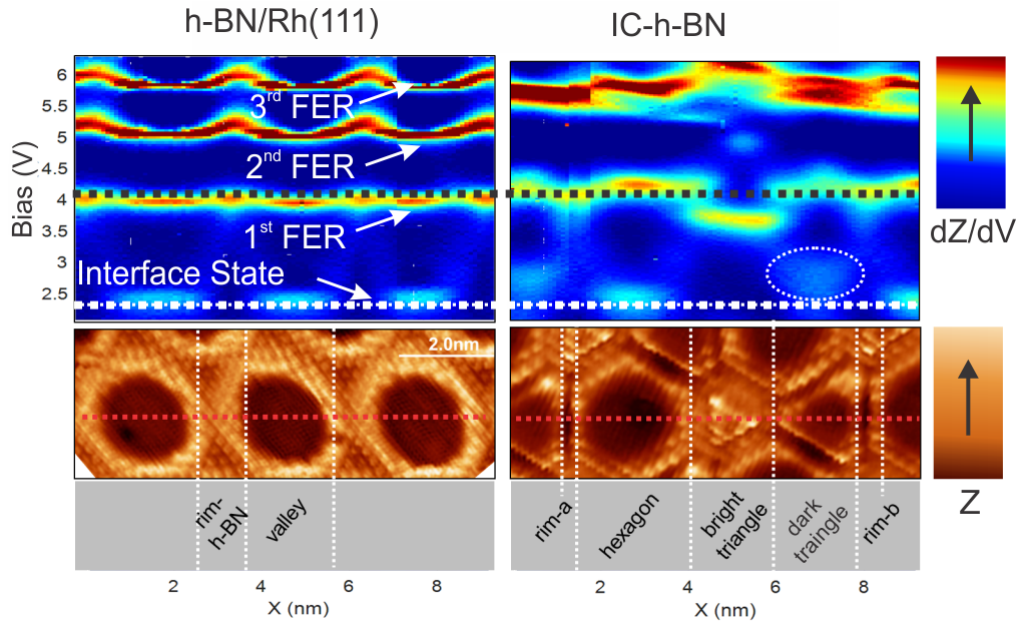


Figure 2.21 – Line profiles of the energetic position of the FER on h-BN(left) and IC-h-BN (right). The corresponding spatial positions are indicated in the STM topographs (red dashed line). Dashed black line: Position of the 1<sup>st</sup> FER (h-BN). Dashed white line: Position of the interface state (h-BN). Dashed white circle: New state at dark triangle position (IC-h-BN).

h-BN, the interface state as well as the first FER have a almost similar position (c.f. Fig. 2.21). The higher order FERs are shifted to higher energies by about 0.5 eV for IC-h-BN, most likely due to another tip geometry. This is indicated in Fig. 2.21 for the 2nd and 3rd FER. A similar effect was also discussed in [130]. The effect caused by a variation of the effective electric field inside the junctions is more prominent for the higher order FER since they are affected more strongly by a Stark Shift. Because of this, the absolute energetic positions of higher order FER resonances cannot be compared for different sets of measurements.

For the center of the dark triangle a new state at  $\approx 2.6$  V is observable. Its intensity is about half the intensity of the interface state of the hexagon. The occurrence of an state at this position implies that in contrast to the normal h-BN this area of the Moiré-pattern now has a modified interface to the underlying metal substrate. The accumulation of carbon underneath the h-BN might lead to the modification in the electronic structure, observed at the position of the dark triangle by introducing additional channels for charge transfer.

An additional modification of the electronic structure can be observed at the position of the bright triangle. Two resonances are visible at around +3.5 V and + 6.3 V, which might correspond to the FER of the h-BN/Rh(111) each shifted by about 500 meV. Furthermore in the gap between these peaks an additional state appears at about 5 V. Spatially the maximum of this state is strongly localized on the center of the bright triangle and has only about 50% of

the intensity of the 1st FER. An individual  $dz/dV$  spectrum at the center of the bright triangle furthermore reveals a state at 1.9 V (Fig. 2.22).

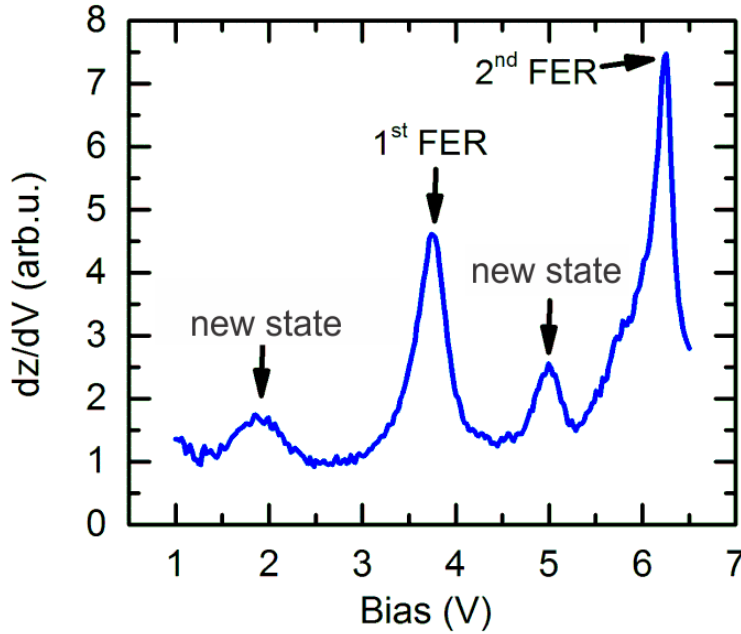


Figure 2.22 –  $dz/dV$  spectrum of FER acquired with an STM on the position of the bright triangle of IC-h-BN. ( $I = 50$  pA (Constant current)). The position of the individual peaks are indicated.

Without DFT simulations of the electronic structure (analogue to the analysis performed in [108] for graphene/Ru) of IC-h-BN, however it cannot be unambiguously determined at this point whether these peaks are FER resonances shifted due to a modified chemical environment or new interface states. These observations indicate a strong modification of the surface composition and especially of the interaction between the h-BN and the Rh substrate at this point. The large shift of the FER of about 500 meV and the resulting large change of  $\phi$  supports once more the hypothesis of carbon underneath the h-BN.

It was shown in the literature that the difference in  $\phi$  between graphene/Rh(111) and h-BN/Rh(111) is about 600 meV [131]. This could consolidate for small patches of carbon leading to the spatially confined work function modification. To further analyze the observed FER, their spatial extension was recorded in  $dI/dV$  maps for each energy at which a peak was observed. An area was chosen where two domains of h-BN and IC-h-BN meet. The resulting  $dI/dV$  maps are depicted in Fig. 2.23. It has to be noted, that the absolute positions of the FERs vary from those depicted in Fig. 2.21, since they were acquired with a (geometrically) different STM tip. The first FER of h-BN can be clearly observed at +4.5 V and at +3.5 to +4 V



for IC-h-BN. The second FER respectively at + 6 V (h-BN) and +5.5 V (IC-h-BN) (Fig. 2.23).

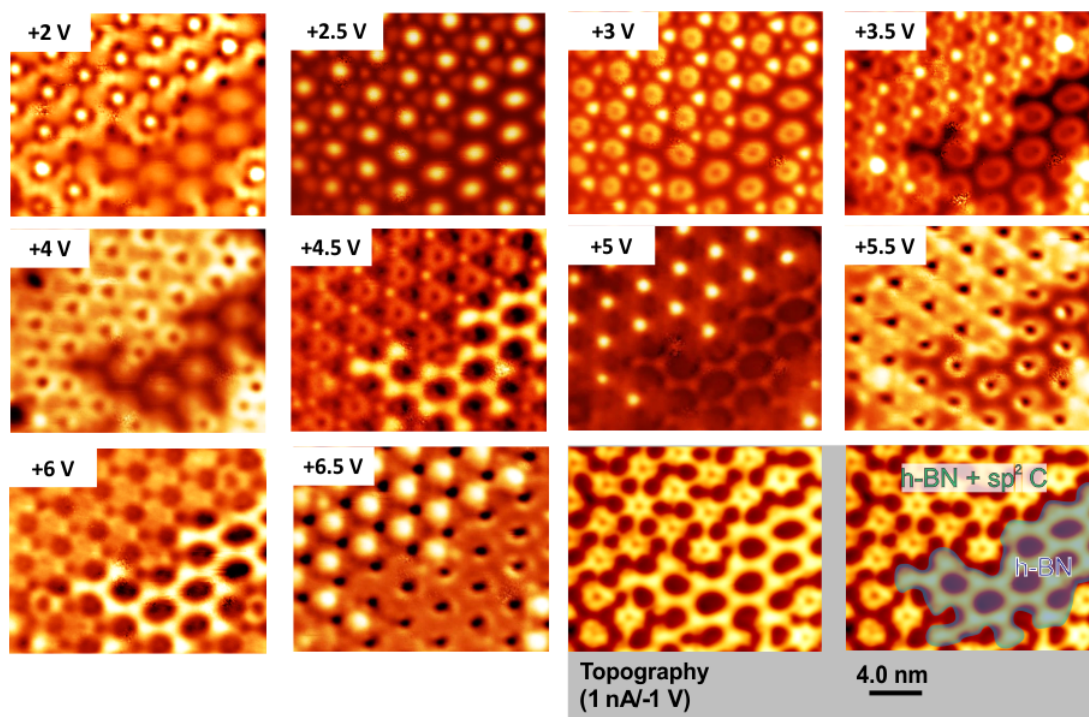


Figure 2.23 – Spatial mapping of the FER in  $dI/dV$  maps (Acquisition parameters: Setpoint  $I=50$  pA (constant height mode),  $U_{mod}=50$  mV,  $f_{mod}=832$  Hz) at the energy positions of the major resonances for standard h-BN and IC-h-BN. The corresponding STM topography of the area utilized for this measurement is depicted on the bottom right.

One can see that for some resonances, especially for the interface state of the h-BN valleys at + 2.5 V, both domains show a DOS with similar geometries. This observation supports the hypothesis that for IC-h-BN the hexagon is unmodified and carbon intercalates on the rim-sites. In contrast the modified interface state at +2 V can only be observed on the IC-h-BN and does not have a counterpart in h-BN. Similarly the state at +5 V is observed as a strongly localized DOS at the position of the bright triangles. Interestingly, the interface states of both phases and the state at +5 V are observed at similar energies as in previous measurements, whereas for the FER a small energy shift, most-likely because of tip variations, can be measured. This might hint at the fact, that also the state at +5 V is an interface state of the carbon/Rh interface.

### XPS on IC-h-BN/Rh(111)

XPS is a surface sensitive technique in which a sample is irradiated with X-rays and based on the photoelectric effect, electrons are extracted from it . It is commonly used to gain information on the elemental composition of a sample, as well as their chemical and electronic

state [132]. In a XPS measurement electrons are excited by the X-rays and removed from the core shells of the atoms. The excited electrons diffuse to the surface and subsequently leave the sample as photoelectrons. The kinetic energy of the extracted electrons is measured in a spherical analyzer, in which variable retarding voltages and electrostatic lenses are utilized to sort the electrons by their energy. Thus a spectrum of the electron kinetic energy is generated. The measured kinetic energy of the electrons also contains information on their binding energy which is specific for the element they originate from as well as the specific orbital they were bound in. Due to the penetration depth of about 10 nm, XPS is not purely surface sensitive but rather sensitive to the topmost atomic layers of the sample.

Since the photon energy of the X-Ray source is known (typically Al  $K_{\alpha}$  = 1486.7 eV or Mg  $K_{\alpha}$  = 1253.6 eV) the binding energy of the electrons can be derived according to:

$$E_{binding} = E_{photon} - E_{kinetic} \quad (2.2)$$

In order to get further insight in to the composition and origin of the IC-h-BN the so far utilized Rh(111) crystal has been transferred to another UHV setup equipped with X-ray Photoelectron Spectroscopy (XPS) and Ultraviolet-Photoelectron Spectroscopy (UPS) facilities. The sample was prepared in-situ in a UHV preparation chamber connected to the XPS set up following the procedures described earlier in this chapter. After the preparation the sample was transferred under UHV conditions to the XPS setup.

The utilized XPS was operated at a base pressure of  $1 \cdot 10^{-10}$  mbar. The measurements were performed with an Al-X-ray source emitting photons at 1486.7 eV. A resulting full range XPS spectrum of the kinetic energy, with all relevant peaks labelled is shown in Fig. 2.24.

The peaks indicated in the overview spectrum could be identified by comparison with literature values. No signature of additional elements apart from carbon present on the surface could be detected in the overview spectrum, strongly supporting the hypothesis of carbon being the source of the modified Moiré pattern. To further analyze the individual relevant peaks, detailed scans have been performed. These are depicted as spectra of binding energy in Fig. 2.25 a)-c). A nonlinear Shirley background function was subtracted from the data. The peak position, the full-width-at-half-maximum (FWHM) and total area under the peak was determined by fitting the respective peaks with a Gaussian-Lorentzian line shape using a fitting algorithm. The resulting values are denoted in the graphs in Fig. 2.25.

The nitrogen 1s peak was determined to be at 398.208 eV. This corresponds well to the value reported in literature [133].



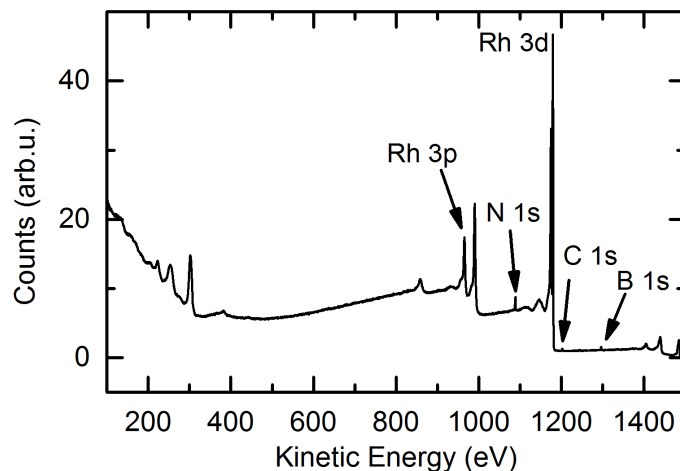


Figure 2.24 – Spectrum of the kinetic energy acquired by XPS on a IC-h-BN sample.

The characteristic carbon 1s peak for the IC-h-BN sample is located at 284.471 eV. For literature values from high resolution XPS measurements on graphene on Rh(111) the C 1s peak has been reported to split into two peaks one at 284.94 and one at 284.41 eV, caused by the buckled growth of graphene/Rh(111) and thus two different binding states of carbon<sup>2</sup>. For XPS measurements on pure  $sp^3$  carbon (diamond) a binding energy of the of about 290.45 eV, whereas for pure  $sp^2$  carbon (graphite) a binding energy of about 284.36 eV was reported [134]. The observed C 1s peak is shifted towards the binding energies reported for  $sp^2$  carbon or graphene/Rh(111). Thus a good hypothesis in the case of IC-h-BN might be, that the carbon is predominantly found in aggregates with  $sp^2$ -character at defined positions in the space between the rhodium surface and the h-BN layer. Since the utilized XPS-chamber does not allow for an in-situ transfer to a STM, the results could not be cross-checked with STM topography. This option is currently under construction and will be utilized to provide additional insight into this matter.

#### DFT model of IC-h-BN/Rh(111)

To rationalize the assumptions based on the experimental results, density functional theory (DFT) calculations of the resulting h-BN Moiré pattern under the presence of 1, 2 and 3 carbon-rings were utilized based on the model depicted in Fig. 2.26 a) and b). These simulations were performed by the group of Prof. Talat Rahman (University of Central Florida) in a collaboration on this project.

In the simulations the carbon rings were placed at similar symmetry points on the Rh(111)

<sup>2</sup>A measurement of an energy variation of this size is beyond the resolution limit of the utilized machine.

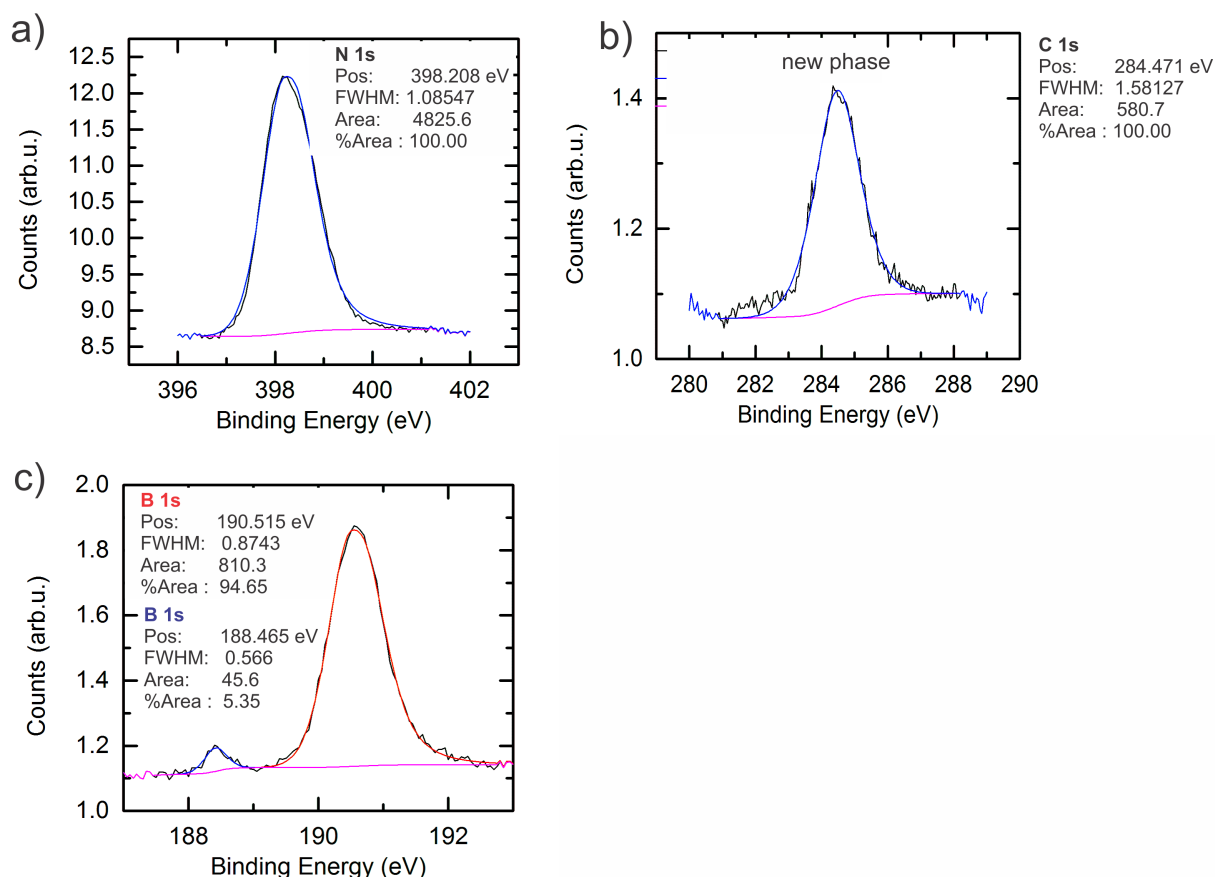


Figure 2.25 – Binding energy of the characteristic elements of a IC-h-BN sample measured by XPS. a)-c) The characteristic peaks in the binding energy of the elements C, N and B are depicted along with the corresponding fits and the resulting parameters for the energy position, FWHM and peak area.

surface (Fig. 2.26b)). In order to compare these results to the experimentally observed data, simulated STM images were created. These are depicted in Fig. 2.26c). Whereas for 1 phenyl ring per suggested binding site, barely a change in the simulated STM contrast is visible, distinct structures form for 2 and 3 phenyl rings. Clear structures of a triangular regions with high and low apparent height are found. The best agreement with the experimental data was achieved for 3 phenyl rings. A comparison between experimental data and DFT simulation is shown in Fig. 2.27. One can see, that the structures of the bright and dark triangles, as well as the hexagonal shape of the valley are reproduced very well.

Considering the experimental and theoretical results presented in this section, the origin of IC-h-BN can be related to intercalated carbon between the Rh(111) surface and the h-BN superlayer. After the growth of h-BN on Rh(111), the temperature of the metal substrate is gradually decreased. For a certain temperature range, carbon has the lowest solubility in

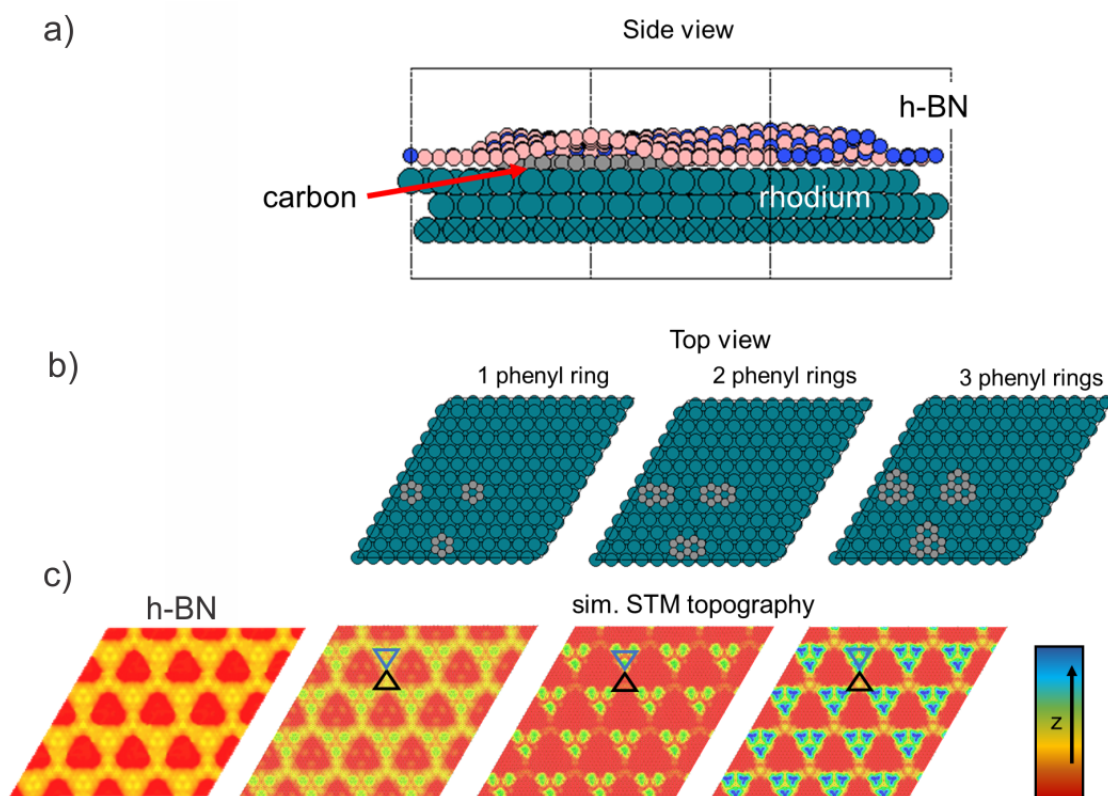


Figure 2.26 – a) Side view of model of IC-h-BN. b) Top view of the model used for the DFT simulations for 1, 2 and 3 phenyl rings. c) Simulated STM images based on the results of the DFT calculations for 1, 2 and 3 phenyl rings. The blue triangles indicate the position of the "bright triangle", the black triangles the position of the "dark triangle".

the Rh bulk and thus diffusion to surface of the Rh-crystal is promoted. Due to the strong interaction of the h-BN with the Rh(111) surface at the valley position, carbon accumulates at the rim-areas with the furthest distance to the metal substrate, resulting in the formation of a new Moiré-pattern. Since this is the equivalent of carbon intercalated between h-BN and Rh, we call this phase IC-h-BN.

### Pentacene on IC-h-BN/Rh(111)

As an additional experiment we investigated, if IC-h-BN has modified characteristics towards molecular adsorbates compared to h-BN. Since pentacene is a well understood model system and we studied its behavior on h-BN extensively, we also performed a similar study of pentacene on IC-h-BN. A STM topography image of the resulting sample surface of pentacene adsorbed on IC-h-BN/Rh(111) is depicted in Fig. 2.28.

The pentacene molecules again appear as rod-like objects when imaged in the energy range of the HOMO-LUMO gap. In contrast to h-BN, where their binding position was defined by the

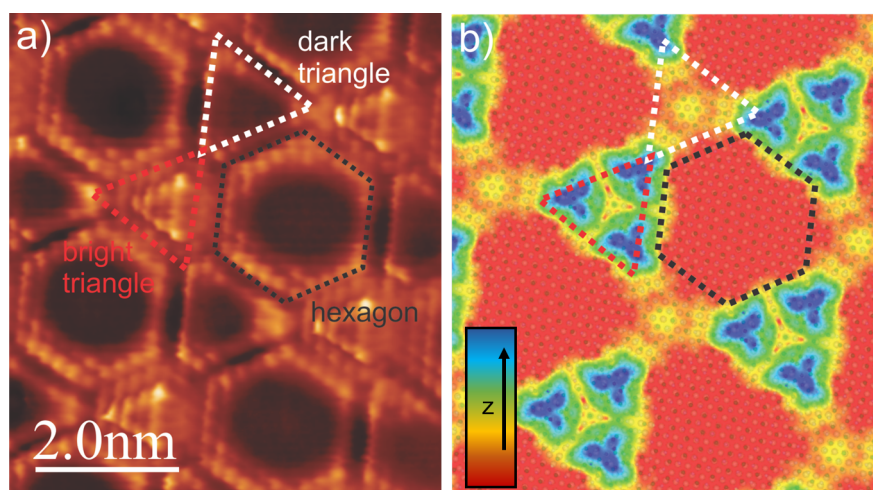


Figure 2.27 – a) High resolution STM topography image of IC-h-BN. The respective characteristic areas are denominated and indicated in the image. b) Simulated STM topography image based on a DFT calculation assuming three phenyl rings at every other h-BN rim site. The scaling and the indicated shapes correspond to those of the image depicted in a).

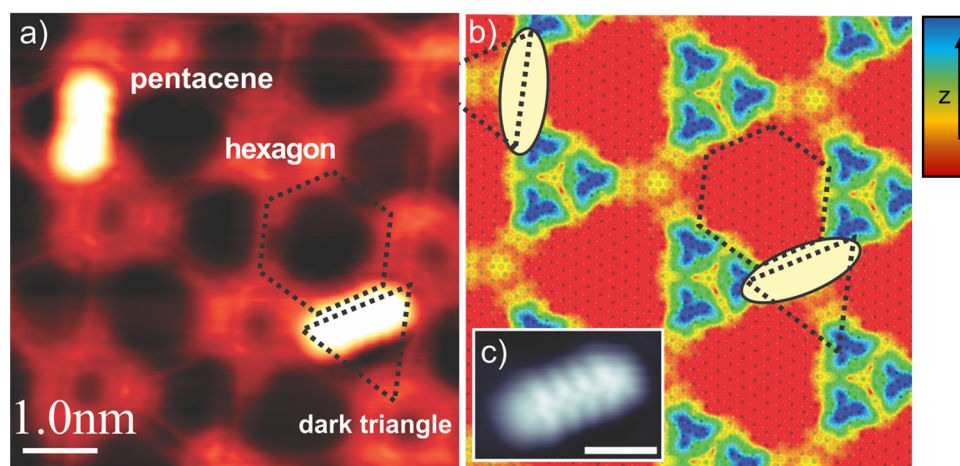


Figure 2.28 – a) STM topograph of pentacene on the Moiré-pattern of IC-h-BN (Acquisition parameters:  $U_B = -1$  V,  $I = 100$  pA). b) Adsorption position of pentacene indicated on simulated STM image of Moiré-pattern of IC-h-BN. c) STM constant height image of the orbital structure of the pentacene HOMO acquired as a  $dI/dV$  map. (Acquisition parameters:  $U_B = -2.1$  V,  $I = 100$  pA,  $U_{mod} = 50$  mV,  $f_{mod} = 832$  Hz)

dipole rings inside the h-BN valley, they are now almost exclusively found in the dark triangles. They adhere in such a way, that the long axis of the molecule is aligned in parallel to one of the triangle sides. In STS measurements it was possible to resolve the molecular resonances of HOMO and LUMO with a similar gap as for h-BN/Rh(111) as well as their orbital structure (c.f. Fig. 2.28 c)).

This indicates that the decoupling capability of the binding site of the pentacene of the dark triangle is similar to the valley. The modified adsorption position might originate from the fact, that the dipole ring of the h-BN was modified due to the carbon formation underneath the h-BN layer or due to a small geometric change of the h-BN valley. The latter seems unlikely since the area of the dark triangle is smaller than the area of the hexagon. If and to what extent the dipole-ring of the original h-BN valley has been modified cannot be determined at this point. A more plausible explanation is a local modification of the reactivity of the surface due to the increased gradients in the local  $\phi$  introduced by the carbon. Analogous to the trapping potential of the dipolar rings of the h-BN Moiré formed by the work function differences between valley and rim, this local gradient of  $\phi$  at the observed adsorption position might generate a similar attractive potential.

## 2.5 Conclusion part II

In conclusion we could show, that we can steer the growth of an additional Moiré-pattern of h-BN/Rh(111) by modifying the amount of carbon impurities in the subsurface layers of the Rh(111) substrate. By means of high resolution STM and STS in combination with XPS measurements and the support of DFT it could be shown, that the structure originates from small domains of  $sp^2$ -carbon forming at specific registries with the substrate at the position of the highest distance between h-BN and Rh(111) substrate. The observed work-function variations, probed via the FER, could be shown to affect the local reactivity of the surface. This results in altered adsorption geometries of small molecular species. In order to get a deeper understanding of this process further theoretical models will be utilized in the future to especially clarify the origin of the individual electronic states.



### 3 The building blocks of peptides - Single amino acids on surfaces

The study of functional biological molecules, such as peptides and proteins on (inorganic) surfaces by means of high resolution STM and STS has been an emerging field in the recent years. This was demonstrated on a broad range of investigations on small natural peptides and proteins such as studies on the assembly of cyclic peptides [135], the formation of aggregates of peptides and lipids [136], the assembly of small dipeptides on metal surfaces [11] and the folding of proteins on metal surfaces [36]. Especially to rationalize the final conformations of folded peptides on surfaces [37] the chemical properties of the individual amino acids and their individual interactions play a crucial role. Good examples for the role of the specific interactions of amino acids, such as for example hydrogen bonding, are the formation of specific conformational motifs, like the  $\alpha$ -helix or the  $\beta$ -sheet [23][137]. The self assembly of peptides on surfaces [15, 22, 138] is determined by their amino acid sequence and its interaction with the underlying substrate. The 20 proteinogenic amino acids exhibit a broad chemical diversity [71] and thus are interesting model system for a broad variety of effects. The ability of amino acids to form ordered structures at metal surfaces was studied in 1978 by Atanasoska et al. [139] using low-energy-electron diffraction (LEED). Another important aspect of the self-assembly of amino acids on surfaces is their specific chemical form. The chemical form of amino acids can, depending on their immediate environment (e.g. the metal substrate), vary between a acidic, cationic, zwitterionic or neutral [140] and thus facilitate different bonding schemes. A number of STM studies were performed, such as for the example of L- and S-proline on Cu(110) [141] and D- and L-methionine on Au(111) [142], where the self-assembly of the structure on the surface was determined by the chirality of the building blocks. For L-tryptophan on Cu(111) [143] the assembly of tightly packed structures driven by the intermolecular hydrogen bonds and the  $\pi$ -stacking of the indole residues was observed. The specific adsorption of L-cysteine to surfaces via its thiol groups was investigated on Si(111) [144] and Au(111) [74]. On behalf of these examples it can be seen that amino acids on surfaces offer a vast research field to study the diversity of self-assembled structures.

## Chapter 3. The building blocks of peptides - Single amino acids on surfaces

---

In this chapter basic studies by means of high-resolution STM and STS on the characteristic assemblies of the amino acids phenylalanine, tryptophan, arginine and proline on metals are presented. As a second part, the possibility to attach specific amino acids to the STM tip is presented. It is shown that characteristic motifs of the respective amino acid assemblies on the surfaces are identified and moreover utilizing amino acid functionalized STM tips their electronic structure could be assessed.

### 3.1 Phenylalanine

L-phenylalanine (Phe) is a proteinogenic amino acid with a functional residue consisting of a phenyl ring [22] and thus exhibits an aromatic and hydrophobic character (c.f. chapter 1.3). The chemical structure of Phe is depicted in Fig.3.1 a). By measuring the atomic distances within a chemical drawing software one can approximate the length of the Phe molecule to about 0.85 nm.

In the experiments presented here an atomically flat Cu(111) surface was employed. The surface was prepared by subsequent cycles of  $Ar^+ - ion$ - bombardment ( $E_{kin}=1$  keV,  $p_{Arg} = 1 \cdot 10^{-6}$  mbar) and annealing to 550°C for 5 min. The L-Phe was bought as an enantiomer pure powder with a purity of >99% from Sigma-Aldrich. Utilizing a molecular evaporator (Dodecon), the molecules were sublimed in-vacuo onto the clean Cu(111) surface. The successful (intact) sublimation and its onset temperature could be determined using a mass-spectrometer. The sublimation temperature range could be determined to approx. 118°C to 130°C. Subsequently the deposition parameters were adjusted via STM measurements to a low submonolayer coverage. An overview STM image is depicted in Fig.3.1a).

On the surface mainly three molecular species can be found (Fig.3.1 c) - e)). According to their respective dimensions, symmetry and the number of observable constituents, one can deduce, that these are dimers (c)) and tetramers (e)). This is visualized by superimposing high resolution STM images with the chemical structure of Phe. The aggregate depicted in (d)) cannot be clearly assigned to a specific number of constituents. Most-likely these structures consist of three Phe units (trimers). This was estimated by comparison of the aggregate size to the size of the tetramers, which is about 25% larger. However this might also be related to a variation in the adsorption geometry of the individual Phe units.

The dimers appear as rod-like structures with two bright protrusions at the outside and an area of lower apparent height in the center. The bright protrusions can most-likely be allocated to the phenyl-rings of Phe. Based on the calculations presented in [145] it is likely that the amino group binds to the surface. The elevated binding geometry of the phenyl ring results in the bright protrusion observed in STM topography. The observed structure fits well to the structure reported by Lingenfelder et al. [11] for the dipeptide consisting of two Phe adsorbed



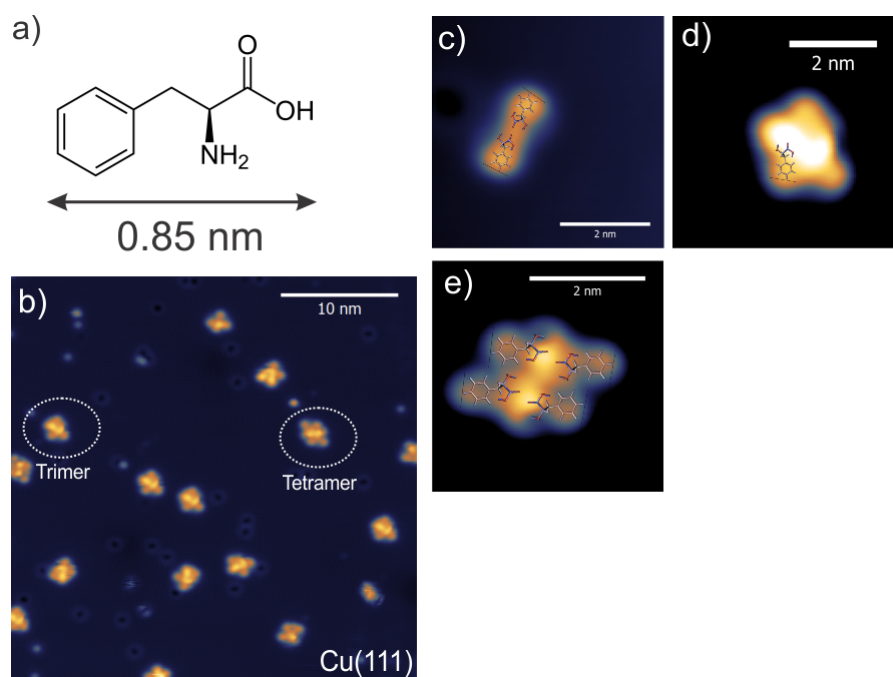


Figure 3.1 – a) Chemical structure of Phe and its length. b) Overview STM image of Phe deposited on a Cu(111) surface. Exemplary the position of a Phe tetramer and a trimer is indicated. c)-e) Detailed STM images of dimer (c)), unspecific aggregate (d)) and tetramer (e)) superimposed with structural formula of Phe in tentative models. (Acquisition parameters: b)-e)  $U_B = 1\text{ V}$ ,  $I = 200\text{ pA}$  (constant current))

on Cu(110). The Phe units in the present case are not interconnected via a covalent peptide bond. Nevertheless might the similar appearance in STM topography hint at an analog binding motif to the one suggested in [11] for Phe-Phe.

The most common species at low coverages is the trimer. For higher coverages, the tetramers are preferred. The trimers exhibit a central L-shaped region with elevated apparent height, which generates a chiral assembly. Using this feature one can observe that the trimers adsorb in three distinct orientations on the surface as it is shown in Fig.3.2 a)-c).

Most likely the observed adsorption geometry is governed by the interaction, of the Phe with the underlying Cu(111) substrate and represents the three crystallographic directions of the surface. As shown in studies by Forster et al. for S-proline on Cu(110)[146] and extensively described by Barlow et al. [140] an important factor, which might lead to a certain bonding geometry of the individual amino acid units, is the chirality on the surface and furthermore the so called organisational chirality [140]. It can be seen that only one enantiomer of the trimers can be found on the surface, which hints at a preservation of the chirality of the Phe on the surface and furthermore a chirality induced organization to the tetramer structures.

The Phe tetramers appear in a rhomboid shape with two central lobes arranged in a linear

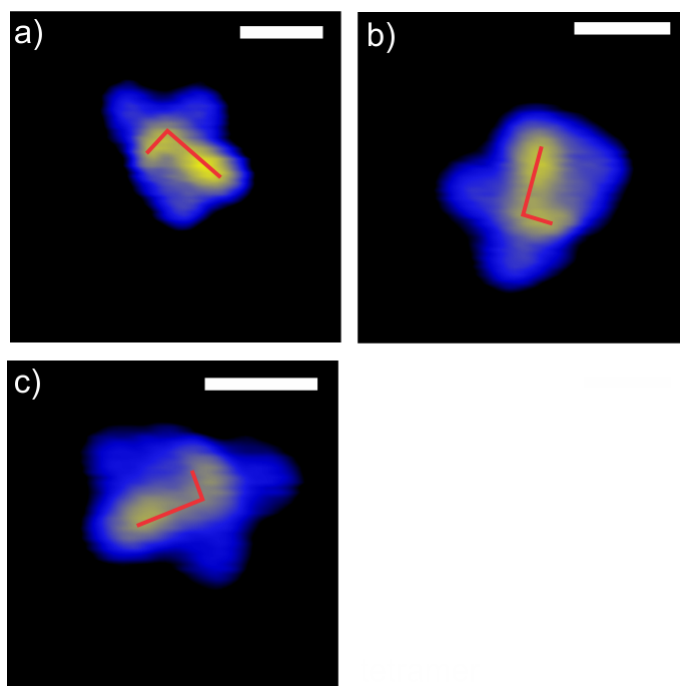


Figure 3.2 – a)-c) Detail STM topography images of Phe trimers. Their specific orientation is indicated by the red L-shaped line.  $U_B = 1\text{ V}$ ,  $I = 200\text{ pA}$  (constant current). All scale bars correspond to 1 nm.

geometry (Fig.3.2 d)) and correspond well to two times the size of the dimer. Interestingly the Phe units in the tetramers (and in the trimers) seem to bind in a different fashion to the surface as in the case of the dimers, since they express a single elevated region in the center. In contrast to this the endpoints of the dimers were the regions of highest apparent height. This variation might be caused by the lateral interaction of the polar amino groups of the individual Phe units in the trimers and tetramers. In general a geometry was suggested where the polar residues of the Phe units are facing each other and thus can engage polar non-covalent interaction such as hydrogen bonding, whereas the unpolar phenyl residues are facing outside (c.f. Fig.3.1). A similar motif was reported for the folding of natural peptides on surfaces imaged by STM in [13]. For the dimers and tetramers also a threefold adsorption geometry on the Cu(111) surface can be observed.

In general, Cu (111) is a relatively reactive substrate compared to other noble metal (111) [147] surfaces and thus molecular adsorbates bind strongly to it. This enables STM imaging even at higher bias voltages (in the range of  $U_B \approx \pm 2\text{ V}$ ), without displacing molecular adsorbates. However, the strong interaction with the substrate comes at the cost of poor resolution in STS. Molecular features are typically broadened, due to the hybridization with the electron bath of the metal [35, 85] making an observation difficult.

In order to gain access to spectroscopic features, we have worked on decoupling the molecules from the metal substrate by means of a thin dielectric layer. In literature it was shown, that  $C_{60}$  amongst others can act as a suitable decoupling layer with a band gap of more than 1 eV [148] for molecular systems. Smooth  $C_{60}$  layers can be grown in a very straight forward way via thermal sublimation of the  $C_{60}$  molecules in a molecular evaporator onto a clean Ag(111) substrate. A flat Ag(111) surface was prepared by subsequent cycles of  $Ar^+$  – ion-bombardment ( $E_{kin}=1$  keV,  $p_{Arg} = 1 \cdot 10^{-6}$  mbar) and annealing to 530°C for 5 min.  $C_{60}$  grows in a layer by layer growth (Frank–van der Merwe) mode [149]. For an approximate coverage of about 1.5 monolayers,  $C_{60}$  was sublimed at 510°C within several minutes. Exemplary a resulting STM image of an area with a bilayer of  $C_{60}$ /Ag(111) and corresponding height profile is shown in Fig.3.3 a) and c), a high resolution STM image depicting the individual  $C_{60}$  molecules in Fig.3.3 b).

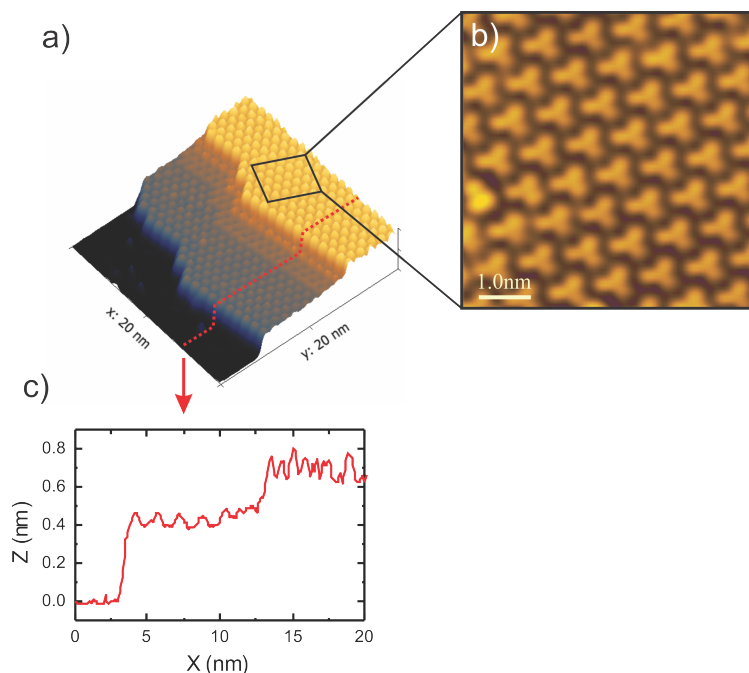


Figure 3.3 – a) STM topograph of a bilayer  $C_{60}$  deposited on a Ag(111) surface. The black square represents the dimensions of the high resolution STM image depicted in b). The red dotted line indicates the height profile depicted in c). (Acquisition parameters:  $I=30$  pA,  $U_B=-2$  V)

The  $C_{60}$  molecules appear mostly as three lobe structures and exhibit a surface roughness of less than 50 pm in a close packed layer [149]. Phe was deposited onto the  $C_{60}$  in a similar way as before. The result is depicted in Fig.3.4.

### Chapter 3. The building blocks of peptides - Single amino acids on surfaces

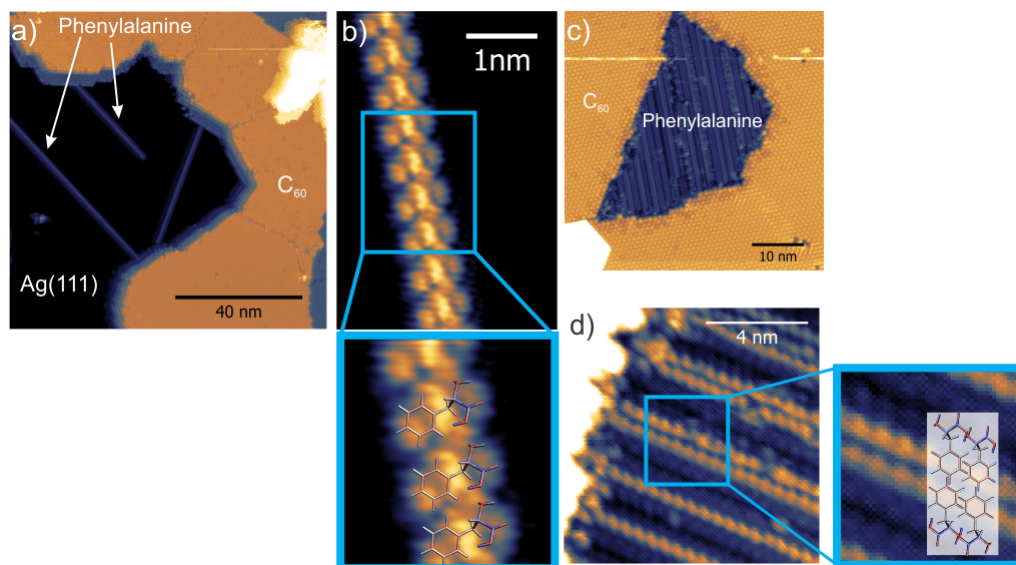


Figure 3.4 – a) STM image of linear structures of Phenylalanine grown on the Ag(111) surface for a low coverage of Phenylalanine. b) Detail of linear Phenylalanine cluster. The inset shows a zoom-in on the image with an overlay of the chemical structure of Phenylalanine to visualize possible arrangement within the linear assembly. c) Resulting assembly of Phenylalanine on Ag(111) for higher coverages. d) Zoom-in on Phenylalanine assemblies for higher coverages. The inset shows a zoom-in on the image with an overlay of the chemical structure of Phenylalanine to visualize possible arrangement within the assembly. (Acquisition parameters (a-d)):  $I=30$  pA,  $U_B=-1$  V)

As shown in Fig.3.4a), no ad molecules are found on the C<sub>60</sub> layer but well ordered chains can be observed at the boundaries of the C<sub>60</sub> islands. Phe seems to be too mobile on the C<sub>60</sub> films and thus it is diffusing to the bare Ag surface instead. The diffusion length of Phe is at least of the order of a couple of 100 nm because no molecules can be found even on extended C<sub>60</sub> islands. Lowering the sample temperature during the deposition of Phe to liquid nitrogen ( $LN_2$ ) lead to a similar result, demonstrating that the diffusion length of Phe still exceeds the typical size of the C<sub>60</sub> islands. Acquiring high-resolution STM images of Phe on Ag(111) reveals that the observed structures match well in size with linear aggregates of Phe. It should be noted that the structure as shown in Fig.3.4 b) is a suggestive model. Increasing the coverage of Phe leads to a saturation of the free patches of exposed Ag(111) surface (Fig.3.4c,d)), but does not lead to the adsorption of Phe on the C<sub>60</sub> layer. These results imply, that C<sub>60</sub> is not a suitable decoupling layer within the accessible temperature range during the deposition, to enable STS experiments on Phe because it does not exert sufficient interaction with the amino acid to immobilize it.

## 3.2 Tryptophan

The results obtained from the experiments performed with Phe indicated that surfaces which are too reactive (Cu(111)) and those which are too inert ( $C_{60}$ ) only allow limited access to topographic and spectroscopic features of adsorbed molecular species. For surfaces which are too inert, the large diffusion length of the molecules on the surface inhibits the observation of individual molecules. For strongly interacting surfaces the electronic features cannot be observed due to strong hybridization. As a less reactive substrate Au(111) [147] was utilized. Furthermore Soe et al. showed in 2009 for pentacene adsorbed on Au(111) [111], that it is possible to observe the topography as well the orbital structure of pentacene adsorbed on Au(111). This suggests, that Au(111) is inert enough to enable STS but still allows for the observation of individual molecules. Au(111) was prepared in an analogue way to the Cu(111) surface.

As a second amino acid, L-tryptophan (Tryp) was investigated. Tryp is an aromatic amino acid with an indole ring system as functional residue [22]. For large protein systems such as the photosystem or membrane proteins, Tryp was reported to predominantly mediate specific H-bridges and interaction with cations at the outer perimeter of the protein and thus act as a stabilizing agent [150][151]. Its size estimated on behalf of its chemical structure is about 0.9 nm along its long axis (c.f. Fig.3.5a)). For Cu(110) [152] and Cu(111) [143] surface Tryp has been investigated in STM experiments published in literature. There it was shown, that for these surfaces the functional groups of Tryp bind to the surface resulting in a flat adsorption geometry. In a similar way as described for the Phe sample, Tryp was obtained as highly pure powder (>99%, Sigma-Aldrich) in an enantio pure form and was deposited by evaporation at 210°C in vacuo.

Fig.3.5 b) and d) depict overview STM images of Tryp on Au(111) for high coverage ( $t_{deposition} = 60$  s) and lower coverage ( $t_{deposition} = 30$  s) respectively. For the high coverage (Fig.3.5b)) the most common structures are square like aggregates, which can also interconnect into bigger row-like superstructures. A detailed scan (inset: (Fig.3.5b)) of these square structures shows, that they consist of four repeating elements, each rotated by 90° (Fig.3.5c), the shape of a building block is indicated in red). Every sub-unit fits well in size and shape to the slightly bent structure of Tryp originating from the geometry of the indole-residue.

Lowering the coverage leads to individual equally distributed clusters with a typical more rounded shape as shown in Fig.3.5d). It can be seen in Fig.3.5e) that two of the observed features of these aggregates are similar to the building blocks of the square clusters. However, the two remaining constituent have a different appearance. An altered STM topography of the constituents might imply a varied adsorption geometry of these building blocks medi-

### Chapter 3. The building blocks of peptides - Single amino acids on surfaces

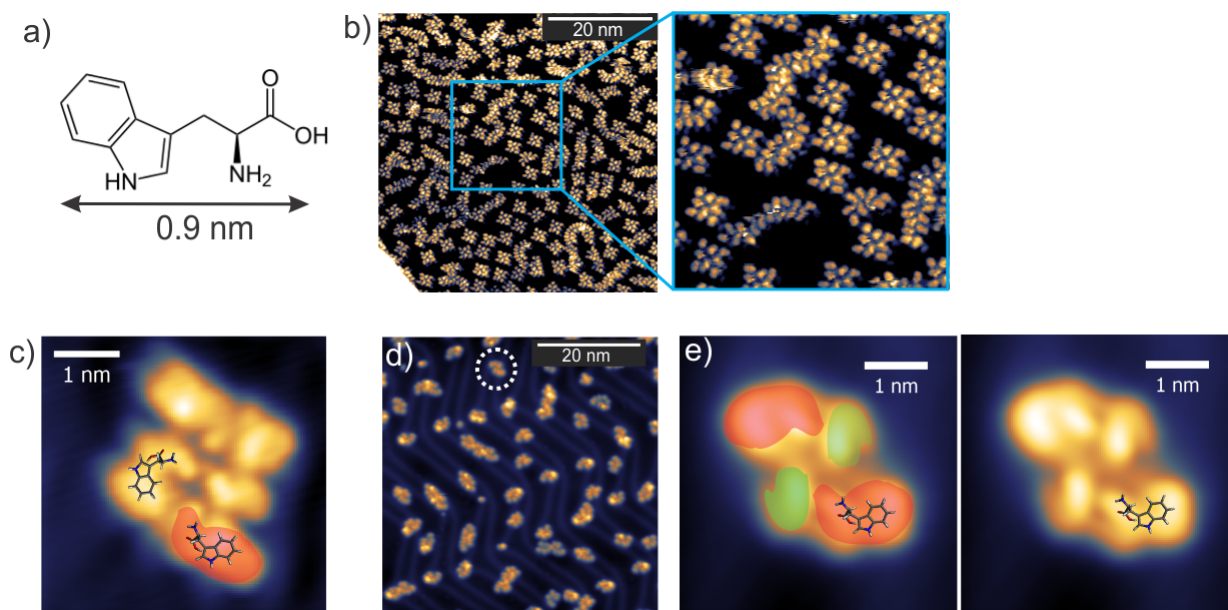


Figure 3.5 – a) Chemical structure and size of L-Tryp. b) STM image of a high coverage of L-tryptophan deposited on Au(111). Blue square depicts area of zoomed in STM image depicted in the inset. (Acquisition parameters:  $U_B = -1$  V,  $I = 50$  pA). c) Characteristic Tryp aggregate for high coverage, superimposed with structural formula of Tryp (Imaging parameters:  $U_B = -1$  V,  $I = 50$  pA). d) STM image of a adjusted coverage of Tryp deposited on Au(111). The white dotted circle indicates a Tryp aggregate as depicted in d) (Imaging parameters:  $U_B = -1$  V,  $I = 50$  pA). e) Characteristic Tryp aggregate for low coverage, superimposed with structural formula of Tryp. The two sets of building blocks are indicated by the colored areas in the left image. For visibility the right image depicts the STM topography without the color coded areas. (Imaging parameters:  $U_B = -1$  V,  $I = 50$  pA).

ated either by a variation in the molecule-substrate interaction or the interaction with the neighboring Tryp molecules. To clarify this however, a distinct simulation by means of DFT or MD is necessary. The model as it is shown in Fig.3.5 suggests that the Tryp molecules are arranged in such a way that the indole residue can engage in polar interaction with the carboxylate groups of the neighboring Tryp. Studies of L-Tryp on Cu(111), Cu(100), Cu(001) [139, 143, 152] for higher coverages of Tryp show that ordered networks are formed with a similar arrangement as observed for the square clusters (Fig.3.5e)). The reported networks are further stabilized by  $\pi$ -stacking [143] and intermolecular hydrogen bridges. For Tryp adsorbed on Au-nanoparticles [153] it was stated that both the indole and the carboxylate group of Tryp bind to the surface, which is in good agreement with our STM data.

The clusters observed in the experiment on the Au(111) surface exhibit a certain mobility on the surface and are prone to rotation or displacement upon scanning with elevated  $U_B$  ( $\approx 2$  V) or currents ( $\approx 500$  pA) indicating a rather weak interaction with the substrate but due



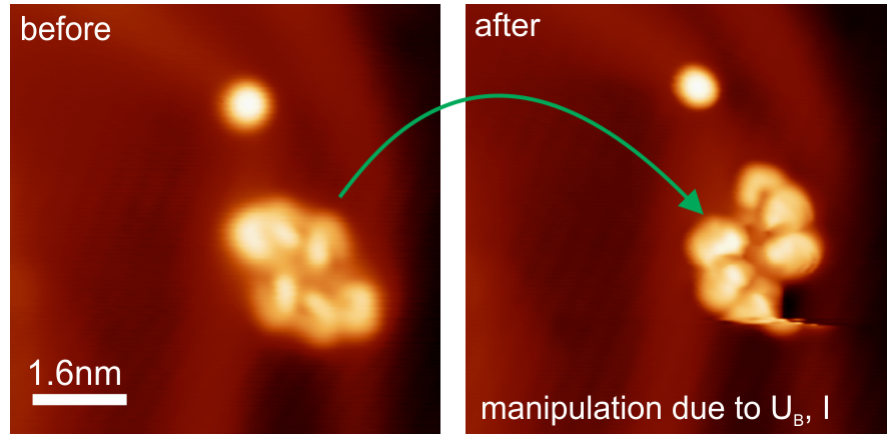


Figure 3.6 – Manipulation of Tryp cluster on Au(111) due to sweep of  $U_B$  in the range of  $\pm 2$  V around  $E_F$  at a setpoint of 500 pA.

to the preservation of the structure of the assembly a rather strong interaction in between the individual Tryp units.

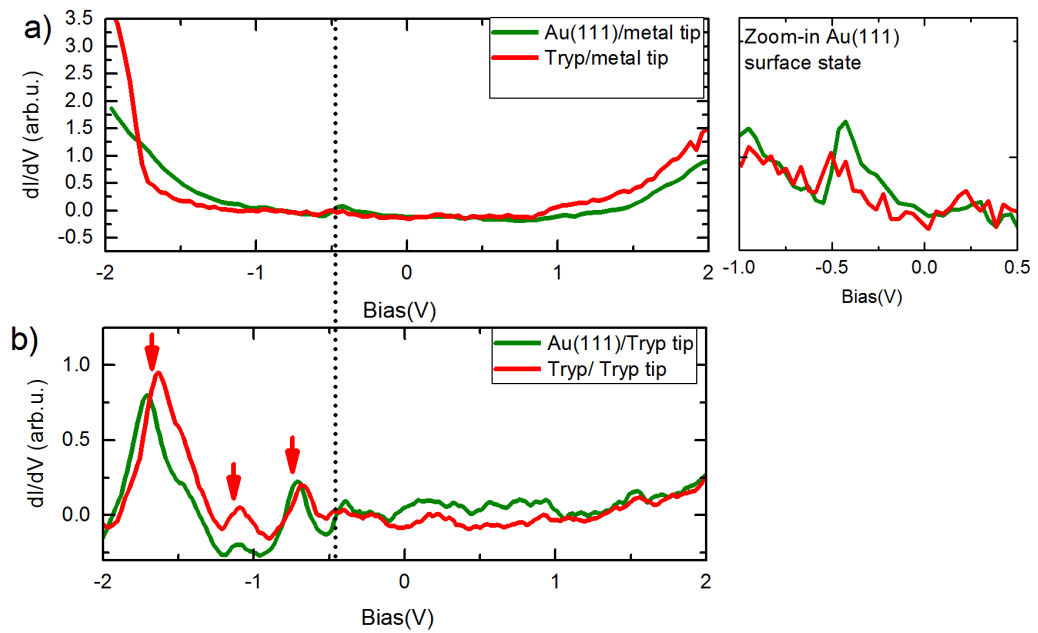


Figure 3.7 – a) STS measurement on Au(111) (green) and Tryp tetramer (red) using a metal tip. Acquisition parameters:  $I = 100$  pA,  $U_{mod} = 50$  mV,  $f_{mod} = 832$  Hz. The curves have been smoothed using a Gaussian filter for better visibility. The inset shows zoom-in on Au(111) surface state b) Measurement on Tryp tetramer (red) and Au(111) (green) with Tryp functionalized tip. The red arrows indicate positions of characteristic resonances. The vertical dotted black line indicates the position of the surface state of Au(111). Acquisition parameters:  $I = 50$  pA,  $U_{mod} = 50$  mV,  $f_{mod} = 832$  Hz.

### Chapter 3. The building blocks of peptides - Single amino acids on surfaces

---

The STS measurement on the bare Au(111) substrate (c.f. Fig.3.7 a)) shows a parabolic behavior and at -0.45 V a step in the differential conductance. This feature originates from the Shockley surface state of the Au(111) surface and its energetic position is in good agreement with values reported in literature [154]. The unperturbed observation of this characteristic feature without the abundance of additional resonances is used as a benchmark to determine, if the tip is metallic. On a Tryp tetramer the STS measurement is mostly featureless apart from the surface state of Au(111), an increase in the differential conductance around -1.8 V and a small step at + 0.9 V. In order to be more sensitive towards certain molecular resonances, the possibility of functionalized STM tips was investigated. Therefore, a Tryp tetramer was picked up by continuously approaching the tip to the surface for  $U_B \approx -1$  to  $-1.5$  V until a jump in the observed tunneling current is visible. Investigating the surface area by STM topography indicates the absence of the Tryp cluster. Performing a STS measurement after this experiment, results in the data depicted in Fig.3.7b). The green curve is measured on the Au(111) surface. One can see that the surface state of the Au(111) is visible. However, additional peaks are observed at -1.7 V, -1.1 V and -0.7 V. This confirms that the STM tip was most likely modified. A similar behavior in STS can be observed, when measuring on a Tryp tetramer (red curve). The dominant peak at -1.7 V is slightly shifted and has an about 10% increased intensity and the surface state cannot be observed on the Tryp tetramer. This implies, that the tip functionalization might play a crucial role in the observation of the molecular resonances, however the resonances cannot be assigned unambiguously in the present case. The multitude of observed resonances in the STS might hint at a rather undefined tip functionalization probably caused by the adsorption of a Tryp cluster to the tip. In order to gain the maximum control over the tip functionalization process it is favorable to minimize the cluster size, ideally to individual molecules and develop a proper protocol for the controlled adsorption of a molecule to the tip apex.

The formation of clusters, as depicted above, is facilitated by their diffusion length. Thus, a well established way to limit the clustering on a surface is reducing the thermal energy of the adsorbates by reducing the substrate temperature. This was demonstrated for individual atoms [57] and larger molecular species [35]. Here, we cooled the Au(111) sample during the deposition process to approximately 77 K. The resulting two most common species are depicted in Fig. 3.8. As before, aggregates consisting of four Tryp units can be observed. Additionally, it is possible to observe a new structure, which can be identified as dimers (c.f. Fig.3.8 b)).

It was possible to acquire high resolution images of these dimer structures (c.f. inset Fig.3.8 b)) utilizing a functionalized tip. These scans revealed intra-molecular contrast. Furthermore the respective monomers exhibit a characteristic curved shape. In order to further understand the



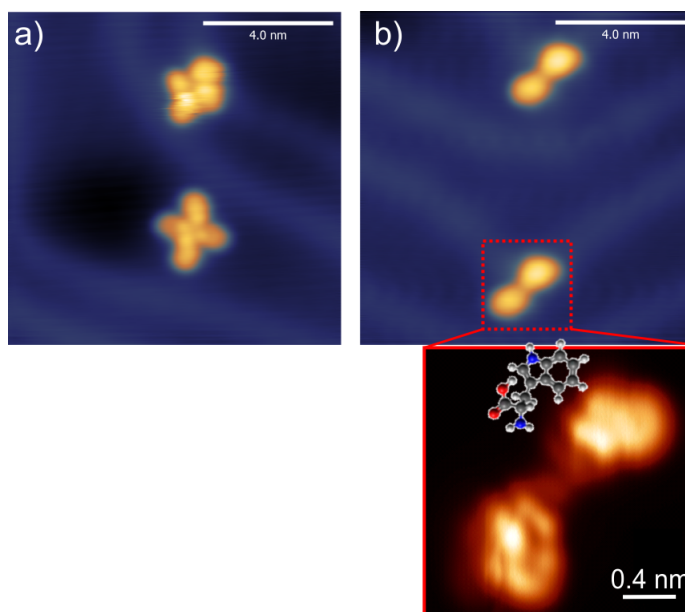


Figure 3.8 – a) and b): Resulting structures of Tryp/Au(111) for a deposition onto a pre-cooled sample surface ( $\approx 77$  K) (Acquisition parameters:  $U_B = -1$  V,  $I = 50$  pA). The inset of b) depicts a high resolution constant height scan of the framed structure superimposed with suggested geometry of Tryp (Acquisition parameters:  $U_B = 10$  mV, Setpoint:  $I = 50$  pA).

tip functionalization process a protocol for a controlled decoration of the tip was implemented. As a first step a metallic tip was prepared by means of voltage pulses or controlled indentation into the metal substrate followed by subsequent STS measurement on a bare metal. The pick up process was performed in a similar way as described above. Subsequently to the pickup process, topographic images and STS measurements revealed the success of the functionalization as depicted in Fig.3.9 a). The white arrow indicates the position of the picked up Tryp unit. After the functionalization changes in the inner contrast of the remaining structures on the surface are visible, most-likely due to the altered geometry of the tip apex. Furthermore, STS measurements on Au(111) with the modified tip revealed the success of the functionalization. Apart from the surface state of Au(111) at  $\approx -400$  meV, a strong resonance at  $-1.7$  V is visible most likely originating from the Tryp adsorbed at the STM tip. Repeating the STS measurement on Tryp cluster with this tip, it was possible to resolve two distinct peaks below and above  $E_F$ .

Although the absolute energetic positions of HOMO and LUMO of a molecular species on a surface are influenced strongly by e.g. the specific hybridization and  $\phi$  of the substrate [113], the observed resonances most likely corresponding to the HOMO ( $U_B = -1.7$  V) and LUMO ( $U_B = +1.8$  V) of Tryp by comparison with values for Tryp on Cu(111)[143] and on for Tryp on Gold nanoparticles [153]. The HOMO at  $-1.7$  V furthermore corresponds well to the most

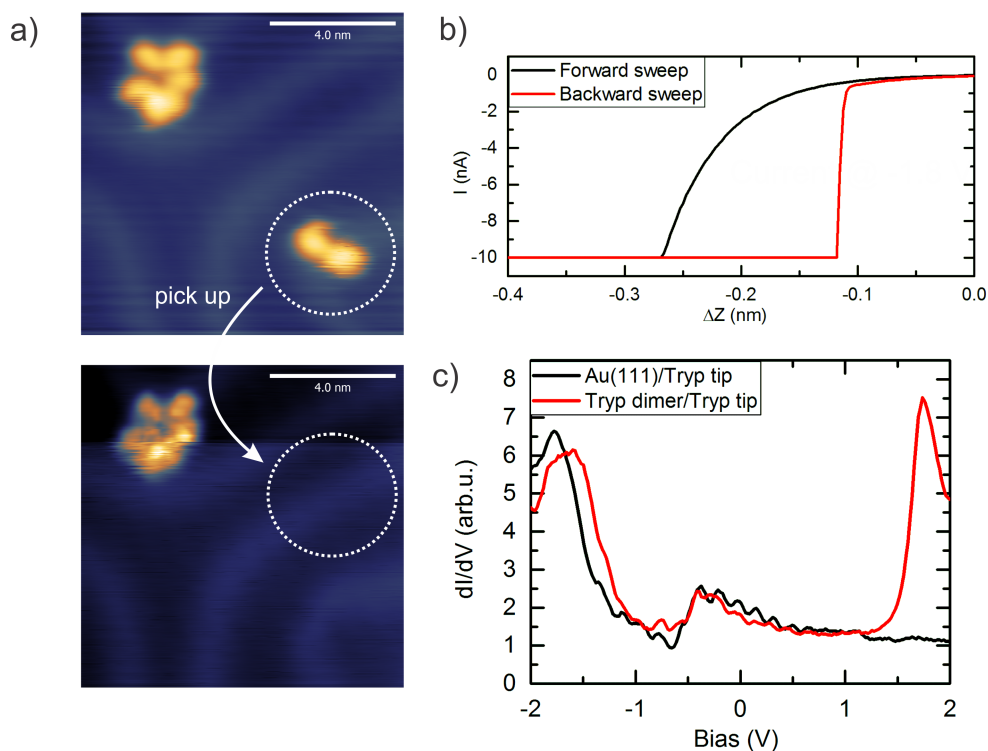


Figure 3.9 – a) Pick up of Tryp dimer. (White arrow indicates former position of Tryp dimer)(Acquisition parameters:  $U_B = -1$  V,  $I = 50$  pA). b) Corresponding  $I(z)$  curve, indicating the tip modification in the backward sweep. c) STS measurement on Au(111) and Tryp dimer with Tryp functionalized tip. ( $I = 50$  pA,  $f_{mod} = 832$  Hz,  $U_{mod} = 50$  mV).

dominant peak observed in previous measurements. The other resonances observed for a Tryp cluster at the tip apex could not be reproduced and thus are most likely caused by an undefined composition of the tip apex. From the observation presented in this section, we can conclude that the application of a well defined Tryp functionalized STM tip, enables the observation of the molecular energy levels of Tryp deposited on a Au(111) surface.

### 3.3 Arginine

Following a similar protocol as previously described for Tryp, L-arginine (Arg), bought as an enantio pure powder from Sigma Aldrich (Purity > 99%), was studied on a Au(111) surface. Arg is a polar amino acid with a guanidine residue as functional group and thus exhibits a basic and hydrophilic character [22]. Its chemical structure is depicted in Fig.3.10 a).

Arg was deposited onto a clean Au(111) surface by thermal evaporation at  $180^\circ\text{C}$  for  $t = 30$  s leading to a typical sub-monolayer coverage as depicted in the STM overview scan in Fig.3.10 b). Characteristic aggregates consisting of four circular features can be observed (Fig.3.10c)). The four features can be divided into a set of two smaller features with an apparent height of

about 1.5 Å and a set of two larger features with an apparent height of 1.8 Å. These two sets of circular features are spaced about 1 nm apart within the aggregate. The entire aggregate exhibits a twofold symmetry along its long axis. By comparing the size of the aggregate with the dimension of the chemical structure of Arg and taking the twofold symmetry of the aggregate into account they can be most likely assigned as Arg dimers.

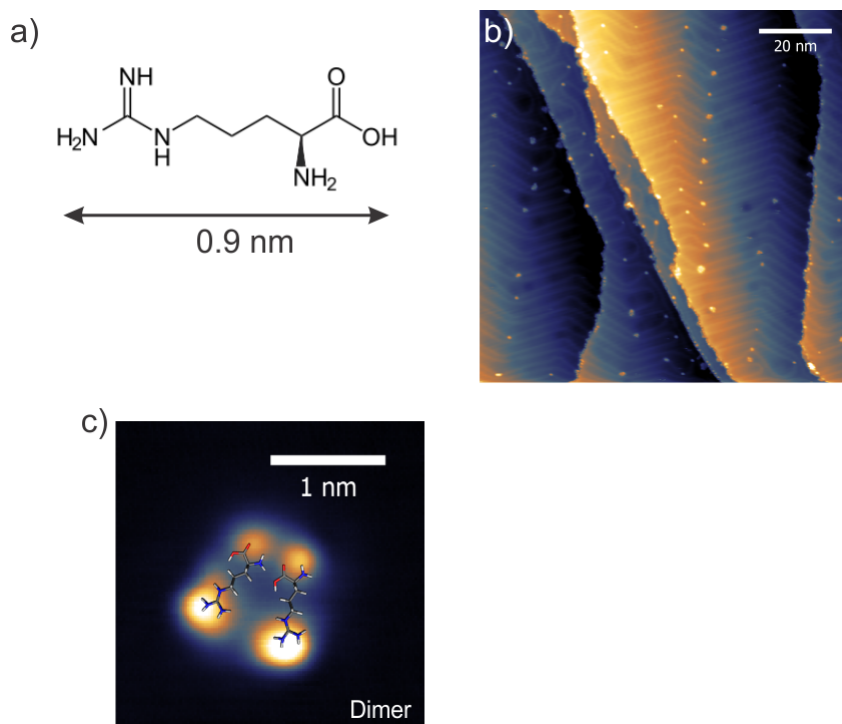


Figure 3.10 – a) Chemical structure and size of L-Arg. b) STM image of L-Arg evaporated on Au(111). Deposition parameters: 180°C,  $t = 30$  s. The Au(111) substrate was kept at room temperature. c) Characteristic Arg aggregate superimposed with structural formula of Arg.

Following this analysis each structure corresponding to a single Arg unit consists of two circular features in STM topography. These originate most likely from the amino acid group, inheriting elevated electron densities. It can be noted, that there is a difference in apparent height for the two observed features, which might be caused either by a variation in binding geometry or by local variations of the electron density. An exact allocation of one of the features to either the guanine- or the amino-group cannot be done based on the STM topography alone. However, there is data available in literature, which indicates that the adsorption of amino acids to a metal surface occurs via bond formation of the N (amino group) or the O atoms of the carboxyl group [143, 146, 155]. Currently, in a collaboration with C. Baldauf (Fritz Haber Institute, Berlin (Germany)), ab-initio simulations of Arg/Au(111) are prepared to rationalize the observed STM topography. For a deposition at room temperature mostly dimers or larger aggregates of Arg

### Chapter 3. The building blocks of peptides - Single amino acids on surfaces

are found on the sample surface. Predominantly they are immobilized at the most reactive elbow sites [149] of the Au(111) ( $22 \times \sqrt{3}$ ) reconstruction. In a similar fashion as for the case of Tryp, cooling of the Au substrate to 77 K during the deposition favors monomers and hinders the formations of dimers. These monomers (c.f. Fig.3.11 a)) can again be used to specifically functionalize the STM tip. The utilized protocol corresponds to the one described in the Tryp section.

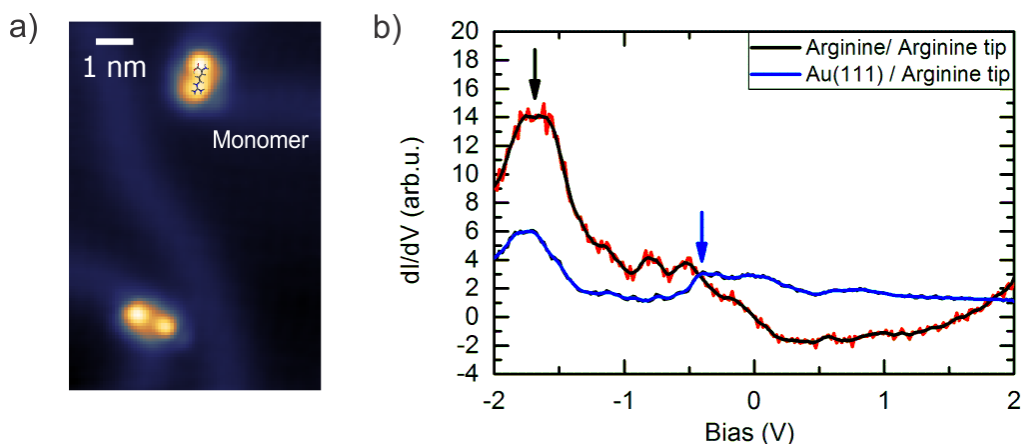


Figure 3.11 – a) Arg monomers on Au(111). b) STS measurement on Au(111) and Arg dimer with Arg functionalized tip revealing characteristic resonance of Arg (Acquisition parameters:  $I = 100$  pA,  $U_{mod} = 50$  mV,  $f_{mod} = 832$  Hz)

With a functionalized tip a characteristic resonance of Arg could be detected at a sample bias of  $U_B = -1.7$  V as indicated by the black arrow. Using a functionalized tip, this peak is also observable on the Au(111) substrate along with the surface state at  $U_B \approx -400$  mV. It has to be noted, that the observed resonances for Arg is at an almost identical position as the resonance observed for Tryp, which might either indicate that the observed resonance originates from a state of a common part of both amino acids adsorbed on the tip, such as the amino group. However, it was shown for L-Tryp on Cu(111) [143] that the orbital structure of the frontier orbitals of Tryp extends over the entire amino acid and thus it is unlikely that only a specific functional group corresponds to the conductance. In the present case of Arg, it is furthermore only possible to observe one state below  $E_F$ , which most-likely corresponds to Arg HOMO, opposed to the case of Tryp, where it was possible to observe HOMO and LUMO. The equal position thus seems either to be a coincidence or to be more-likely caused by an uncertainty in the measurement. Moreover a difference in interaction between the two amino acid species with the surface, might cause these peaks to be observed at almost identical energy positions. The overall energy position of the Arg resonance varied within a range of about 100 meV. The

width and the intensity of the peaks though varies rather strongly. This parameter might be strongly dependent on the adsorption geometry of the molecule on the tip, which leads to variations of the geometry of the tip apex. A more drastic energetic shift of the peak of the order of a couple of 100 meV and the occurrence of multiple peaks in STS is usually related to the adsorption of several molecules and could also be observed for Arg. A mapping of the spatial extension of the peak at -1.7 V could not be performed, since the molecules tend to be very unstable at these elevated values of  $U_B$ .

### 3.4 Proline

As a fourth amino acid L-proline was investigated on Au(111). Proline is one of the smallest amino acids and has a structural peculiarity. Its amine group is incorporated in the functional pyrrolidine group (c.f. chemical structure Fig.3.12b)). Interconnected in peptide chains, proline units do not bind in a linearly but interconnect in a helical binding motif as it was shown for poly-proline chains in [156]. Furthermore poly-proline helices are reported as very stiff assemblies due to a reduced rotational freedom of the proline-proline peptide bond [157][158] and thus acting as integral part in the structures of bio molecules [156][159][158]. STM studies on S- and L- Proline were performed on various surfaces such as Cu(110)[146], Ge(100) [160] and Au(111)[155]. In these studies relatively high coverages of the order  $0.5 - 1$  monolayer of L-proline was investigated. It was shown on Au(111) that proline appears as 0.5 nm wide circular feature and arranges in a regular closely packed hexagonal pattern [155]. In the experiments performed here, it was not possible to thermally evaporate proline using a molecular evaporator. Instead this obstacle was circumvented by utilizing ES-IBD as an alternative UHV method for the deposition of proline. An Au(111) sample was prepared according to the recipe described above. The sample was transferred under UHV conditions utilizing a vacuum suitcase (c.f. section 2.2.1) to an ES-IBD setup. The proline powder was dissolved in a mixture of  $H_2O$  and Ethanol (ratio 1:1) with 0.1 % of formic acid. Within the electrospray process of this solution, proline was brought as positive ions into UHV. After mass-selection proline was deposited onto the Au(111) sample, which was subsequently transferred back to the 4 K STM. It should be noted that up to now the set-up is currently limited to substrates kept at room temperature during ES-IBD. A new vacuum suitcase will be implemented, supporting cooling the samples to liquid nitrogen temperatures.

An overview scan of the resulting sample surface is depicted in Fig.3.12a) showing individual clusters of varying size. Furthermore, isolated objects have adsorbed at the elbow sites of the Au(111) surface reconstruction and appear as dot-like features (Fig.3.12c)). As a most common structure a tetramer assembly consisting of square arrangement of four circular objects, each having a size of about 0.4 nm, is observed. In size and appearance these correspond well to

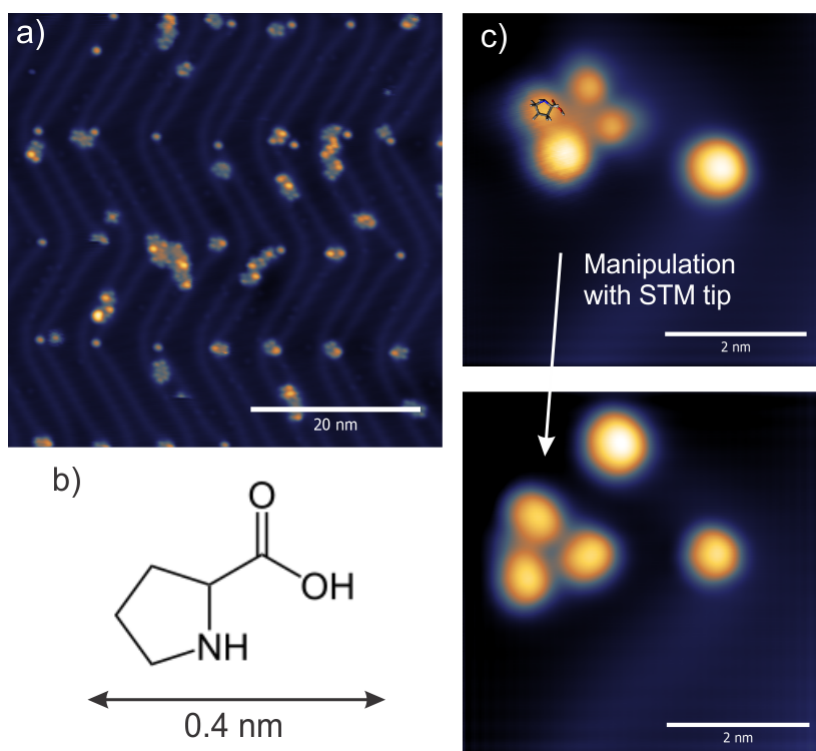


Figure 3.12 – a) STM image of L-Proline deposited on Au(111). The deposition was carried out with ES-IBD. b) Chemical structure and dimensions of Proline. c) Common structures of Proline on Au(111). Top image: Most common Proline tetramer superimposed with structural formula of Proline. Lower image: Tetramer after atomic manipulation with STM tip resulting in isolation of Proline monomer. (Acquisition parameters:  $U_B = -1$  V,  $I = 50$  pA)

the results obtained for S-proline on Au(111) in [155]. Most of the tetramers seem to adsorb on the objects immobilized at the elbow sites, which act as pinning centers. The tetramers are to some extent mobile on the surface and can be easily manipulated with the STM tip by approaching the tip or ramping  $U_B$  (Fig.3.12c) resulting in a displacement of the tetramers or eventually in splitting them.

However, a similar behavior is not observed for the individual adsorbates on the elbow sites, which are not prone to manipulation with the STM tip. Either this implies that they are a chemically different species and thus a contamination on the surface along with the proline or they are proline units which are adhered more strongly to the surface. For the Au(111) surface it is known, that the atoms on the elbow sites are the most reactive areas of this surface [149] making the immobilization of molecular adsorbates at these positions likely. A contamination of the Au(111) during the ES-IBD process is unlikely, as the ionic beam is mass-filtered prior to the deposition. As no clear identification of these features can be performed, they were ignored for the studies on proline or for subsequent tip functionalization purposes.

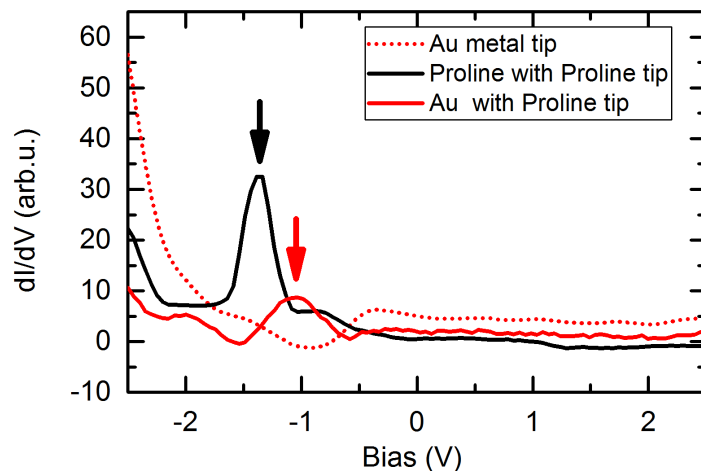


Figure 3.13 – STS measurements with proline functionalized STM tips on proline and on Au(111). The dotted red line is a reference measurement with a metallic tip on gold. The arrows indicate the relevant peaks (Black: Signature of proline with proline tip; Red: Signatures of proline functionalized tip on gold) Acquisition parameters:  $I = 50$  pA,  $f_{mod} = 832$  Hz,  $U_{mod} = 50$  mV.

In order to perform STS experiments with functional tips analog to the experiments performed on the other amino acids, the proline tetramers were split by means of a voltage pulse of about  $\Delta U_B \approx 2$  V. This is indicated in Fig.3.12c). Subsequently individual proline molecules could be attached to the STM tip according to the procedure described before. The results of the STS measurements are depicted in Fig.3.13. Again, it was possible to observe a characteristic feature in STS with a proline functionalized STM tip at  $U_B = -1.01$  V. On the metal surface, the functionalized tip revealed a state at  $U_B = -1.39$  V. As reference experiments with a purely metallic tip was used. Typical fluctuations of the observed states were in the range of a couple of 10 meV. Due to the relatively high mobility of the proline units on the Au(111) surface, the states could be observed but it was not possible to acquire spatial maps of the corresponding DOS.

### 3.5 Multiple amino acids on Au(111)

In a next experiment, the two amino acids Tryp and Arg were deposited on a Au(111) surface alongside pentacene. With this experiment we wanted to investigate, if an unambiguous identification of the various species is still possible on the surface. Pentacene was co-evaporated as a reference molecule to study the influence of a tip-functionalization with different molecular species on STS measurements on amino acids. A clean Au(111) substrate was prepared according to the recipe described before. During all depositions the substrate was kept at room



### Chapter 3. The building blocks of peptides - Single amino acids on surfaces

temperature. Fig.3.14 depicts a typical STM overview image of the resulting sample surface.

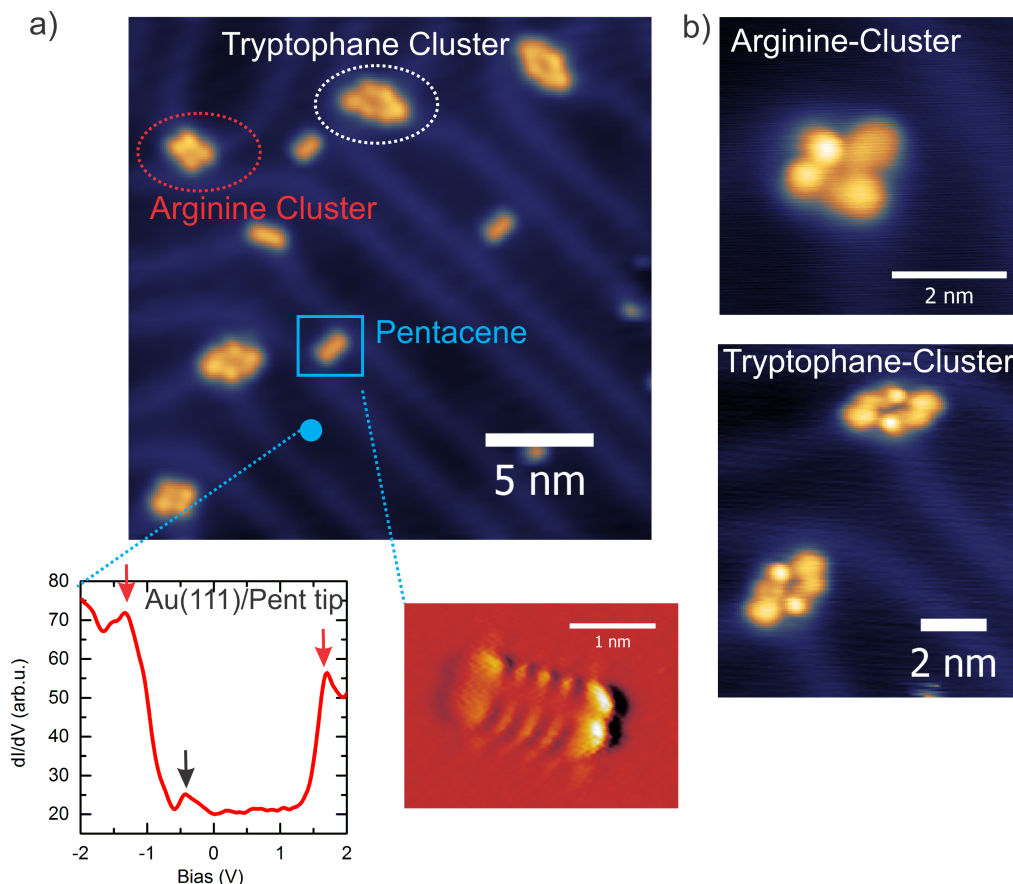


Figure 3.14 – a) STM image of Arg, Tryp and pentacene deposited on Au(111). The dotted circles indicate the positions of characteristic structures for each species. Acquisition parameters:  $U_B = -1$  V,  $I = 50$  pA. b) Detail scans of characteristic Arg and Tryp cluster imaged with a pentacene functionalized tip. The inset depicts an STS measurement on Au(111) with a pentacene functionalized tip ( $I = 50$  pA,  $f_{mod} = 832$  Hz,  $U_{mod} = 50$  mV) and the observed orbital shape of the pentacene HOMO.

One can see that it is possible to observe the characteristic structures for Tryp (Tetramers), Arg (Dimers) and Pentacene. Interestingly, these structures form in a similar way as for the samples with only one single species of amino acids. Tryp and Arg seem to not form any hybrid structures, implying that the dominating force behind the formation of the respective aggregates is the specific interaction between the amino acids of the same species. The very polar guanine residues of Arg are known to interact strongly with other polar sidegroups of peptides and thereby determine their specific conformation on a surface [37][13]. Arg has the tendency to passivate its polar groups via polar interaction with other Arg units on the surface. The elongated structure of Arg and its polar guanine-, carboxylate- and amino-groups offer multiple sites to form hydrogen bonds or interact via dipole-dipole interactions. Tryp as the



only other amino acid species on the surface on the other hand, has an unpolar aromatic character and is unlikely to engage in polar interaction with Arg. Furthermore, its specific curved conformation determined by the indole-group might also introduce a steric aspect hampering the aggregation of Arg and Tryp.

In literature [150] it is described for proteins, that Tryp is likely to interact in a perpendicular geometry with cations and other polar groups via its  $\pi$  electron system extending perpendicular to the plane of the aromatic ring of the indole group. By this an interaction between the  $\pi$  system and a neighboring cation, e.g. the charged residue of Arg in aqueous solution can be formed in a stacked geometry. However a stacked bonding motif would require that either the polar residues of Arg or the aromatic ring of Tryp are lifted off the surface. Due to the interaction of aromatic adsorbates with the dipole moment of the surface [161] a flat binding geometry seems to be more likely. By this the formation of specific clusters consisting only of Arg or Tryp might be favored.

Another aspect, which needs to be considered here, is the subsequent deposition of the amino acids. Thereby the respective aggregates of one amino acid might already form on the surface and thus making them unavailable for interaction with the second amino acid deposited in a subsequent step. However, it is not clear in how far these aggregates are already formed at room temperature during the deposition or if they condensate upon cooling to 5 K in the STM. In order to assess this aspect of the formation of amino acid aggregates, measurements at various temperatures would be necessary. To further study the role of functionalized tips in the specific recognition of amino acids in a STM experiment we performed similar experiments as described in the previous sections. Although it was possible to observe some of the characteristic peaks of the individual amino acids, the obtained results are unclear. A major problem poses the unambiguous determination of the state of the tip before attempting a functionalization or acquiring STS data. Therefore, the tip cleaning protocols and the recipes for a proper tip functionalization need to be more refined in control experiments. However, for pentacene as a molecular species the functionalization is well known and described in literature [35, 111, 162]. According to the experiments described in chapter 2, pentacene was brought to the surface and used for tip functionalization. A pentacene functionalized STM tip shows a clear signature in STS on the Au(111) substrate (c.f. inset Fig.3.14 a)). Furthermore, the orbital structure of pentacene is easily observable as exemplarily shown for the HOMO. For the Tryp and Arg, no significant features could be determined using a pentacene tip in STS or STM.

### **3.6 Conclusion**

With the experiments presented in this chapter, it was shown that various species of amino acids could be deposited on different substrates and investigated in STM and STS experiments. As a suitable substrate enabling both, STM and STS, Au(111) was utilized. For the amino acids of Phe, Arg, Tryp and proline specific binding motifs could be determined. Furthermore, employing amino acid functionalized STM tips it was possible to resolve electronic fingerprints of Tryp, Arg and proline. This enables further studies aiming at resolving these states in extended molecular compounds, such as peptides.

## 4 Towards sequencing of peptides on surfaces

In biology, a broad arsenal of "machines" with very intricate shape and functions at the nanoscale determines the processes in every cell. The utilized machinery is thereby based upon the self-assembly of peptides and proteins into complicated but still well defined three-dimensional conformations. Peptides consist of a chain of linearly interconnected amino acids. Due to the chemical diversity and specific interactions of the amino acid this chain folds and thereby defines the ultimate shape of the peptide. An aim of modern research and development of novel nanostructured materials is to understand and mimic the exquisite functionalities that could be observed in the toolbox of nature. DNA was one of the first biological compounds utilized for the generation of artificially engineered nanostructures [163] and nano-machines [164]. In contrast to DNA, which is designed for information storage and structural rigidity, peptides are chemically and conformationally versatile due to their sequential assembly. Furthermore, they often exhibit additional properties, such as catalytic activity. As a new approach, the imitation of the outstanding self-assembly capabilities of peptides and proteins is an interesting alternative to find ways for the generation of novel materials [22]. Thereby a general obstacle is the high structural complexity and thus the complicated potential landscapes [165] involved in the folding of peptides. This complicates the straightforward access and understanding of the specific relevant process involved in the formation of the distinct final conformation. In order to find simple model systems with reduced complexity and circumvent the often complicated isolation of natural peptides, an interesting alternative is the molecular class of synthetic peptide sequences. Synthetic peptides are generated for instance by solid-phase synthesis (SPPS) [39], which was developed by Merrifield in 1963 [166]. In the recent years SPPS [167] became an affordable tool to generate artificial peptide sequences with sufficient purity. This allows for the investigation of artificially designed model systems and their derivatives with properties inspired by nature. Thus the complexity of natural peptides and proteins can be reduced and specific properties can be singled out, allowing for the basic understanding of their function and structure. In the last decades, there are a

number of examples in literature studying (synthetic) peptide self-assembly into nanostructures [168]. In [169] the formation of self-assembled amyloid nanostructures introduced by cross  $\beta$ -sheet formation was studied. Matson et al. [170] discussed different classes of peptide amphiphiles, Fmoc-peptides, self-complementary ionic peptides and hairpin peptides, which can be utilized for the generation of self-assembled nanostructures suitable for the generation of scaffolds for bio-active materials. Further experiments using synthetic peptide sequences were performed by Ghadiri et al. [171]. They studied the formation of cyclic peptide nanotubes with an alternating sequence of L and D amino acids. However, in contrast to natural peptides, the self-assembly of engineered peptide sequences still follows rather simple design principles, such as the use of alternating domains of polar- and unpolar amino acids leading to a segregation of the two upon folding and the formation fibril-structures [14]. The application of more intricate design principles requires a fundamental knowledge of the peptide structure as well as a detailed knowledge of the interactions between the individual amino acids involved in the self-assembly process. In a first theoretical study by Frederix et al. [172] the influence on the chemical space of tri-peptides by specific amino acids was investigated and general design rules for the self-assembly of small peptides could be established.

On the experimental site it is therefore an interesting approach to investigate peptides and their self-assembled structures on a single molecular level with the two key tasks of direct structure determination and identification of the individual amino acids on a nanometer scale. With respect to possible technological applications of peptide nanostructures, such as functional coatings [173] or bio molecule interfaces [174, 175] with other materials another important aspect is their specific assembly and binding to inorganic surfaces. Within the last decade, STM became an important tool to probe peptide nanostructures with nanoscale precision for their structural characteristics on surfaces. Claridge et al. [176] employed STM measurements on a synthetic peptide sequence comprised of Histidine- and Alanine drop-casted on a HOPG-surface to investigate its specific assembly. Experiments performed by So et al. [177] studied the binding of genetically engineered peptides to a Au(111) surface and could deduce principles behind the formation of the peptide/metal interface. Lingenfelder et al. [11] was able to trace the chiral recognition of Phe-Phe by thermally evaporating the small di-peptides onto a Cu(110) surface.

When performing STM experiments on large bio-polymers such as peptides a general difficulty is the discrimination between the individual amino acids due to the lack of chemical sensitivity of the STM. Typically it is not directly possible to perform such an identification based on STM data, without the extensive application of MD- or DFT- based models. In the following chapter a possible approach towards problems of the structural determination and the on surface identification of amino acids in peptide sequences is presented. As sample systems,

---

two simple synthetic peptides, consisting of two and three amino acid species respectively are utilized. On behalf of the results presented here, the influence of a modification of the peptide sequence on the on-surface self-assembly could be studied. As it will be shown, macromolecules as the utilized synthetic peptides possess a high conformational freedom, which makes the structural determination of even rather simple peptides absolutely non-trivial. As a main focus the application of functional STM tips, modified with amino acids adsorbed at their apex is discussed. It could be shown, that by employing these tips, a specific recognition and thereby a partial sequencing of the peptide sequences on the surface was enabled. By comparison with DFT models, the results could be rationalized.

### 4.1 Model system - WWPPPPWW on Au(111)

The first model system discussed here is a peptide with the sequence  $NH_2 - WW - PPPP - WW - COOH$  and is referred to as WWPPPPWW. The chemical structure of WWPPPPWW is depicted in Fig.4.1. The design of the first investigated peptide was chosen as such, that it enables the observation of individual amino acids. Therefore a sequence of two sets of amino acids with big functional groups (Tryp (W)) separated by a short and stiff spacer (proline (P)) was chosen. A poly-proline chain consisting of four L-prolines was chosen as spacer because of their helical bonding motif. Proline-proline bonds are considered to be one of the stiffest peptide bonds [156, 159] and thus are a suitable structural element to enhance the rigidity of the peptide chain. Tryp was utilized because of its conjugated indole residue providing high electron density observable in STM [143]. Furthermore aromatic amino acids have the tendency to adsorb in a planar binding geometry as it was shown on the example of Phe on metal surfaces [145]. The synthetic peptides used in this work were obtained from the commercial supplier "GeneScript" ([www.genscript.com](http://www.genscript.com)) and delivered in lyophilized form with a purity of 99%.

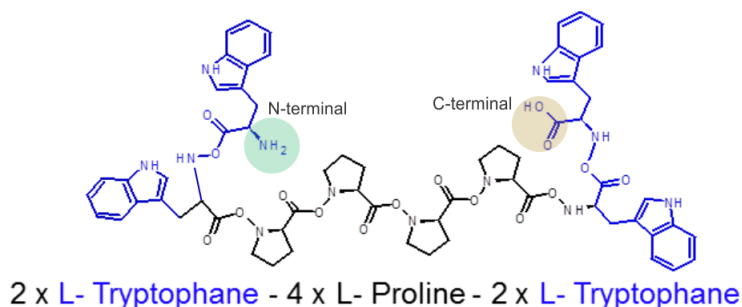


Figure 4.1 – Chemical structure of the synthetic peptide with the sequence WWPPPPWW. The N- and the C-terminal are color coded.

WWPPPPWW has a molar mass of 1390 g/mol. Typically molecules of this weight cannot be thermally sublimated using a molecular evaporator. In order to bring WWPPPPWW to a surface in UHV, an ES-IBD on a Au(111) surface was performed. To this end WWPPPPWW was dissolved in dimethyl sulfoxide (DMSO). In the mass selection process the singly protonated state was isolated and used for deposition. STM scans of the sample are depicted in Fig. 4.2. One can see that the deposited molecules form mainly 2D islands with varying sizes and a substructure consisting of regularly arranged dot like features. The coverage of the Au(111) surface can be estimated to  $\approx 20\%$ . Typical island sizes range from a couple of  $10 \text{ nm}^2$  to up to a  $1000 \text{ nm}^2$ . It is possible to see, that the borders of the islands follow the three high symmetry directions of the Au(111) surface. A small periodic modulation of the apparent height is visible

leading to a "striping" of the islands (c.f. red dotted lines in Fig.4.2a)). These features originate by the  $22\times\sqrt{3}$  (herringbone) reconstruction of the underlying gold substrate. Acquiring high resolution STM images gives more insight in the individual building blocks of the networks (Fig.4.2b)). One can recognize that the individual building blocks appear in a "windmill like" shape as it is indicated by the cartoon representation and are thus referred to as windmills in the following. They consist of four prominent lobes with high apparent height in a squared arrangement. Four lobes with lower height extend out of these and thereby form the windmill shape. This structure has a four-fold symmetry and is chiral. The main lobes are spaced about 1.2 nm apart as it is indicated by the depicted profile.

Additionally the islands are divided into parallelly arranged domains of about 4 nm width (c.f. white dotted lines Fig.4.2 a)) separated by domain borders, which appear as dark lines in the STM contrast. A precise origin of these domains cannot be determined. The equally spaced domains with two binding geometries might hint at a strain relief mechanism, for example due to the mismatch of the preferred adsorption sites of the molecules on the Au(111) substrate [178]. Furthermore in one domain the windmills are arranged such that adjacent lines are shifted by half the size of a windmill with respect to each other. Thereby the windmills are arranged in a diagonal geometry. In the neighboring domains they are arranged in a linear geometry (c.f. Fig.4.2c)). Interestingly for domains with diagonal arrangement it is not possible to arrange the windmills by pure translation. Only every other line matches with this windmill, which indicates the presence of two types of windmills in this domain. The linearly arranged domains on the other-hand consist of only one type of windmill. An explanation for this observation might be given by accounting for the chirality of the windmills. In the diagonal domains with alternating lines varying chirality of the windmill form the networks, whereas the linear domains only consist of homo-chiral windmills. Similar effects were also reported in literature for instance for self assembled two-dimensional networks of adenine on HOPG [179, 180].

On the edges of the networks, evenly spaced (about 1.6 nm) features with a doubled apparent height and bean like shape are visible (right STM image Fig.4.2c)). At each position of such a feature the neighboring windmill is missing one of its prominent lobes. This indicates that the elevated features are part of the windmill which are lifted off the surface due to a lack of interaction with a neighboring windmill. This also hints at the fact, that the windmills are indeed the smallest building blocks of these networks and presumably correspond to one WWPPPPWW peptide. By comparison of the structure observed in the network to the chemical structure of WWPPPPWW one can see that they do not match in a straight forward manner. From the chemical structure one can estimate the size of an outstretched WWPPP-PWW molecule to be about 3.1 nm, roughly twice the size of the observed building blocks.

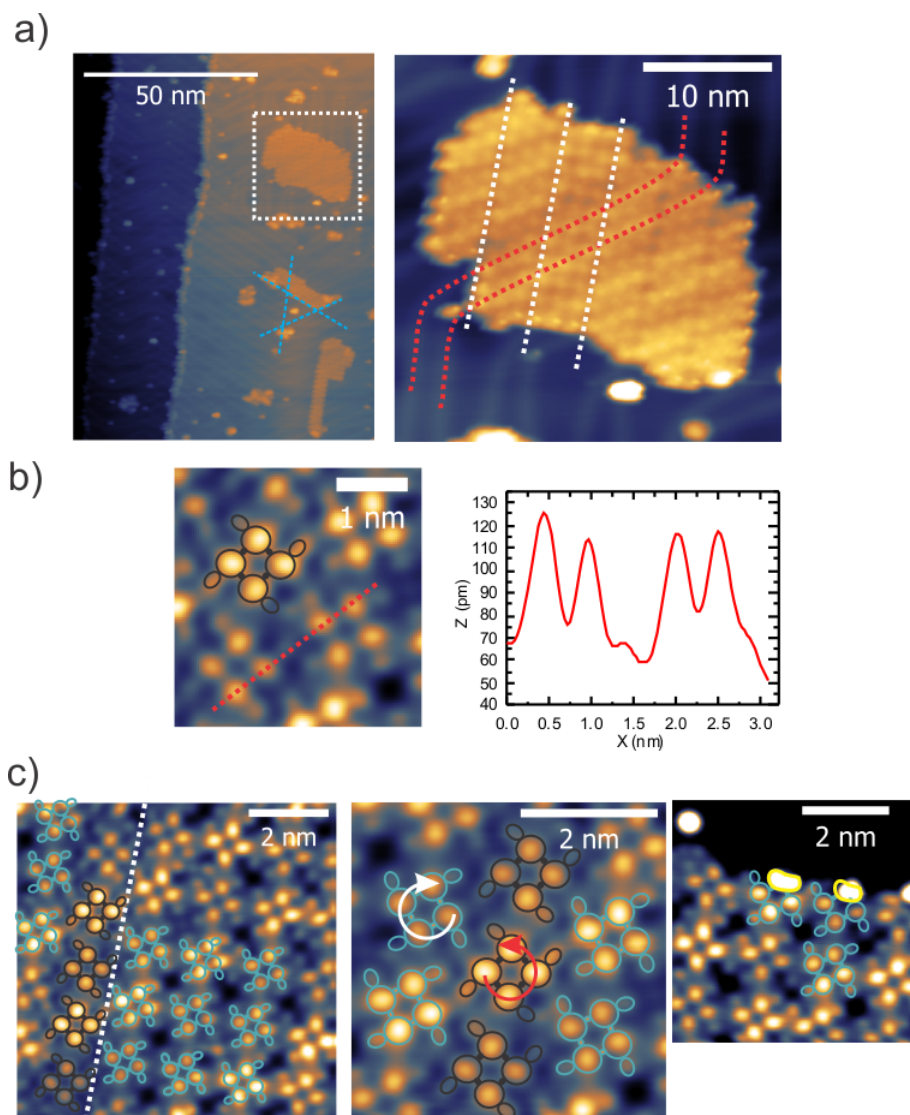


Figure 4.2 – a) 2D-network of WWPPPPWW on Au(111) (dotted square). The right STM topography image depicts a zoom-in on the marked frame. The red dotted lines indicate the course of the Herringbone reconstruction. The white parallel dotted lines indicate the borders of the respective domains within the 2D-network (Acquisition parameters:  $U_B = -1$  V,  $I = 50$  pA (constant current)) b) High resolution STM image (Parameters:  $U_B = 1$  mV,  $I = 50$  pA (constant height)) of the network superimposed with cartoon representation of a building block. The red line indicates the position of the height profile shown in the right graph. c) High resolution constant-height STM image superimposed with cartoon of building blocks to visualize the assembly. The white dotted line indicates a domain border. The circular arrows describe the chirality of the folded peptides.

Furthermore, the observed symmetry and periodicity of the network cannot be reproduced using an outstretched single molecule. A local gradient relaxation in the gas-phase was per-



formed by J. Cortes et al. (LAAS-CNRS, Toulouse, France) to obtain a first estimate of the structure. The resulting structure is depicted in Fig.4.3 a) and b). The energy minimum of the peptide conformation in the gas-phase corresponds to a folded structure with Tryp groups in one plane and a curved poly-proline chain arranged below (Fig.4.3a)). The size of this folded conformation obtained for the gas-phase, fits well to the dimensions of the "windmill" units of the networks. Assuming that these units correspond to a single peptide, implies that WWPPPPWW exhibits a folded conformation on the surface as well. The peptide backbone is folding in such a way, that the polar groups of the N- and the C- terminal but also the NH- and doubly bond oxygen groups of the backbone can engage in polar interaction and can form hydrogen bonds. The non-polar functional residues of Tryp and proline are facing outwards towards the non-polar medium of the vacuum, whereas the polar residues are passivated due to their mutual interaction. This is a common motif of peptides in non-polar environments and is described in literature [13, 37, 181].

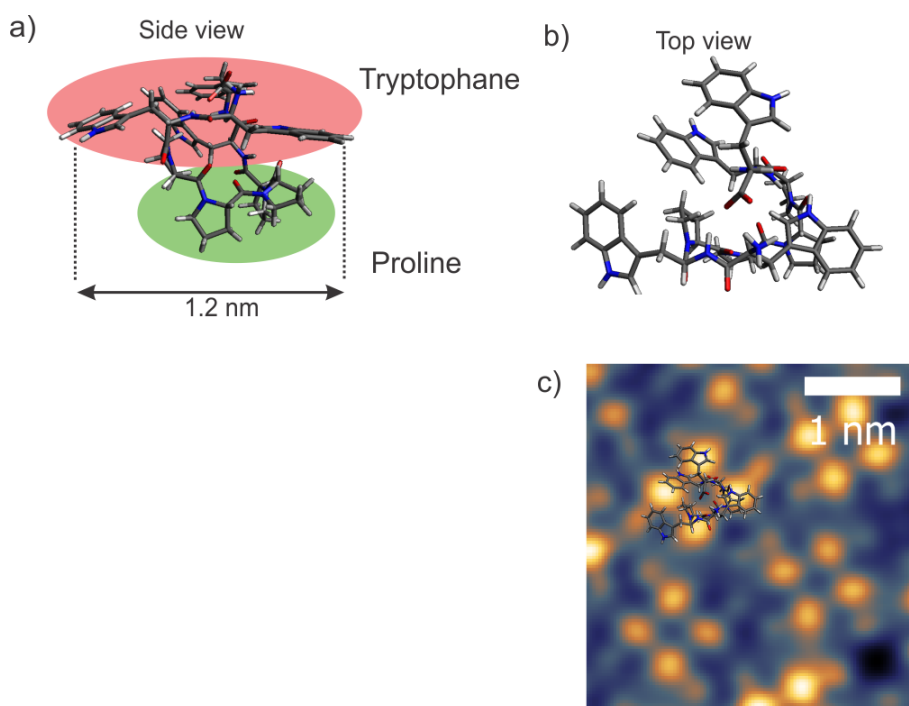


Figure 4.3 – a),b) Side and top view of the structure of WWPPPPWW generated by a gas phase relaxation. c) WWPPPPWW networks on Au(111) superimposed with the simulated structure.

With this model, the four equivalent most prominent lobes of the windmill building block of the structure can most likely be explained by the two terminal sets of Tryp groups arranging in a square geometry. One of the two ring-systems of the indole group might correspond to the arm like structures extending from the four main lobes of the windmill (c.f. Fig.4.3 c) STM

image). However, it should be noted that this is just a tentative model based on experimental observations in tandem with a gas-phase model. The symmetry of the windmill-shape is not reproduced by the gas-phase model, most-likely since no interaction with an underlying metal-substrate and no interaction with neighboring peptides was taken into account. The interactions with the neighboring peptides in the network, such as hydrogen bonding or polar interactions, might lead to a reorientation of the individual residues and thus yielding the shape and symmetry as it is observed in the experiment. In order to rationalize the structure further, a simulation of the molecule including the surface and neighboring WWPPPPWW units needs to be performed. This is a rather cost-intensive calculation and could not be included in this work.

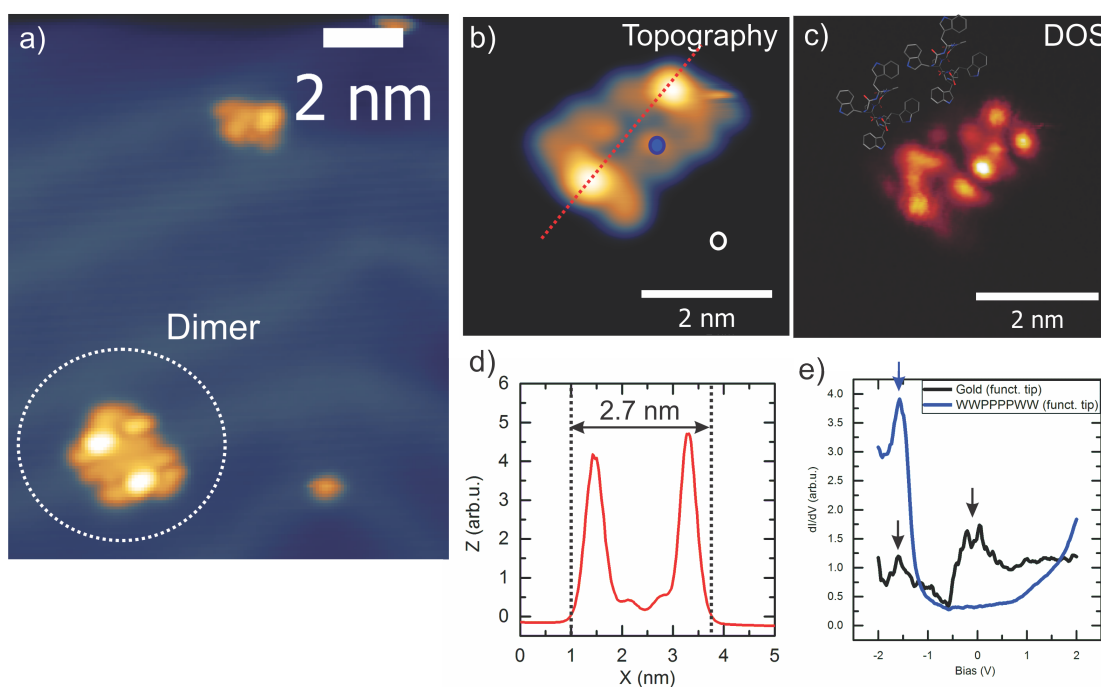


Figure 4.4 – a) STM topography image of a WWPPPPWW dimer on a Au(111) surface. b) Constant height STM image of WWPPPPWW dimer. The two circles correspond to the coordinates of the STS measurements depicted in e). The red dotted line indicates the position of the height profile shown in d) (Acquisition parameters:  $I=50$  pA,  $U_B=-1.7$  V). c) Spatial distribution of the DOS at -1.7 V acquired simultaneously to the current map shown in b) using a lock-in technique (Parameters:  $U_{mod}=50$  mV,  $f_{mod}=832$  Hz) with a peptide-modified STM tip.

Interestingly it was also possible to observe smaller repeating structures on the surface which could be attributed to WWPPPPWW dimers by their size of about two times the building blocks (c.f. Fig.4.4 a), b)). They have a length of about 2.7 nm and two characteristic lobes with elevated intensity (c.f. Fig.4.4 d)). In STS measurements it was possible to identify a molecular resonance at  $U_B \approx -1.7$  V (Fig.4.4e)). The reference measurement on gold indicated that the

utilized tip was functionalized, most likely with another WWPPPPWW molecule due to the occurrence of additional resonances apart from the surface state (c.f. black curve Fig.4.4e). With this tip, it was possible to map out the spatial distribution of the LDOS at this energy (Fig.4.4c)). It is possible to notice a clear difference of the obtained LDOS to the STM topography. A clear assignment of the specific origin of this peak cannot be made at this time. Further measurements utilizing functional STM tips with specific probe molecules combined with simulations of the molecular structure on the surface and the resulting electronic structure are necessary to gain a more complete understanding of the observed structure.

From the results presented here on the first studies of a synthetic peptide an initial determination of the structure on the surface could be performed and deduced that the sequence is undergoing a specific and reproducible folding process. The folded peptide units exhibit the capability to form highly ordered networks in a self assembly process.

## 4.2 Modifying the sequence - WWPPPPRR on Au(111)

We modified the sequence described in the previous section in order to find a peptide sequence suitable as a model system for sequencing. Such a model peptide should preferentially provide an outstretched and flat adsorption geometry on the surface allowing to resolve all contained amino acids in the sequence. Furthermore, it should be possible to discriminate between N- and C-terminal to aid the identification of the individual groups. Therefore, one set of the terminal Tryp groups was replaced by two Arg groups resulting in a new peptide with the sequence  $NH_2 - WW - PPPP - RR - COOH$ , which is in the following referred to as WWPPPPRR. The chemical structure of WWPPPPRR is depicted in Fig.4.5 a).

The guanidine residue of Arg might enable hydrogen bonding to the C-terminal, which might lead to an outstretched conformation. This hypothesis is supported by local gradient relaxation of the sequence in the gas-phase (J. Cortes et al. (LAAS-CNRS, Toulouse, France)). The structure corresponding to the lowest energy minimum is depicted in Fig.4.5 b). One can see that the peptide indeed favors an outstretched conformation in the gas-phase. Estimated from its chemical structure a length of the structure of about 3.1 nm can be approximated. For all following experiments a Au(111) substrate was utilized and prepared in UHV, following a similar recipe as described in the previous chapter. Because of the relatively high mass of 1093 g/mol, WWPPPPRR was brought on the surface in UHV via ES-IBD. Therefore, the lyophilized peptide was dissolved in a solvent mixture of ethanol and  $H_2O$  with a ratio of 1 to 1. In the subsequent mass-selection in the ES-IBD process, the two fold positively ionized peak was isolated and used for the deposition.

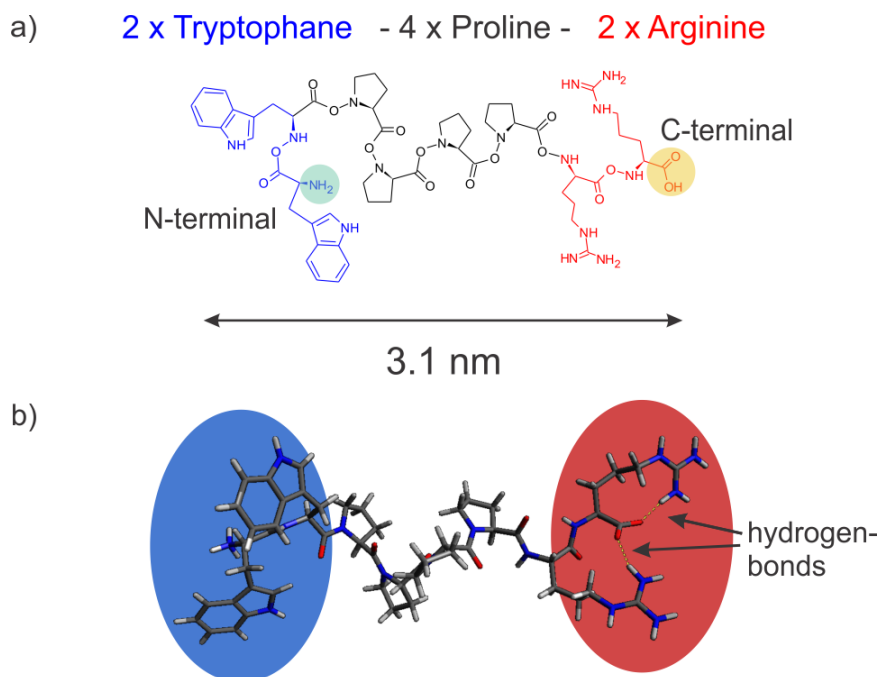


Figure 4.5 – a) Chemical structure of the synthetic peptide WWPPPPRR and its amino acid sequence. Its head to tail length was determined to  $\approx 3.1$  nm. b) Resulting conformation from a gas phase local gradient relaxation of the peptide sequence. The Tryp groups are highlighted in blue, Arg in red. The yellow dotted lines correspond to H-bridges.

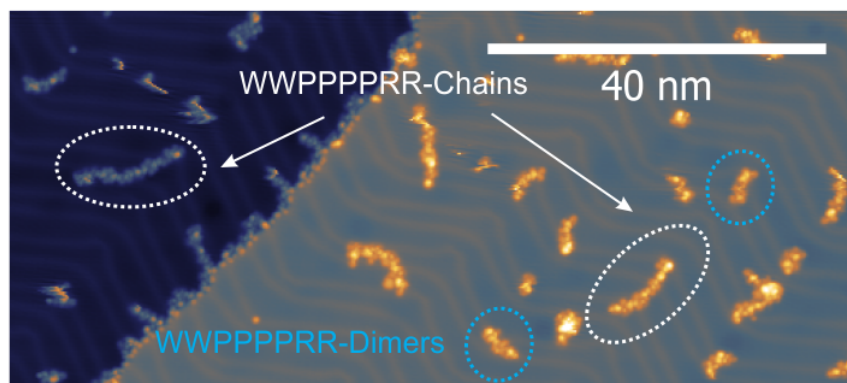


Figure 4.6 – a) STM overview topograph depicting linear chains (dotted white circles) and dimers (dotted blue circles) of WWPPPPRR on a Au(111) surface.

An overview STM topograph of the resulting sample is depicted in Fig.4.16a). From these scans it can be directly seen that WWPPPPRR has completely different self-assembly properties than WWPPPPWW. Instead of forming extended two-dimensional networks the peptide now self-assembles to linear chains of various lengths. Two main structures can be observed, namely extended chains and short structures with a length of about 6 nm and a two fold symmetry.

Comparing these structures to the length of gas-phase relaxations of the molecular structures reveals that they have about two times the size of a monomer. Thus, the smaller species might be dimers (blue dotted circles Fig.4.16a)). Their specific structure will be discussed in the following in detail.

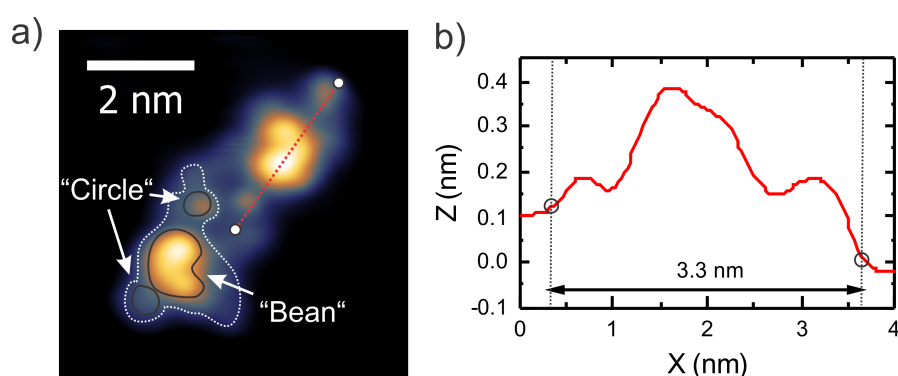


Figure 4.7 – a) STM topography image of WWPPPPRR dimer. The red dotted line indicates the position of the height profile depicted in b). The white dotted line marks the outline of a monomer. Two characteristic features are indicated by the arrows.

A high resolution STM image of a typical dimer structure can be seen in Fig. 4.7a). According to this image one can identify the twofold symmetry of the dimer very well. The dimer consists of two identical building blocks (c.f. white dotted line Fig.4.7a)), with one of them rotated by 180°. Furthermore one can see that each of the building blocks has an apparent length of about 3.3 nm (c.f. height/length profile Fig.4.7b)). For each building block one can identify 3 main features. The central part consists of a "bean" shaped structure with the highest apparent height. This structure is surrounded by two circular structures at each end of the dimer.

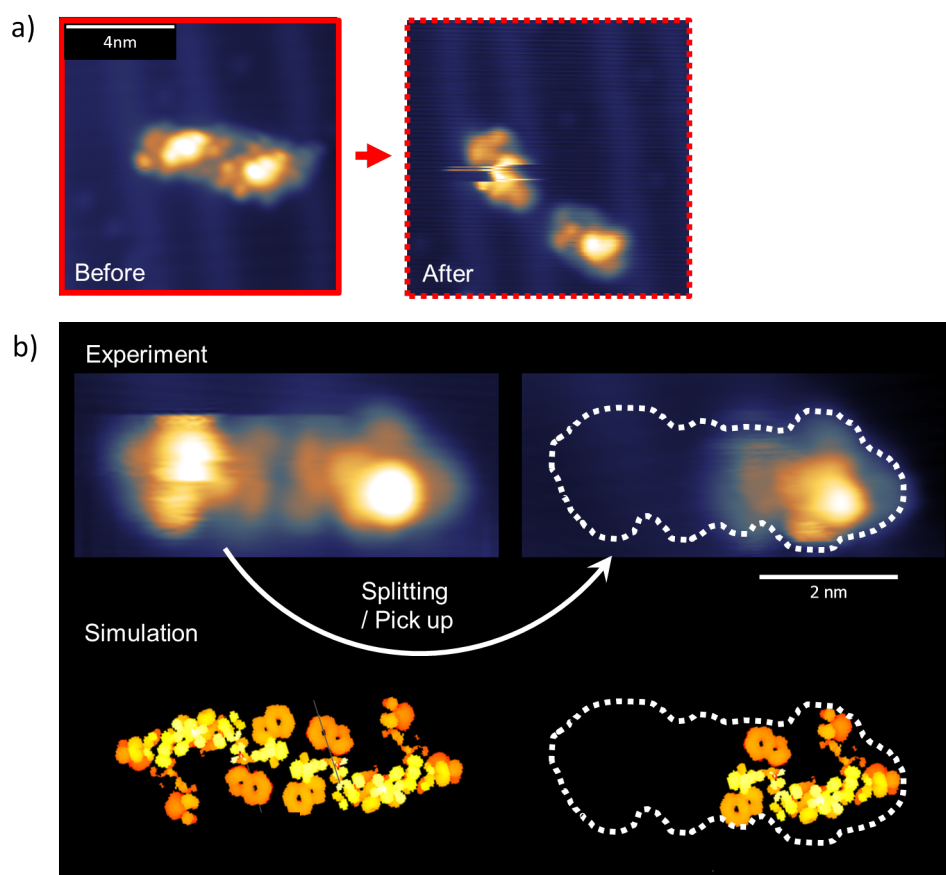


Figure 4.8 – a) Splitting of WWPPPPRR dimer induced by increasing  $U_B$  from -1 V to -2.5 V ( $I=50$  pA). The two separated Monomers remain next to each other b) Splitting and removal of one WWPPPPRR monomer out of the dimer assembly by similar voltage pulse as in a).

A strong bond between the building blocks of the dimers can be excluded, since it was possible to split them in the experiment by relatively mild voltage pulses of about -1.5 V to -2 V while the tip was positioned in the dimer center. This is depicted for two cases in Fig.4.8a) and b). Furthermore the experiments depicted in Fig.4.8 show that the dimers indeed consist of two identical building blocks. With this, a general rationalization of the observed structures is possible, proofing that they are dimers.

For the observed structure, a local gradient based ab initio relaxations (DFT, VASP algorithm) of a WWPPPPRR monomer on two atomic layers of gold were performed <sup>1</sup>. The simulated structure is depicted in Fig.4.9. From the side view image of the relaxed structure (Fig.4.9a)) one can see that the functional residue of Tryp has the tendency to bind in a flat geometry to the gold surface. The two groups of arginine adsorb in slightly varied adsorption geometries,

<sup>1</sup>Collaboration with C. Schön et al. (Rheinische Friedrich-Wilhelms-University Bonn (Dept. Chemistry), Max-Planck Institute for Solid State Research, Stuttgart)

## 4.2. Modifying the sequence - WWPPPPRR on Au(111)

one in a planar geometry, the other one slightly rotated. The most elevated parts of the peptide are the N-terminal and two of the proline units. The geometry of the proline units inside the peptide chain can be related to the helical bonding motif of the proline-proline bonds, forcing two prolines away from the substrate and into this geometry. The helical conformation of the poly-proline segment of the peptide is counteracted by the tendency of the indole residue of Tryp to bind in a flat geometry to the gold surface. For the aromatic system of Tryp, the interaction with the dipole moment of the surface favors [182] a flat adsorption geometry as it is described for numerous aromatic molecular species on metal substrates in literature [98, 99, 145, 183, 184].

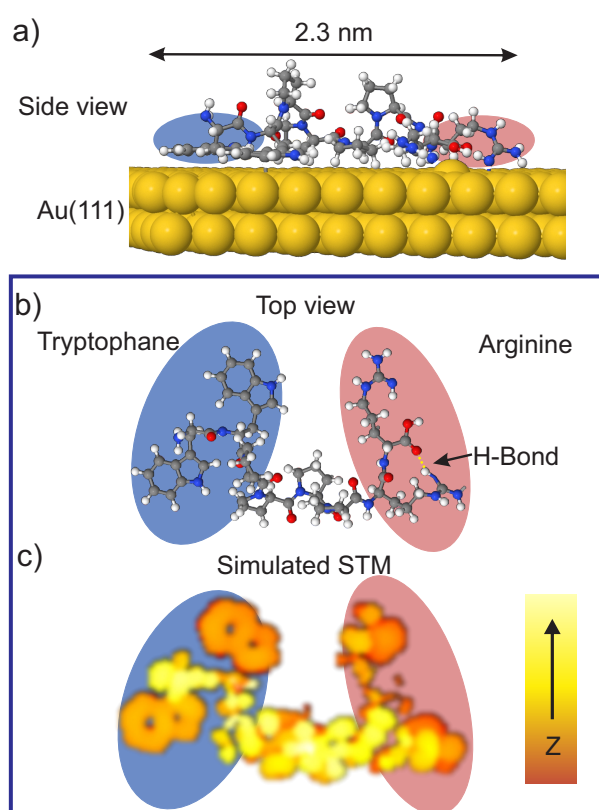


Figure 4.9 – a) Side view of structure of WWPPPPRR monomer relaxed on (DFT, VASP algorithm) two atomic layers of gold. The end to end length of the structure is indicated in the figure. Tryp and Arg are color-coded. b) Top view of relaxation result (for visibility reasons the surface is not depicted). c) Simulated STM image for the occupied orbitals within 2 eV below the Fermi level based on the structure from b). Orange colors correspond to low apparent height, bright yellow colors to high apparent height.

The top view (Fig.4.9b)) shows that the peptide has a curved conformation on the surface. There are a number of different contributions leading to this conformation. On the Arg side of the peptide the flat lying guanine group seems to exhibit a relatively strong interaction with

the gold surface, indicated by the relatively close distance to the surface. However it should be noted, that the displaced gold atom is most likely an artifact from the calculation and does not correspond to an actual physical effect. A strong affinity of Arg to bind to a Au(111) surface however was also reported in literature [182]. A major contribution to the overall conformation of the molecule and the non-equal bonding scheme of the two Arg groups might furthermore originate from the hydrogen-bonding of the rotated guanine group to the C-terminal of the peptide as it is indicated in Fig.4.9 b). This stabilizes this conformation. It should be taken into account that a global search for energetic minima in the potential landscape for WWPPPPRR indicated several minima which are in close energetic proximity to the one corresponding to this structure. This shows the high conformational freedom of macro molecular structures such as the one of WWPPPPRR.

For the relaxed structure it was possible to calculate a simulated STM image based on a gas-phase DFT calculation performed with a home-made code by R. Gutzler<sup>2</sup>. A gas-phase method was chosen, since it was assumed that the Au(111) substrate is interacting rather weakly with the electronic structure of the ad molecule and thus can be neglected for this calculation. This is in good agreement with the results reported for Angiotensin-II on Au(111) by Abb et al. [13]. All contributions to the electron density from orbitals within an energy window from  $E_F$  to 2 eV below  $E_F$  were taken into account. This corresponds to the typically applied values of  $U_B$  for this experiment. The result of this simulation is depicted in Fig.4.9c). One can see that the most prominent features in the simulated STM image have their origin in the upright standing proline groups and the N-terminal of the peptide. The functional residues of Arg and Trp exhibit some contrast but appear considerably lower due to their flat binding geometry.

---

<sup>2</sup>Simulation performed by R.Gutzler (Max-Planck Institute for Solid State Research, Stuttgart (Germany))



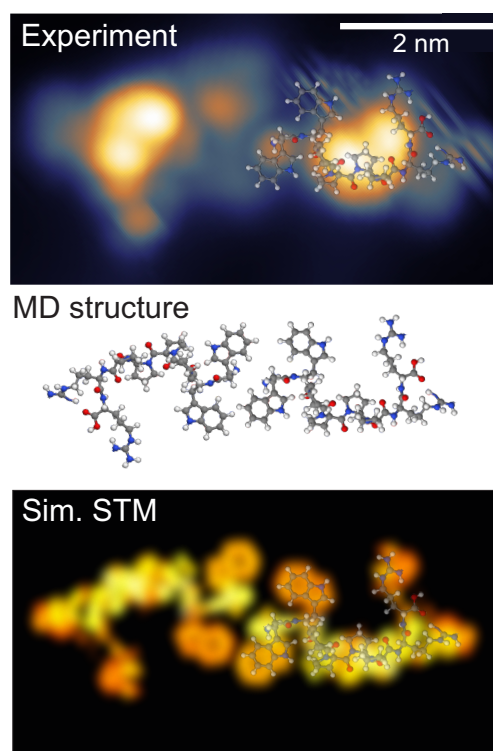


Figure 4.10 – Comparison of experimental STM topography image (top) of WWPPPPRRR dimer to relaxed (simulated) structure (middle) and simulated STM image (bottom).

In Fig. 4.10 a direct comparison between a STM image of a WWPPPPRRR dimer and the suggested arrangement based on the simulated model is shown. One can see that the relaxed structure fits to the experimental data. It should be kept in mind that the dimer structure is assembled based on the relaxed structures for the WWPPPPRRR monomer (similarly for the simulated STM image). Thus, the specific orientation, especially of the individual amino acid residues cannot be determined precisely. For the experimentally observed structure, the length of a monomer could be determined to 3.3 nm. In contrast to this, the theoretical structure has only a length of 2.3 nm from end to end. Nevertheless, this is in good agreement, since in a STM experiment the extended electron density is measured to the effect that an object appears bigger than its pure chemical structure is. Minor deviations of the experimental data from the simulated structure furthermore originate from the high conformational freedom of the peptide sequence on the surface. The agreement between theory and experiment is visualized best by comparing the simulated STM image with the experimental one (bottom image Fig. 4.10). By this it becomes apparent, that the "bean" shaped elevated regions correspond to the upstanding proline units in the center of the peptide sequence. The circular features in the center of the dimer

are related to the  $NH_2$  group at the N-terminal together with one of the Trp residues. The two arm like features extending from the "bean" shaped area correspond to the functional residues of the Arg. In this conformation the dimer structure is stabilized most likely by a polar interaction between the two  $NH_2$  groups of the N-terminals and the aromatic  $\pi$  system of the indole. These interactions between polar groups or cations and the aromatic system of Trp are also reported to provide a significant contribution to the structural stabilization of natural proteins [185–187]. Although the most favorable interaction geometry was reported to be a perpendicular arrangement, parallel interaction schemes are observed as well. Taking into account the interaction of Trp with the surface this might be plausible. Overall this could result in the slightly staggered arrangement of the two N-terminals (circular features at the dimer center in the STM topography) as it is observed in the experiment. By introducing Arg as polar amino acid on the C-terminal of the sequence, an outstretched conformation of the peptide units on the Au(111) could be observed in dimers and linear chains. Combining high-resolution STM imaging with simulations of the molecular structure, the individual features visible in STM topography could be related to the respective amino acids of the sequence.

### Partial sequencing of WWPPPPRR using an Arg functionalized STM tip

An aspect, which is still missing is an experimental proof for the individual orientation of the monomers inside the dimer assembly. Therefore a methodology is required, that enables to be sensitive towards specific groups within an STM experiment. It was shown in the previous chapter on amino acids, functional STM can indeed yield access towards specific electronic features in STS experiments. In a similar fashion it was tried to gain sensitivity towards amino acids within the peptide chain by applying functional STM tips decorated with specific amino acids. As an initial step a sample of WWPPPPRR on Au(111) was prepared as described before. In an additional step, Arg was co-deposited in a thermal evaporation process, while the sample was cooled to  $LN_2$  temperature (77K). This preparation resulted in a sample with the previously described WWPPPPRR chains and dimers, as well as Arg monomers. In a first set of experiments STS measurements with a metallic tip were performed on the WWPPPPRR dimer (Fig.4.11 a)).

As a reference, a STS measurements on Au(111) was performed with the same metallic tip. Here, only the surface state at  $U_B = -400$  mV is observable. On the WWPPPPRR dimer at the position indicated by the red dot in Fig. 4.11a) a molecular resonance can be observed at  $U_B = -1.77$  V. In a next step a neighboring Arg (dotted circle Fig.4.11a)) was picked up according to the methodology described in the previous chapter. Fig.4.11b) shows the same area after the functionalization of the tip with the Arg. One can see that the adsorbed Arg is gone from the surface. Furthermore, a change in the internal contrast on the dimer can be observed, which

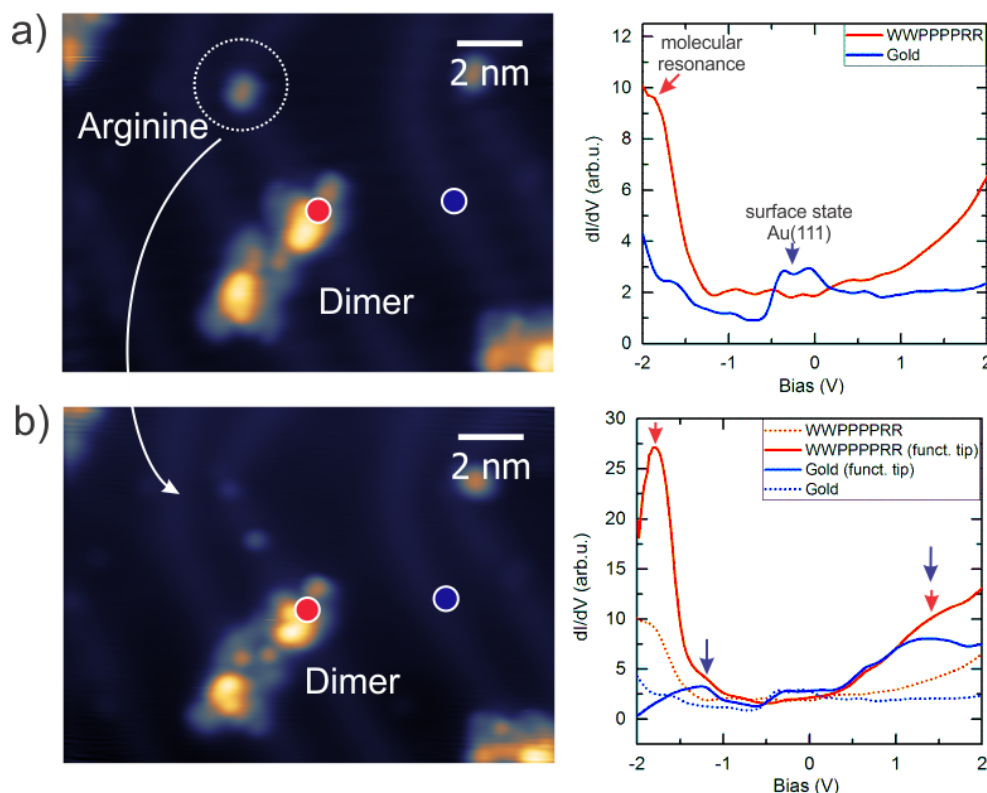


Figure 4.11 – a) Left: STM topography image of a WWPPPPRR dimer and neighbouring arginine. Right: STS measurements with a metallic STM tip on the indicated positions on gold (blue graph, blue dot) and WWPPPPRR dimer (red graph, red dot). b) Left: STM image of the same area as shown in a) after picking up arginine with the STM tip (dotted white circle). Right: STS measurements graph with a functionalized tip (solid lines). The arrows indicate the positions of new resonances observed on gold and the WWPPPPRR dimer. The dotted lines depict the STS measurements shown in a) for comparison. (Acquisition parameters: STM images:  $I = 50$  pA,  $U_B = -1$  V (constant current); STS:  $I = 50$  pA,  $U_{mod} = 50$  mV,  $f_{mod} = 832$  Hz)

can be accounted to an altered geometry of the tip apex. Performing an STS measurement on the Au(111) reveals, apart from the Au(111) surface state, two additional peaks visible at  $U_B = -1.28$  V and  $U_B = +1.39$  V, indicating a successful tip functionalization. In the following the STS measurement on the WWPPPPRR dimer (similar position as before) with this functionalized is repeated. With identical measurement parameters the previously observed feature is now measured as a peak with an intensity increased by a factor of 3 compared to the measurement with a metallic tip. The energetic position of the molecular resonance has not changed within the accuracy of the measurement. This strong enhancement of this particular molecular resonance makes it possible to spatially map the extension of this molecular orbital using a lock-in technique and a value of  $U_B$  where the gradient in the  $dI/dV$  is highest. Thus a value of  $U_B = -1.64$  V was chosen. As shown in Fig.4.7, the WWPPPPRR dimer exhibits a variation

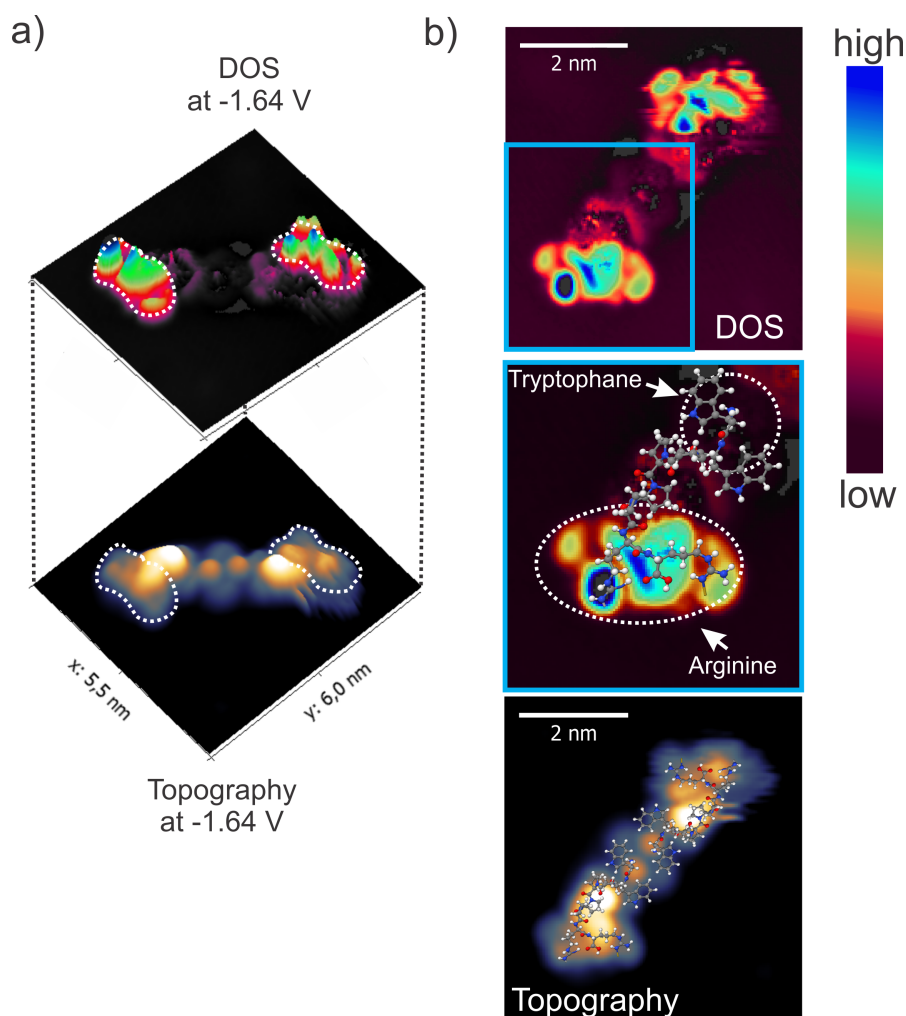


Figure 4.12 – a)  $dI/dV$  map of LDOS with an Arg functionalized STM tip at -1.64 V of a WWPPPP-PRR dimer and simultaneously acquired topography image ( $U_B = -1.64$  V,  $I = 100$  pA (Constant current),  $U_{mod} = 50$  mV,  $f_{mod} = 832$  Hz, time per pixel: 5 ms). The position of the highest signals are marked with a white dotted line and are indicated in both images. b) DOS and topography from a) superimposed with MD model of WWPPPPRR.

in apparent height of about 0.4 nm. To compensate for this height variation and to single out the contribution from the variation of the LDOS, the measurement was performed with activated feedback (constant current mode). The resulting map of the LDOS is depicted in Fig.4.12 a). One can see that the map acquired at -1.64 V shows a strongly spatially localized signal in the DOS. The signal is localized on the outer regions of the dimer. Furthermore some substructure is visible. The LDOS consists of a central lobe and two neighboring small lobes on each side (Fig.4.11 b, blue frame). Especially by comparing the simultaneously recorded STM topography, it is possible to see that the areas of high intensity in the LDOS map do not coincide with the areas of highest apparent height. This indicates that the observed

contrast originates from a variation in the LDOS and is not influenced by the topography of the molecule (white dotted circles Fig.4.12 a)). In tandem with the strong enhancement of the STS signal for a Arg-functionalized STM tip, these results imply a sensitivity towards a specific units in the peptide. Comparing the observed LDOS with the structural model and furthermore assuming that the two monomers are coupled via the Tryp groups and Arg is thus located at the outer edges of the dimer, indicates that the high LDOS is mainly localized on both of the two Arg groups and the C-terminal of the peptide.

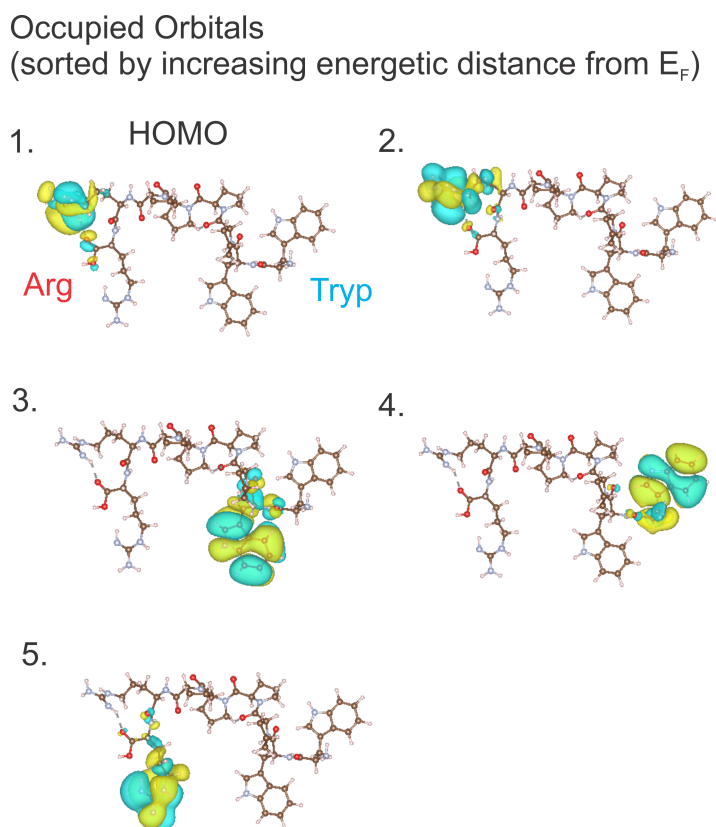


Figure 4.13 – Occupied orbitals as calculated by DFT (gas-phase) based on the structure relaxed on a Au(111) surface. The orbitals are sorted by their energetic distance from  $E_F$  starting from the HOMO.

In order to understand and rationalize these findings, they are compared to the theoretically derived (DFT) orbitals in close energetic proximity to  $E_F$ . It should be noted that the simulations presented here are performed for the gas-phase. The 5 highest orbitals are depicted in Fig.4.13 starting from the HOMO (1.). One can see that for the HOMO and the HOMO-1, only the top left Arg group and the C-terminal is occupied. The next two orbitals (3. and 4.) are related to the Tryp groups. The lower left Arg group is occupied first in the 5. highest orbital. Orbitals providing LDOS at both Arg groups simultaneously can only be found at

much larger energy distances to  $E_F$  and thus are not considered as relevant for the energy window accessible in a STM experiment. The DFT description is in contrast to the observed LDOS, which by their spatial extension as well as their structure indicates a contribution from both Arg groups. A possible explanation for the deviation of the experimental data from the simulations might be found by taking the hybridization of the peptide orbitals with the metal substrate into account. Thus observation of a LDOS might be possible, which is not solely determined by the spatial extension of the HOMO or LUMO. A similar effect was described in [79] for Cu-pthalocyanine on Cu(100), where a combination of up to seven orbital were necessary to reproduce the experimental results.

On the part of the simulation it should be considered that it was performed for the gas-phase and thus a certain deviation from the experimental results might be possible. Especially the energy distance between the individual molecular states might be reduced due to the interaction with the surface. Furthermore, small variations in the binding geometry of the individual groups might introduce deviations in the calculated LDOS and their sequential order with respect to  $E_F$ .

A strong argument that accounts for a "resonant" tunneling process is the enhancement of the signal observed in STS by a factor of 3 and its dependence on the functional tip apex. This effect supports the hypothesis of a specific sensitivity towards a certain part of the peptide sequence when employing an amino acid modified tip. By comparison with the results obtained from the DFT simulations of the orbital structure, it is implied that an Arg tip results in a sensitivity towards Arg within the peptide sequence.

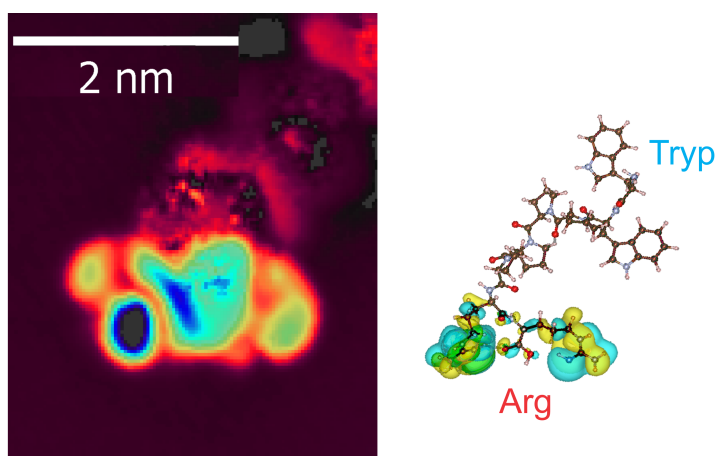


Figure 4.14 – Manually summed occupied orbitals for Arg as calculated by DFT based on the structure relaxed on a Au(111) surface in comparison with the experimentally observed DOS at -1.64 V with an Arg functionalized STM tip.

As it was already shown in the chapter about the amino acids, especially for the STS measure-

ments the status of the tip seems to be crucial. These results hint at the fact, that amino acid modified STM tips enable the observation of the specific electronic structure of the amino acid on the surface not observable with a metallic tip. A similar effect might be present here. One indication for this is the strong enhancement of the intensity of the observed peak. Furthermore the extension of the observed DOS over both of the Arg groups and the C terminal can hint at a sensitivity beyond the HOMO of the WWPPPPRR although an eventual uncertainty of the calculation should be considered. In literature some examples utilizing functional STM tips are described. It was shown by Chen et al. [188] for the observation of a negative differential conductance caused by matching tip and sample orbitals (W and Ni tip on CoPc/Au(111)) that a specific electronic state of the tip enables the observation of certain electronic effects which are obscured otherwise. A similar approach might be useful in the present case to explain the strong enhancement in the observed STS signal. A direct chemical interaction enabled the specific recognition for molecules on a sample. This could be shown by Tanaka et al. [189] for the identification of a nucleic acid on single stranded DNA deposited on Cu(111) by utilizing STM tip with covalently attached nucleic acids. Specific H-bonding between matching nucleic acids on tips and sample facilitated an increase in electron transmission and thus locally enhanced the contrast observed in STM. However it should be noted, that DNA is designed for information storage and thus a read out by specific interaction with probe molecules is enabled. Van der Vegte et al. [190] showed for different probe molecules attached to the tip of an AFM, that depending on their specific chemistry the interactions between tip and sample vary from hydrogen bonding, van der Waals interactions to coulombic interactions. In the present case of Arg a polar interaction or hydrogen bonding might also be plausible. However it is unclear if this process would be specific to Arg-Arg interaction as it is for the matching nucleobases in DNA [191–194]. A process increasing the resolution by a geometric effect due to a smaller terminal tip orbital (apex) (e.g. CO,  $H_2$  modified tips [195]) or sensitivity towards orbital geometries with high spatial gradients (e.g. pentacene functionalized tips [100]) can be most likely excluded. Apart from the strong enhancement of the observed signal in STS after the tip functionalization, only small variations in resolution and shape of the imaged molecules could be noted in topography(c.f. Fig.4.11). To my current knowledge no effect in literature is known for a peptide amino acid interaction explaining this observation. In order to understand the involved processes a simulation of the transmission of the tunneling current through the functionalized tip would be favorable and is planned, similarly as it was performed for the nucleobases immobilized on STM tips in [196].

With our working assumption that the enhanced signal corresponds to a sensitivity to the Arg group, it was possible to gain deeper insight into the various binding motifs of WWPPPPRR dimers on the surface. Thus three types of dimer structures could be identified and are



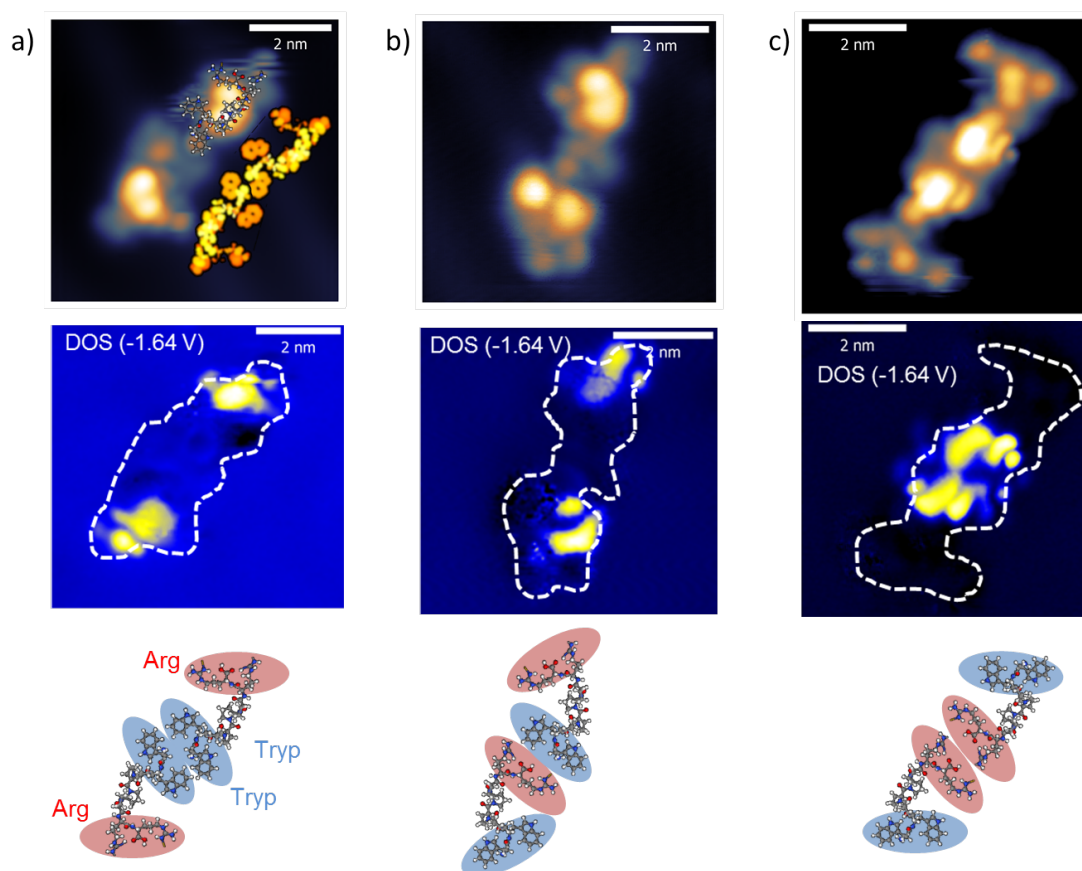


Figure 4.15 – Determination of the Arg position within WWPPPPRR dimer by acquisition of  $dI/dV$  maps using Arg-functionalized tip. The upper row of images shows the STM topography. In the lower row, the simultaneously recorder  $dI/dV$  maps are depicted. a) Symmetric dimer with Tryp as the central part superimposed with chemical structure of WWPPPPRR monomer. For comparison a simulated STM image of a manually arranged dimer is shown. b) Asymmetric dimer with a central part of Arg and Tryp. c) Symmetric dimer with Arg as the central part. (Acquisition parameters:  $I = 100$  pA,  $U_B$  as indicated,  $U_{mod} = 50$  mV,  $f_{mod} = 832$  Hz)

depicted in Fig.4.15. Fig.4.15a) shows the STM topography and corresponding LDOS of Arg of a symmetric dimer as it was discussed before. Furthermore, dimers with other binding motifs can be found as shown in b) and c). For the dimer shown in b), the specific resonance of Arg is located for one monomer at the terminal position according to the case of the dimer discussed before. For the second monomer, the observed LDOS is shifted towards the center of the dimer. For the structure depicted in c) a clear difference in conformation can already be seen in the STM topography. For this dimer, the LDOS is for both monomers located in the center of the dimer. The depicted dimers can thus be identified as asymmetrically bound dimer (Fig.4.15b)) with Tryp and Arg meeting in the center, and an inversely assembled symmetrically dimer (Fig.4.15c)) with Arg in the center, respectively. A statistical analysis



for 104 observed dimer structures yields that the symmetric dimer is encountered with 70% probability, the asymmetric one with 23% and the inversed symmetric one with 7%. The big difference in occurrence, especially between the symmetric and the inversed symmetric dimer indicates that the interaction of the Trp groups or the N-terminals is the structure determining motif for the dimers. The comparably low fraction of the other two structures hints at the fact that these are rather to be seen as unfavorable binding motifs on a Au(111) surface. The interaction of the Arg groups of two peptides or a mixed Trp-Arg interaction might be suppressed in the initial formation of the dimers and only becomes relevant in the subsequent formation of the chain structures. Even if our working assumption, the sensitivity to Arg with an Arg-functionalized tip is wrong, we can conclude that we have three coupling motifs that can only be explained by an exchange of Trp and Arg groups in the center of the dimer.

To proof how the terminal groups and their various combinations determine the motif, simulations of the different dimer structures and their binding energies are performed. An experiment aiming at the clarification of the role of the N- and C- terminal in the dimer formation is ongoing work. Therefore, a synthetic peptide with the inversed sequence RRPPPPWW will be investigated on a Au(111) surface in a similar experiment. For this sequence the positions of N- and C-terminal are exchanged with respect to WWPPPPRR.

As shown in the beginning another species, namely linear chains of various lengths can be observed on the surface. A detailed STM topography image of a WWPPPPRR chain is depicted in Fig.4.16.

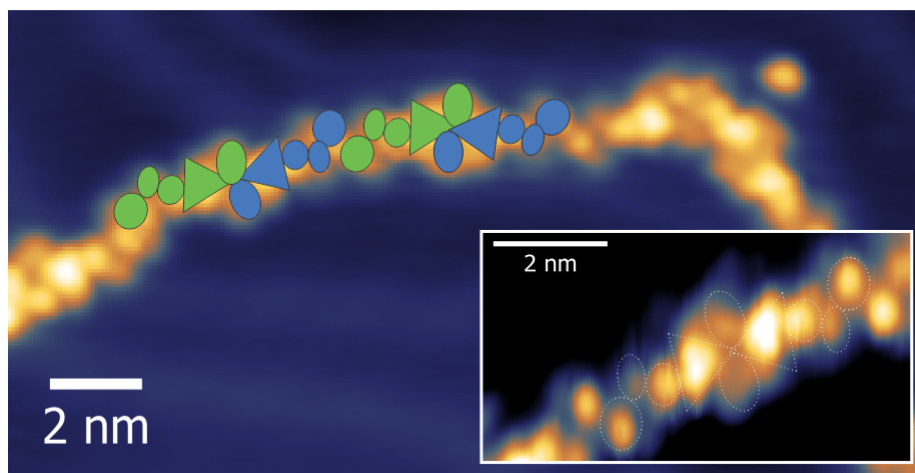


Figure 4.16 – Detail STM topography scan of WWPPPPRR chain superimposed with cartoon visualizing the repeating building blocks of the chain. The inset depicts a detailed STM image of two building blocks of the chain. ( $U_B = -1$  V,  $I = 100$  pA)

The chains are built up by a repeating motif, which consists of 5 features in the STM topograph. One terminal of this motif is formed by a feature appearing as a triangular region with elevated apparent height. The other terminal is formed by a circular feature with lower apparent height (c.f. Fig.4.16). In the linear chain, every other of the motifs is rotated by  $180^\circ$ . This is indicated in Fig.4.16) in the cartoon superimposed with the STM topography image. The alternating building blocks (rotated and non rotated) are discriminated by the colors green and blue. This motif can be observed unperturbed in the straight areas of the chains. Bends or terminal points of the chain cause local defects with varying binding geometry. Upon closer inspection of the bonding geometry, two triangular features point directly at each other, whereas the circular features are arranged under an angle of  $\approx 45^\circ$  with respect to the chain direction, implying that the peptide chain has a bend conformation on the surface. In comparison to the observations discussed for the dimer structures, one can identify two bonding motifs yielding similar contrast in STM topography. The two circular features resemble the Tryp-Tryp bonding scheme of the WWPPPPRR dimers. The elevated triangular features resemble the Arg-Arg bonding motif.

Again, using our working assumption, the identification of the Arg state with an Arg tip could also be demonstrated for the chain structures, in a similar way as for the WWPPPPRR dimers. This is depicted in Fig.4.17 a) and b).

The observation of the same enhanced LDOS in the chains with an Arg-functionalized tip as beforehand discussed for the dimers, gives the possibility to assign the previously introduced cartoon model to the simulated structure and the observed features in STM topography (Fig.4.17c)). The areas of high intensity depicted as triangular shapes correspond to the Arg groups of the peptides. The circular features which resemble the ones observed in the center of the symmetric dimers correspond to Tryp groups and the N-terminal. Especially when comparing the observed Arg DOS for chains with the Arg DOS of the dimer (Fig.4.17b)) one can see a good agreement.

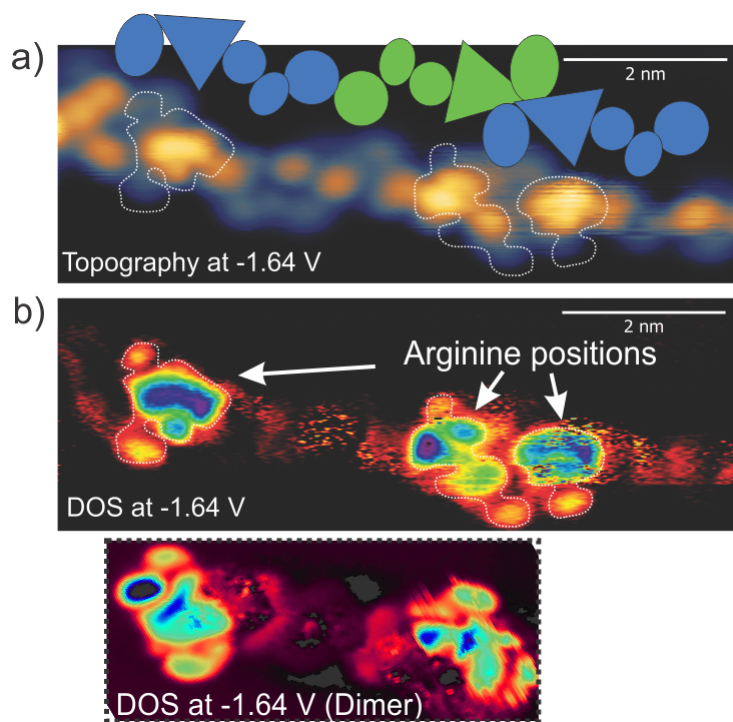


Figure 4.17 – a) Topography of WWPPPPRR chain imaged with Arg functionalized tip. The cartoon model of the WWPPPPRR chain was superimposed with the topography image. b) Simultaneously recorded dI/dV map in comparison with the DOS recorded at a similar energy for a WWPPPPRR dimer ( $U_{Bias}=-1.64$  V,  $U_{mod}=50$  mV, 832 Hz).

### Partial sequencing of WWPPPPRR using a proline functionalized STM tip

For Arg it was shown, that an Arg functional STM tip enabled the specific localization of a specific area within the peptide and most likely to the Arg groups within the peptide or its polymeric compounds. In order to proof the concept as a viable approach for other amino acids, it is necessary to perform additional experiments. Initial tests using proline functionalized tips have been performed. In a two step ES-IBD process first WWPPPPRR and subsequently L-proline was deposited to a Au(111) surface prior to imaging it in the 4K STM. The proline could again be identified by its characteristic tetramers. By controlled manipulation with the STM tip, individual prolines could be isolated and utilized for tip functionalization (Fig.4.18a)). With the so obtained proline tip, a characteristic STS feature on proline could be recorded. On the WWPPPPRR dimer, two characteristic molecular resonances could be identified at  $U_B=-2.2$  V and  $U_B=+2$  V (Fig.4.18b)) which similarly to the Arg case were not observable before. The LDOS corresponding to these peaks could be mapped out spatially as shown in Fig.4.18c). For a proline functionalized tip the dimer was prone to manipulation and furthermore the observed appearance was strongly altered in contrast to a metallic tip. Typically such effects might be caused by a strong mechanical interaction of the probe and

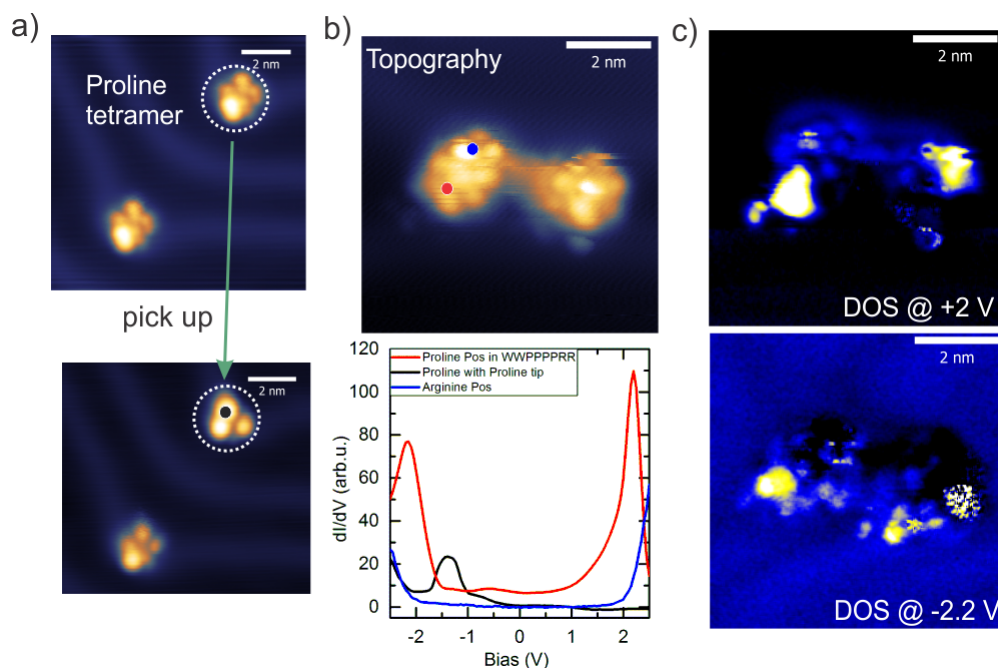


Figure 4.18 – a) STM topography before and after pick up of proline from characteristic proline cluster (Acquisition parameters:  $I = 100$  pA,  $U_B = -1$  V). b) STS of proline with proline functionalized tip (black curve) and of WWPPPPRR on two positions on the WWPPPPRR dimer (red and blue curve). c) Spatial mapping of characteristic STS resonance recorded with proline tip on WWPPPPRR dimer.

the molecule on the sample and could be explained by the upstanding binding geometry of the poly-proline chain. From this measurement a clear assignment of the dimer type and also the exact spatial origin of the observed resonance cannot be deduced. It should be noted that the proline groups do not have any occupied orbitals within 2 eV from  $E_F$  (c.f. Fig. 4.13). This is also reflected in the relatively high energy of  $E - E_F \approx 2$  eV of the molecular resonance of proline in WWPPPPRR. This complicates a clear and stable observation of this peak further. In conclusion it could be shown, that for a proline modified STM tip it becomes possible to observe an enhanced molecular resonance in STS at a different energy position as for an Arg functionalized tip. Furthermore the proline at the tip apex seems to introduce a strong mechanical interaction between tip and sample.

### 4.3 Conclusion

In this chapter it could be shown, that synthetic peptides offer the possibility to study their intricate assembly on surfaces and could be used to develop a methodology to identify individual amino acids within the sequence. Utilizing a simple amino acid sequence consisting of the aromatic L-tryptophan and a poly-L-proline chain as spacer, the self-assembly into

regular 2D-networks could be demonstrated by means of high resolution STM imaging. It was shown, that the networks consist of two types of "windmill"-shaped building blocks only differing by their chirality. Within the networks chiral selective and heterochiral domains could be identified. With the aid of gas-phase relaxations performed for the peptide sequence, the individual building blocks could be assigned to a folded conformation of the synthetic peptide, mediated by H-bonding of the backbone. Upon modifying the sequence and replacing two terminal Tryp units by the polar amino acid L-arginine the on-surface assembly could be tuned. High resolution STM-images of the modified sequence on Au(111) revealed now a self-assembly into ordered chain-like structures and dimers implying an unfolded conformation of the peptide backbone. The unfolded conformation of the peptide could be related to the suppression of hydrogen bonding within the backbone due to a saturation of the C-terminal by the guanine residue of the Arg. By this the observed structure could be rationalized. By co-depositing amino acids the methodology of preparing amino acid functionalized STM tips was applied to the outstretched peptides. For an Arg modified STM tip a significant enhancement of the local STS with respect to a metal tip could be observed at specific areas of the dimer and the chain. To assess to which part of the peptide the tip is sensitive to, DFT calculations of the orbital structure were performed. Comparing these results to on-surface relaxations and simulated STM images of the peptide sequence indicated a good agreement between theory and experiment. A working assumption that the Arg tip is sensitive to the Arg groups in the peptide could be deduced. In a similar experiment the specific resonance of proline as a second amino acid could be identified utilizing a proline functionalized STM tip. As a next step similar measurements with Tryp co-deposited along WWPPPPRR will be performed to proof the concept of specific sensitivity towards individual amino acids. Furthermore negative tests, e.g. trying to observe the Arg resonance with a Tryp modified tip, will be performed. Moreover, the computer models of the peptides on Au(111) will be further refined concerning multiple aspects. On one hand the structural simulation will be refined and extended to various types of dimer motifs and ultimately to the chains. Thus, it will be possible to rationalize the observed structures better and assess the distinct interactions leading to the formation of the observed structures. On the other hand specific simulations of the tunneling process in a junction consisting of an amino acid modified tip and a peptide on a metal surface will be performed. Thereby, we hope to explain the specific mechanism involved in the resonant tunneling process leading to the strongly enhanced signal.

Independent of the exact correlation between the specific functionalized tip and the corresponding part in the peptide, our method is definitively sensitive towards a specific unit in the peptide. This result allows us to conclude that if we can once assign with certainty to which group we are sensitive to, we are able to partially sequence peptides on surfaces.



## 5 Conclusion and Outlook

In the following section a conclusion of the results presented in the respective chapters of this thesis is given.

### 5.1 Conclusion

Scanning probe techniques such as STM at low temperatures and under UHV conditions are an essential tool for imaging molecular species in real space at surfaces with unprecedented resolution. In combination with ES-IBD it becomes now possible to access macromolecules deposited under UHV conditions onto well defined surfaces. Thus ES-IBD as preparation technology extends the accessible range of molecules to biologically relevant non-volatile species. Within this thesis investigations of various molecular species on surfaces enabling structural determination and access to their electronic structure are demonstrated.

Especially the access to rather weak electronic features of molecular species adsorbed on metal surfaces with STS is a challenging task due to hybridization of the molecular orbitals with the electron bath of the metal substrate. A common practice to overcome this obstacle is the utilization of thin insulating layers to electronically decouple the electronic systems of molecule and substrate. In the second Chapter of this thesis the capability of h-BN to effectively decouple a molecular adsorbate from the underlying Rh(111) substrate in the context of STS measurements was analyzed utilizing pentacene as a model system. We could show, that the corrugated h-BN/Rh(111) Moiré-pattern effectively traps the pentacene molecules in a six-fold binding geometry and by comparing the HOMO-LUMO gap of pentacene on h-BN to its gap on a selection of KCl/metal systems the dependence of the energetic position of the molecular orbitals to the respective substrate could be determined. By this an existing model for the interaction strength of molecules with metal surfaces could be extended to thin dielectric decoupling layers.

As a second part of Chapter 2 we could demonstrate the modification of the well known h-

BN/Rh(111) Moiré pattern to a new, long ranged ordered structure by controlling the amount of carbon contamination in the sub-surface Rh layers. Utilizing XPS and spatial mapping of the FER as experimental tools combined with DFT simulations, carbon clusters consisting of three carbon rings located at well defined positions underneath the h-BN super layer could be identified as the origin of this phenomenon. As an interesting result, a modified reactivity of the new surface could be demonstrated by investigating the adsorption geometry of pentacene.

In the context of STM, large molecular systems such as peptides are not extensively studied yet due to experimental restraints in the sample preparation. However, their biological relevance, their vast chemical and structural versatility and their outstanding functionality, opens with peptides as a molecular class an interesting field of research. As a first step to understand the rather complex systems of peptides, we studied amino acids as their individual building blocks. The amino acids were thermally evaporated onto atomically clean metal surfaces and investigated with STM and STS. Characteristic structural motifs and molecular resonances in STS of the respective amino acids could be identified. As a crucial point of this study we could show, that it was possible to adhere individual amino acids to the STM tip by controlled manipulation. Thereby the access and enhancement of specific molecular resonances of the amino acids was possible.

In Chapter 4 synthetic peptide sequences deposited on Au(111) surfaces by means of ES-IBD were investigated. As a first result the structural properties on the Au(111) surface of a synthetic peptide consisting of the two amino acids L-Tryptophane and L-Proline could be determined by high resolution STM. We could show that the peptide forms extended 2D-networks with domains consisting of two sets of constituents of different chirality. Based on gas-phase models it could be shown that the peptide inherits a folded conformation prior to the deposition, which is retained on the surface. In a second step we could show, that the self assembly of these peptide sequences could be drastically modified from 2D networks to linear chains by exchanging one terminal set of Tryptophane units by the polar amino acid Arginine. By means of high resolution STM imaging, two major species, chain-like aggregates and dimers could be identified and their internal structure determined. The application of two different amino acid modified STM tips enabled a partial sequencing of the deposited peptides.

The work presented here gave further insight into fundamental processes relevant in the context of self-assembly and protein folding. Specific control over the self-assembly and folding of engineered macromolecules, such as peptides into distinct nanostructures is currently investigated with respect to a broad range of research fields. These range for example from the development of interfaces between inorganic and organic systems for future medical



applications (e.g. biosensors, drug delivery)[197] to the development of novel nano-materials based on the self assembly of DNA-protein hybrids [198].

## 5.2 Outlook

In the following section possible pathways for future experiments based on the results of this thesis are presented. First, direct follow-up experiments involving alternative molecular systems on surfaces will be discussed. In a second part the extension of our STM to a combined STM/AFM for the determination of the structure of macromolecules is discussed.

### Synthetic peptides

Synthetic peptide sequences offer a toolbox capable of generating a broad variety of possible self assembled nano structures. In order to rationalize the results presented in this chapter and to gain a deeper understanding of the involved processes, a selection of possible synthetic sequences for future projects is discussed. From the results shown here, it is possible to see that the N- or the C-terminal and their interaction with the neighboring functional residues of the amino acids might play a significant role in the determination of the final surface conformation of the peptides. A possible candidate to study the influence of the polar groups of N and C-terminal is depicted in Fig.5.1a). The depicted sequence is exactly inverted to WWPPPPRR, which was utilized for partial sequencing (c.f. chapter 4). It might be interesting to study the conformation of this sequence on a Au(111) surface and investigate in how far the self-assembly characteristics have been modified with respect to the sequence WWPPPPRR.

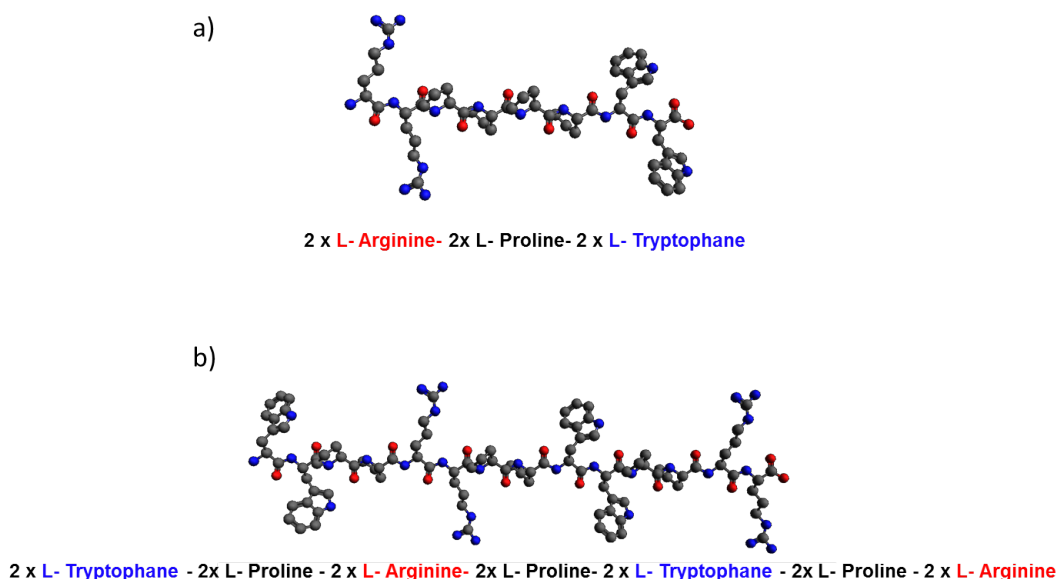


Figure 5.1 – Synthetic peptides with various sequences (a)-b)).

With respect to the identification of individual amino acids in a peptide sequence by means of an amino acid functionalized tip, the sequence depicted in Fig.5.1b) is a potential candidate as well. An extended peptide chain with an alternating sequence of amino acids might be used to test the capability to successfully identify individual amino acids in larger compounds. The design as alternating pattern of repeating building blocks as shown in the presented sequence, might facilitate a more reliable proof for the sensitivity towards a specific amino acid. For elongated peptide sequences an aspect that needs to be considered is the on-surface conformation. An unfolded conformation is desirable to enable resolving individual amino acids in the chain. As it was shown in [36], large bio-polymers such as cytochrome-C can be deposited by ES-IBD in a preferentially unfolded conformation on a suitable surface. The outstretched geometry is thereby induced by Coulomb-repulsion of the individual charges distributed over the peptide sequence. For a more reactive metal substrate, such as Cu(001) [36] the concept of a high-charge state deposition might be transferred to larger peptide sequences as for example the one presented in Fig.5.1b).

In order to develop more general design principles for the development of novel sequences, more aspects need to be considered. Peptides try to form compact structures depending on the on-surface diffusion and the interaction of the amino acid chain with itself. A compact conformation is preferred due to the unpolar characteristic of the UHV environment, which forces the polar groups to self-passivate [181]. For flexible sequences and inert surfaces, such as Au(111), self-passivation by folding is a common motif. Thereby, conformations for which unpolar groups point outwards and the polar residues are located in the inside are generated. For sequences with only a limited capability to self-passivate, due to steric hindrance and an inert substrate allowing for diffusion, the passivation by dimer or multimer formation becomes preferable. This was reported for the natural peptide At-II on Cu(111) in [13]. Moreover, based on the results presented by So et al. in [177] and [138] for the assembly and binding of engineered peptides to surfaces, the design of future synthetic sequences for our experiments can be refined. Amino acid sequences can be chosen as such that outstretched conformations and flat binding geometries are preferred. Examples for amino acids inducing flat binding geometries on metal substrates might be Phenylalanine [161] or Cysteine, which exhibit a flat on-surface conformation due to the specific adsorption of aromatic residues to metal surfaces or bond formation of sulfur containing groups with the metal substrate.

Thus an approach to prevent folding of the peptide backbone might be the realization of synthetic sequences containing sterically demanding amino acids. Additionally introducing amino acids which exhibit planar binding geometries to a metal surface might be a viable concept. Furthermore, the conformation and assembly of the resulting structures can be tuned by choosing a suitable metal substrate.

### Natural peptides: Angiotensin-II

As a consecutive step to test the proposed concept of identifying amino acids with functional amino acid tips, natural peptides on surfaces can be utilized. Two promising candidates for this might be the peptides bradykinin (BK) and angiotensin-II (AT-II), since both have been extensively investigated on low-index metal surfaces using STM and can exhibit planar adsorption geometry for suitable metal substrates. Results on AT-II on Au(111) published in [13] show, that the peptide assembles in long-range ordered self assembled honeycomb networks comprised of flat-lying building blocks. In experiments performed on a Cu(111) surface smaller dimer and trimer structures were reported to form as repeating conformational motifs [199]. For BK on Cu(110)[37] two-dimensionally folded peptides were reported as monomer or dimer structures. Although folded, the individual residues were adsorbed in a flat geometry on the surface and could be allocated to separate features in the STM topography. Because of their well studied on-surface conformation and their specific binding geometries AT-II and BK might be ideal benchmarks for the sequencing of natural peptides. For AT-II we investigated the possibility of utilizing decoupling layers, such as h-BN/Rh(111). Depositing AT-II onto this surface leads to structures as they are exemplary depicted in Fig.5.2a)

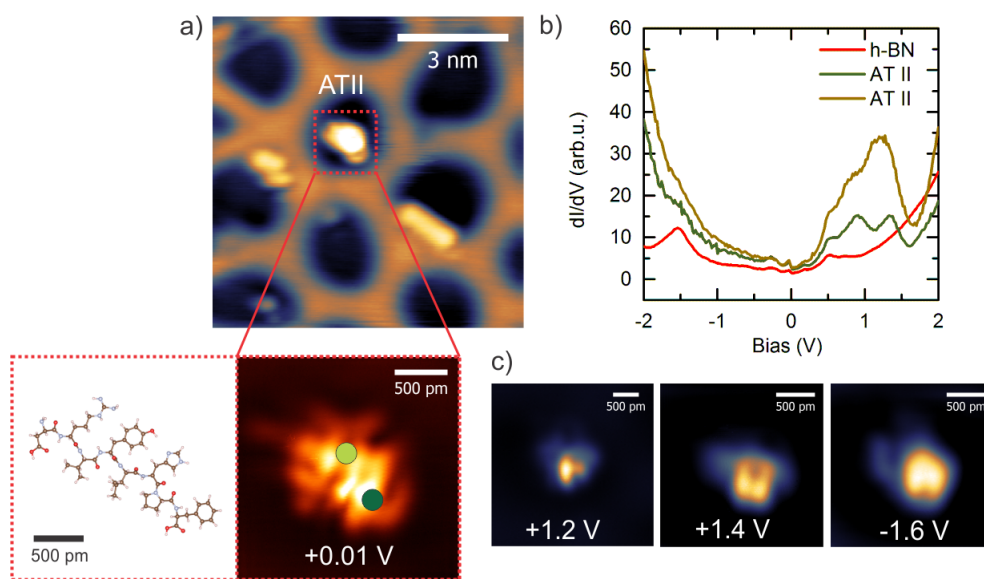


Figure 5.2 – a) AT-II deposited on h-BN/Rh(111) ( $U_B = -1$  V,  $I = 100$  pA). The inset depicts a high resolution scan of the dotted area in comparison to the chemical structure of AT-II. The two circles correspond to the STS measurements with similar color code depicted in b). c) Spatial mapping of the molecular resonances at the depicted voltages.

The size of the observed structure matches the dimensions of an AT-II monomer. However, one major drawback of decoupling layers is the low interaction with the molecular adsorbents.

In combination with the comparably high complexity and conformational freedom of peptides a high variability of the resulting on-surface conformations of molecules can be observed. Since the presented results are only a preliminary study, no detailed structural analysis can be performed yet. However, performing STS measurements on the AT-II molecules reveals a multitude of molecular resonances (light and dark green graphs Fig.5.2b)). The reference measurement on h-BN revealed that the tip was functionalized, presumably with another AT-II molecule. Utilizing a functional tip, it was possible to spatially map out the corresponding distribution of the LDOS over the observed molecule. These are interesting initial results offering another pathway to the identification of individual amino acids within a peptide by enabling good access to their electronic structure on electronically decoupling layers.

### 5.2.1 Combined STM/AFM

An important aspect for the understanding of macromolecules on surfaces is to gain knowledge about the adsorption geometry of individual groups and thereby to facilitate the identification of certain functional residues. Topographic information obtained in an STM experiment are always a convolution of the electronic LDOS and the height information and cannot necessarily be deconvoluted. Another aspect, which is especially relevant to elucidate the origin of the increased signal in STS for amino acid functionalized STM tips on peptides, might be to study the mechanical tip sample interaction. Both of these aspects, the study of structure determination and the mechanical tip sample interaction can be probed using an AFM. Therefore, we modified our STM setup to a combined STM/AFM capable to address the electronic and the structural characteristics of deposited molecules. In 1995 Giessibl et al. [200] proposed with the so called "q-plus" sensor a novel sensor design for scanning probe applications. The original design utilized a stiff quartz tuning fork commonly used as time-keeper in wrist watches for a cantilever of an AFM set up. One prong of the tuning fork was mounted firmly to a comparably large weight. At the end of the other prong a sharp conductive tip is attached allowing for simultaneous STM measurement. The piezo-electric material of the tuning fork material allows for direct all-electric read-out of the AFM signal.

Due to the increased stiffness of the cantilever and its high q-factor an operation with low oscillation amplitudes in the range of 1 Å is possible [203]. This allowed for simultaneous STM and nc-AFM measurements or in other words to simultaneously probe the forces acting between tip and sample and the electronic structure of a sample [203]. For high resolution nc-AFM measurements with CO functionalized tips it was shown for aromatic molecules adsorbed in a flat geometry [204][205] that it is possible to achieve impressive resolution capable to image individual bonds and thus directly observe the molecular structure. An example for this is shown in Fig.5.3a) for a high-resolution measurement on pentacene making individual

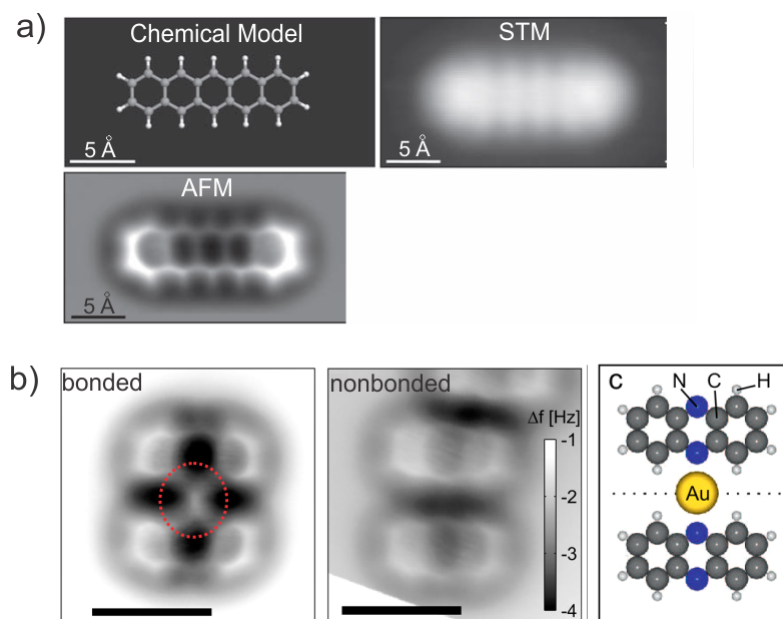


Figure 5.3 – a) The chemical structure of pentacene resolved by high resolution nc-AFM and STM with CO functionalized tip (Modified from: Gross et al., Science 2009 [201]). b) Formation of a complex between an Au-atom and two phenazine molecule observed by nc-AFM. The dotted red circle indicates the position of the Au-atom. (Modified from: Albrecht et al., Journal of American Chemical Society, 2013 [202]).

atomic bonds visible.

Using high-resolution nc-AFM the molecular properties, such as the specific conformation of tetraphenylporphyrin (2H-TPP) and copper-metalated tetraphenylporphyrin (Cu-TPP) on Cu(111) [206] could be identified. Furthermore, it was possible to observe the formation of molecule-metal complexes between phenazine and a Au-atom [202]. Two AFM-topography images of complexated and unbonded phenazine molecules are depicted in Fig.5.3b). It can be seen that it is possible to pinpoint the specific geometry of the complex and the location of the involved metal atom. Another interesting possibility opening up with this technique is the experimental observation of charges or molecular polarization by high resolution AFM based Kelvin-Probe microscopy [110] as it was shown in [207]. This might be a valuable technique to identify functional polar residues as they can be found in certain amino acids.

Although challenging, the experimental technique of combined STM and nc-AFM might be a promising approach to gain intra-molecular resolution on peptides and thereby enabling a novel approach for the on-surface sequencing of these molecules. Employing high resolution imaging with functionalized tips, either for structural imaging (e.g. CO functionalized-tip) or the identification of specific electronic features based on the result presented in this thesis, might be a good approach to investigate peptides on surfaces with STM/AFM. Although not

## Chapter 5. Conclusion and Outlook

---

all groups of the synthetic peptide utilized in this thesis adsorbed flat on the metal substrate, the identification by AFM of characteristic planar areas, such as the indole residues of Trp might be still possible. Further utilizing Kelvin-probe techniques might allow to discriminate between polar and unpolar residues of certain amino acids within the sequence. Therefore, an experimental set-up based on the design of the 4K-STM utilized in this work was developed and built up. The system was subsequently moved to a laboratory optimized as ultra-low noise environment and is currently optimized there. In order to benchmark the new set up, first samples will be flat lying aromatic molecules such as pentacene and its derivatives. In a subsequent step the synthetic peptide sequences discussed in this thesis will be investigated with high-resolution nc-AFM.

# Acknowledgements

During the time of my Ph.D., I worked with quite a number of people, whom I'd like to thank at this place for their support.

First of all I would like to thank my thesis director Prof. Klaus Kern for accepting me as a Ph.D.-student and giving me the chance to work in his group at the Max-Planck Institute for Solid State Research. I was very glad to be given the chance to participate in the extraordinary research that is performed at this place.

Especially I would like to thank Dr. Uta Schlickum as my daily supervisor for your support and guidance throughout my thesis. I appreciated the freedom and advice that was given to me in searching for my own projects and our fruitful discussions about new ideas. On the same note I would like to thank Dr. Daniel Rosenblatt as my predecessor and the person who build up the STM. I was really fortunate to have you as a colleague and work together with you and learn all the quirks and little things you need to know in the lab.

Furthermore, I would like to thank the entire ES-IBD group around Dr. Stephan Rauschenbach for all their work and expertise that made it possible for me to perform the experiments. It was a pleasure working with you. Especially I would like to thank Dr. Sabine Abb for her unwavering patience in preparing and performing the depositions and her scientific input in understanding the data.

For the good collaboration, the good discussions and all the nice conversations we had I would like to thank Prof. Talat Rahman. She and her group performed simulations of our data, which enabled us to understand it. In a similar way I would like to thank Prof. Christian Schön, Dr. Juan Cortes, Dr. Bohdan Andriyevskyy and Prof. Christina Oligschleger for their theory support. Similarly, I highly appreciate the work of Dr. Rico Gutzler, who transformed the theoretical models into simulated STM images and helped me to make sense of them.

I was very glad to work together and exchange ideas with a number of experienced scientists in our work group and thus like to thank Dr. Markus Etzkorn, Dr. Markus Ternes, Dr. Klaus

## Acknowledgements

---

Kuhnke, Dr. Bastian Kern for their support.

Among the people working here, I found many good colleagues and friends inside and outside of the institute. For all the fun lunch breaks, coffees, running sessions, teas, cakes, barbecues and many more I would like to thank: Dr. Kristina Vaklinova, Dr. Sabine Abb, Mathias Müunks, Diana Hötger, Jacob Senkpiel, Shai Mangel, Patrick Alexa, Tomasz Michnowicz, Anna Roslawska, Marcel Pristl, Dr. Roberto Urcuyo, Dr. Tom White, Dr. Berthold Jäck, Dr. Verena Schendel, Dr. Bastian Kern.

On a special note I would like to mention my colleague and office mate Lukas Schlipf. I am very glad that I could work, laugh, drink ... and in general have a good time with you for the last four years. Thank you for being an amazing friend.

I would like to express my gratitude to my parents for their continuous faith in me and their support that made it possible for me to pursue my way. Thank you for everything! Another important member of my family who always stood beside me and supported me was my cousin Katrin. I am very grateful for your advice and your friendship.

Above all, I want to thank Jörg for all his love and support throughout this time. You accompanied me through the ups and downs of my thesis and helped me to find my way. I am looking forward to see where this way will take us in the future.

*Lausanne, June 2017*

S. K.



## Bibliography

1. Lee, I., Lee, J. W. & Greenbaum, E. Biomolecular electronics: Vectorial arrays of photosynthetic reaction centers. *Physical Review Letters* **79**, 3294–3297 (1997) (page 1).
2. Moser, C. C., Keske, J. M., Warncke, K & Dutton, P. L. Electron transfer in photosynthetic reaction centers. *Stud.Phys.Theor.Chem.* **78**, 111–125 (1992) (page 1).
3. Gerster, D. *et al.* Photocurrent of a single photosynthetic protein. *Nature Nanotechnology* **7**, 673–676 (2012) (page 1).
4. D'Souza, F. *et al.* Photosynthetic reaction center mimicry: Low reorganization energy driven charge stabilization in self-assembled cofacial zinc phthalocyanine dimer-fullerene conjugate. *Journal of the American Chemical Society* **131**, 8787–8797 (2009) (page 2).
5. Wöhri, A. B. *et al.* Light-induced structural changes in a photosynthetic reaction center caught by Laue diffraction. *Science* **328**, 630–3 (2010) (page 2).
6. Freund, H. J. & Pacchioni, G. Oxide ultra-thin films on metals: new materials for the design of supported metal catalysts. *Chemical Society Reviews* **37**, 2224–2242 (2008) (page 1).
7. Den Boer, D. *et al.* Detection of different oxidation states of individual manganese porphyrins during their reaction with oxygen at a solid/liquid interface. *Nature Chemistry* **5**, 621–627 (2013) (page 1).
8. Kovaric, B. C. *et al.* Self-assembly of peptide porphyrin complexes: Toward the development of smart biomaterials. *Journal of the American Chemical Society* **128**, 4166–4167 (2006) (page 1).
9. Morgenstern, K. Switching individual molecules by light and electrons: From isomerisation to chirality flip. *Progress in Surface Science* **86**, 115–161 (2011) (page 1).
10. Mahapatra, M. *et al.* Formation of induced-fit chiral templates by amino acid-functionalized Pd(111) surfaces. *Journal of Physical Chemistry C* **119**, 3556–3563 (2015) (page 1).

## Bibliography

---

11. Lingenfelder, M. *et al.* Tracking the chiral recognition of adsorbed dipeptides at the single-molecule level. *Angewandte Chemie - International Edition* **46**, 4492–4495 (2007) (pages 1, 57–59, 78).
12. Stepanow, S. *et al.* Surface-assisted assembly of 2D metal-organic networks that exhibit unusual threefold coordination symmetry. *Angewandte Chemie - International Edition* **46**, 710–713 (2007) (pages 1, 4).
13. Abb, S, Harnau, L, Gutzler, R, Rauschenbach, S & Kern, K. Two-dimensional honeycomb network through sequence-controlled self-assembly of oligopeptides. *Nature communications* **7**, 10335 (2016) (pages 1, 4, 60, 74, 83, 90, 108, 109).
14. Zhang, S. Fabrication of novel biomaterials through molecular self-assembly. *Nature Biotechnology* **21**, 1171–1178 (2003) (pages 1, 78).
15. Ringler, P. Self-Assembly of Proteins into Designed Networks. *Science* **302**, 106–109 (2003) (pages 1, 57).
16. Guo, X. *et al.* Covalently Bridging Gaps in Single-Walled Carbon Nanotubes with Conducting Molecules. *Science* **311**, 356–359 (2006) (page 1).
17. Matsuda, K. *et al.* Conductance photoswitching of diarylethene-gold nanoparticle network induced by photochromic reaction. *Journal of Physical Chemistry C* **112**, 17005–17010 (2008) (page 1).
18. Eelkema, R. *et al.* Molecular machines: nanomotor rotates microscale objects. *Nature* **440**, 163 (2006) (page 1).
19. Browne, W. R. & Feringa, B. L. Making molecular machines work. *Nature nanotechnology* **1**, 25–35 (2006) (page 1).
20. Whitesides, G. M., Kriebel, J. K. & Mayers, B. T. in *Nanoscale Assembly* 217–239 (Springer US, Boston, MA, 2013) (page 1).
21. Whitesides, G. M. Self-Assembly at All Scales. *Science* **295**, 2418–2421 (2002) (page 1).
22. Mendes, A. C., Baran, E. T., Reis, R. L. & Azevedo, H. S. Self-assembly in nature: Using the principles of nature to create complex nanobiomaterials. *Wiley Interdisciplinary Reviews: Nanomedicine and Nanobiotechnology* **5**, 582–612 (2013) (pages 2, 3, 57, 58, 63, 68, 77).
23. Dill, K. A. & MacCallum, J. L. The Protein-Folding Problem, 50 Years On. *Science* **338**, 1042–1046 (2012) (pages 2, 22, 57).
24. Ulijn, R. V. & Smith, A. M. Designing peptide based nanomaterials. *Chemical Society reviews* **37**, 664–675 (2008) (page 2).

25. Yoshida, M., Muneyuki, E. & Hisabori, T. ATP synthase—a marvellous rotary engine of the cell. *Nature reviews. Molecular cell biology* **2**, 669–77 (2001) (pages 2, 3).
26. Stock, D., Leslie, A. G. & Walker, J. E. Molecular architecture of the rotary motor in ATP synthase. *Science (New York, N.Y.)* **286**, 1700–5 (1999) (pages 2, 3).
27. Svergun, D. I., Petoukhov, M. V. & Koch, M. H. Determination of domain structure of proteins from X-ray solution scattering. *Biophysical journal* **80**, 2946–2953 (2001) (page 3).
28. Van den Berg, B. *et al.* X-ray structure of a protein-conducting channel. *Nature* **427**, 36–44 (2004) (page 3).
29. Eng, J. K., McCormack, A. L. & Yates, J. R. An approach to correlate tandem mass spectral data of peptides with amino acid sequences in a protein database. *Journal of the American Society for Mass Spectrometry* **5**, 976–989 (1994) (page 3).
30. Hunt, D. F., Yates Iii, J. R., Shabanowitz, J., Winston, S. & Hauer, C. R. Protein sequencing by tandem mass spectrometry (collision-activated dissociation/liquid secondary-ion mass spectrometry/apolipoprotein B). *Proc. Natl. Acad. Sci.* **83** (1986) (page 3).
31. Fairman, R. & Åkerfeldt, K. S. Peptides as novel smart materials. *Current Opinion in Structural Biology* **15**, 453–463 (2005) (pages 3, 4).
32. Behanna, H. A., Donners, J. J. M., Gordon, A. C. & Stupp, S. I. Coassembly of amphiphiles with opposite peptide polarities into nanofibers. *Journal of the American Chemical Society* **127**, 1193–1200 (2005) (page 3).
33. Hamley, I. W. Peptide fibrillization. *Angewandte Chemie - International Edition* **46**, 8128–8147 (2007) (pages 3, 4).
34. Roth, A. E. *Nobel prize lecture* 2012 (page 4).
35. Repp, J., Meyer, G., Stojkovi, S. M., Gourdon, A. & Joachim, C. Molecules on insulating films: Scanning-tunneling microscopy imaging of individual molecular orbitals. *Physical Review Letters* **94**, 1–4 (2005) (pages 4, 10, 12, 14, 23, 24, 30, 31, 60, 66, 75).
36. Deng, Z. *et al.* A close look at proteins: Submolecular resolution of two- and three-dimensionally folded cytochrome c at surfaces. *Nano Letters* **12**, 2452–2458 (2012) (pages 4, 20, 22, 57, 108).
37. Rauschenbach, S. *et al.* Two-Dimensional Folding of Polypeptides into Molecular Nanostructures. *ACS Nano* **11**, acsnano.6b06145 (2017) (pages 4, 57, 74, 83, 109).

## Bibliography

---

38. Rauschenbach, S. *et al.* Electrospray ion beam deposition: Soft-landing and fragmentation of functional molecules at solid surfaces. *ACS Nano* **3**, 2901–2910 (2009) (pages 4, 19, 20).
39. W. Chan, P. W. *Fmoc Solid Phase Peptide Synthesis A Practical Approach* 370 pages (Oxford University Press, 1999) (pages 4, 77).
40. Lin, Y. Y., Gundlach, D. J., Nelson, S. F. & Jackson, T. N. Stacked pentacene layer organic thin-film transistors with improved characteristics. *IEEE Electron Device Letters* **18**, 606–608 (1997) (page 4).
41. Wang, Z. S., Kwek, L. C., Lai, C. H. & Oh, C. H. Quantum tunneling time. *Physical Review A - Atomic, Molecular, and Optical Physics* **69**, 052108–1 (2004) (page 7).
42. Kopfermann, H. & Ladenburg, R. Full-Text. *Nature* **122**, 439 (1928) (page 7).
43. Esaki, L. New phenomenon in narrow germanium p-n junctions [3]. *Physical Review* **109**, 603–604 (1958) (page 8).
44. Binnig, G., Rohrer, H., Gerber, C. & Weibel, E. Surface studies by scanning tunneling microscopy. *Physical Review Letters* **49**, 57–61 (1982) (page 8).
45. Muller, E. W. Field Ion Microscopy. *Science* **149**, 591–601 (1965) (page 8).
46. Bény-Bassez, C., R. in *A.M.F. O'Hare (Ed.), SEM Inc, Chicago* 119 (Wiley-VCH Verlag GmbH & Co. KGaA, Weinheim, Germany, 1985). arXiv: arXiv:1011.1669v3 (page 8).
47. Reifenberger, R. in *Fundamentals of Atomic Force Microscopy* 1–20 (Springer Berlin Heidelberg, 2015) (pages 8–10, 12).
48. Tersoff, J & Hamann, D. Theory and application for the scanning tunneling microscope. *Physical review letters* **50**, 1998 (1983) (pages 10, 14).
49. Stroscio, J. A. & Kaiser, W. J. Scanning tunneling microscopy. *Methods of Experimental Physics* **27**, 459 (1993) (page 10).
50. Barth, J. V., Brune, H., Ertl, G. & Behm, R. J. Scanning tunneling microscopy observations on the reconstructed Au(111) surface: Atomic structure, long-range superstructure, rotational domains, and surface defects. *Physical Review B* **42**, 9307–9318 (1990) (page 10).
51. Hasegawa, Y. & Avouris, P. Direct observation of standing wave formation at surface steps using scanning tunneling spectroscopy. *Physical Review Letters* **71**, 1071–1074 (1993) (page 10).
52. Crommie, M. F., Lutz, C. P., Eigler, D. M. & Heller, E. J. Quantum corrals. *Physica D: Nonlinear Phenomena* **83**, 98–108 (1995) (page 10).

53. Bardeen, J. Tunnelling from a many-particle point of view. *Physical Review Letters* **6**, 57–59 (1961) (page 11).
54. Hoermandinger, G. Imaging of the Cu(111) surface state in scanning tunneling microscopy. *Physical Review B* **49**, 13897–13905 (1994) (page 12).
55. Lu, X., Grobis, M., Khoo, K. H., Louie, S. G. & Crommie, M. F. Spatially Mapping the Spectral Density of a Single C60 Molecule. *Physical Review Letters* **90**, 096802 (2003) (page 12).
56. Wagner, C. & Temirov, R. Tunnelling junctions with additional degrees of freedom: An extended toolbox of scanning probe microscopy. *Progress in Surface Science* **90**, 194–222 (2015) (pages 12, 13).
57. Eigler, D. M., Weiss, P. S., Schweizer, E. K. & Lang, N. D. Imaging Xe with a low-temperature scanning tunneling microscope. *Physical Review Letters* **66**, 1189–1192 (1991) (pages 12, 66).
58. Bartels, L, Meyer, G & Rieder, K.-H. High-resolution spectroscopy of weakly chemisorbed species using a low-temperature scanning tunneling microscope (STM): CO/Cu(111). *Chemical Physics Letters* **297**, 287–292 (1998) (page 13).
59. Gupta, J. A., Lutz, C. P., Heinrich, A. J. & Eigler, D. M. Strongly coverage-dependent excitations of adsorbed molecular hydrogen. *Physical Review B - Condensed Matter and Materials Physics* **71**, 115416 (2005) (page 13).
60. Temirov, R., Soubatch, S., Neucheva, O., Lassise, A. C. & Tautz, F. S. A novel method achieving ultra-high geometrical resolution in scanning tunnelling microscopy. *New Journal of Physics* **10**, 053012 (2008) (page 13).
61. Kichin, G., Weiss, C., Wagner, C., Tautz, F. S. & Temirov, R. Single molecule and single atom sensors for atomic resolution imaging of chemically complex surfaces. *Journal of the American Chemical Society* **133**, 16847–16851 (2011) (page 13).
62. Kichin, G., Wagner, C., Tautz, F. S. & Temirov, R. Calibrating atomic-scale force sensors installed at the tip apex of a scanning tunneling microscope. *Physical Review B - Condensed Matter and Materials Physics* **87**, 081408 (2013) (page 14).
63. Kelly, K. F., Sarkar, D., Hale, G. D., Oldenburg, S. J. & Halas, N. J. Threefold Electron Scattering on Graphite Observed with C60-Adsorbed STM Tips. *Science* **273**, 1371–1373 (1996) (page 14).

## Bibliography

---

64. Mándi, G. & Palotás, K. Chen's derivative rule revisited: Role of tip-orbital interference in STM. *Physical Review B - Condensed Matter and Materials Physics* **91**, 1–12 (2015) (page 14).
65. Selloni, A., Carnevali, P., Tosatti, E. & Chen, C. D. Voltage-dependent scanning-tunneling microscopy of a crystal surface: Graphite. *Physical Review B* **31**, 2602–2605 (1985) (page 14).
66. Gross, L. *et al.* High-resolution molecular orbital imaging using a p-wave STM tip. *Physical Review Letters* **107**, 086101 (2011) (page 15).
67. Assig, M. *et al.* A 10 mK scanning tunneling microscope operating in ultra high vacuum and high magnetic fields. *The Review of scientific instruments* **84**, 033903 (2013) (page 17).
68. Fenn, J. B. Electrospray ionization mass spectrometry: How it all began. *Journal of Biomolecular Techniques* **13**, 101–118 (2002) (page 19).
69. Fenn, J. B. Electrospray wings for molecular elephants (Nobel lecture). *Angewandte Chemie - International Edition* **42**, 3871–3894 (2003) (page 19).
70. Loo, J. a. Studying noncovalent protein complexes by electrospray ionization mass spectrometry. *Mass spectrometry reviews* **16**, 1–23 (1997) (pages 19, 20).
71. Wagner, I. & Musso, H. New Naturally Occurring Amino Acids. *Angewandte Chemie International Edition in English* **22**, 816–828 (1983) (pages 20, 57).
72. Ramachandran, G. N., Ramakrishnan, C & Sasisekharan, V. Stereochemistry of polypeptide chain configurations. *Journal of molecular biology* **7**, 95–99 (1963) (page 21).
73. Perutz, M. F. *et al.* Structure of Hæmoglobin: A Three-Dimensional Fourier Synthesis at 5.5Å. Resolution, Obtained by X-Ray Analysis. *Nature* **185**, 416–422 (1960) (page 22).
74. Kühnle, A., Linderöth, T. R., Schunack, M. & Besenbacher, F. L-cysteine adsorption structures on Au(111) investigated by scanning tunneling microscopy under ultrahigh vacuum conditions. *Langmuir* **22**, 2156–2160 (2006) (pages 22, 57).
75. Wang, Y., Lingenfelder, M., Classen, T., Costantini, G. & Kern, K. Ordering of dipeptide chains on Cu surfaces through 2D cocrystallization. *Journal of the American Chemical Society* **129**, 15742–15743 (2007) (page 22).
76. Ohtani, H., Wilson, R. J., Chiang, S. & Mate, C. M. Scanning tunneling microscopy observations of benzene molecules on the Rh(111)-(3 x 3) (C<sub>6</sub>H<sub>6</sub> + 2CO) surface. *Physical Review Letters* **60**, 2398–2401 (1988) (page 23).

77. Lee, H. S. Bias-Dependent STM Image Contrast Study of Phenyl octadecyl Ethers Physisorbed onto Highly Oriented Pyrolytic Graphite. *Langmuir* **14**, 7475–7483 (1998) (page 23).
78. Lippel, P. H., Wilson, R. J., Miller, M. D., Woell, C. & Chiang, S. High-Resolution Imaging of Copper-Phthalocyanine by Scanning-Tunneling Microscopy. *Physical Review Letters* **62**, 171–174 (1989) (page 23).
79. Sautet, P. & Joachim, C. Interpretation of STM images: copper-phthalocyanine on copper. *Surface Science* **271**, 387–394 (1992) (pages 23, 96).
80. Bennewitz, R. *et al.* Aspects of Dynamic Force Microscopy on NaCl / Cu ( 111 ) : Resolution , Tip – Sample Interactions and Cantilever Oscillation Characteristics. *Surf. Interface Anal.* **27**, 462–467 (1999) (page 23).
81. Fölsch, S., Barjenbruch, U. & Henzler, M. Atomically thin epitaxial films of NaCl on germanium. *Thin Solid Films* **172**, 123–132 (1989) (pages 23, 35).
82. Baeumer, M. & Freund, H. J. Metal deposits on well-ordered oxide films. *Progress in Surface Science* **61**, 127–198 (1999) (page 23).
83. Kresse, G. *et al.* Structure of the Ultrathin Aluminum Oxide Film on NiAl(110). *Science* **308**, 1440–1442 (2005) (page 23).
84. Liljeroth, P., Repp, J. & Meyer, G. Current-Induced Hydrogen Tautomerization and Conductance Switching of Naphthalocyanine Molecules. *Science* **317**, 1203–1206 (2007) (page 23).
85. Villagomez, C. J. *et al.* STM images of a large organic molecule adsorbed on a bare metal substrate or on a thin insulating layer: Visualization of HOMO and LUMO. *Surface Science* **603**, 1526–1532 (2009) (pages 24, 28, 60).
86. Dil, H. *et al.* Surface Trapping of Atoms and Molecules with Dipole Rings. *en. Science* **319**, 1824–1826 (2008) (pages 24, 25, 29, 46).
87. Watanabe, K., Taniguchi, T. & Kanda, H. Direct-bandgap properties and evidence for ultraviolet lasing of hexagonal boron nitride single crystal. *Nature materials* **3**, 404–409 (2004) (pages 24, 26).
88. Kim, K. K., Kim, S. M. & Lee, Y. H. A New Horizon for Hexagonal Boron Nitride Film. *Journal of the Korean Physical Society* **64**, 1605–1616 (2014) (page 24).
89. Joshi, S. *et al.* Boron Nitride on Cu (111): An Electronically Corrugated Monolayer. *Nano Letters* **12**, 5821–5828 (2012) (pages 24, 25).

## Bibliography

---

90. Orlando, F. *et al.* Epitaxial growth of hexagonal boron nitride on Ir(111). *Journal of Physical Chemistry C* **116**, 157–164 (2012) (page 24).
91. Orlando, F. *et al.* Epitaxial growth of hexagonal boron nitride on Ir(111). *Journal of Physical Chemistry C* **116**, 157–164 (2012) (page 24).
92. Nagashima, A., Tejima, N., Gamou, Y., Kawai, T. & Oshima, C. Electronic states of monolayer hexagonal boron nitride formed on the metal surfaces. *Surface Science* **357–358**, 307–311 (1996) (page 24).
93. Nagashima, A., Tejima, N., Gamou, Y., Kawai, T. & Oshima, C. Electronic structure of monolayer hexagonal boron nitride physisorbed on metal surfaces. *Physical Review Letters* **75**, 3918–3921 (1995) (page 24).
94. Corso, M., Corso, M., Auwa, W., Muntwiler, M. & Tamai, A. Boron Nitride Nanomesh. *Science (New York, N.Y.)* **217**, 217–221 (2012) (pages 24–26).
95. Yang, Y. *et al.* Creating a Nanospace under an h-BN Cover for Adlayer Growth on Nickel(111). *ACS Nano* **9**, 11589–11598 (2015) (page 25).
96. Gómez Díaz, J. *et al.* Hexagonal boron nitride on transition metal surfaces. *Theoretical Chemistry Accounts* **132**, 1–17 (2013) (pages 25, 33, 34, 44).
97. Greber, T., Corso, M. & Osterwalder, J. Fermi surfaces of single layer dielectrics on transition metals. *Surface Science* **603**, 1373–1377 (2009) (pages 25, 34, 35).
98. Lagoute, J., Kanisawa, K. & Fölsch, S. Manipulation and adsorption-site mapping of single pentacene molecules on Cu(111). *Physical Review B - Condensed Matter and Materials Physics* **70**, 1–6 (2004) (pages 30, 89).
99. Tautz, F. S. Structure and bonding of large aromatic molecules on noble metal surfaces: The example of PTCDA. *Progress in Surface Science* **82**, 479–520 (2007) (pages 30, 89).
100. Gross, L. *et al.* High-resolution molecular orbital imaging using a p-wave STM tip. *Physical Review Letters* **107**, 1–4 (2011) (pages 31, 97).
101. Briegleb, G. Electron Affinity of Organic Molecules. *Angewandte Chemie International Edition in English* **3**, 617–632 (1964) (pages 33, 34).
102. Ishii, H., Sugiyama, K., Ito, E & Seki, K. Energy level alignment and interfacial electronic structures at organic/metal and organic/organic interfaces. *Advanced Materials* **11**, 605–625 (1999) (pages 33, 34).
103. Wandelt, K. *Thin Metal Films and Gas Chemisorption* 1987 (pages 33, 34).
104. Dweydari, A. W. & Mee, C. H. B. Work function measurements on (100) and (110) surfaces of silver. *Physica Status Solidi (a)* **27**, 223–230 (1975) (page 33).



- 
105. Vitali, L. *et al.* Portrait of the potential barrier at metal-organic nanocontacts. *Nature materials* **9**, 320–323 (2010) (page 33).
  106. Ruffieux, P. *et al.* Mapping the electronic surface potential of nanostructured surfaces. *Physical Review Letters* **102**, 086807 (2009) (page 33).
  107. Ploigt, H. C., Brun, C., Pivetta, M., Patthey, F. & Schneider, W. D. Local work function changes determined by field emission resonances: NaCl/Ag (100). *Physical Review B - Condensed Matter and Materials Physics* **76**, 1–5 (2007) (pages 33, 34, 45).
  108. Borca, B. *et al.* Potential energy landscape for hot electrons in periodically nanostructured graphene. *Physical Review Letters* **105**, 036804 (2010) (pages 33, 46, 48).
  109. Park, Y., Choong, V., Gao, Y., Hsieh, B. R. & Tang, C. W. Work function of indium tin oxide transparent conductor measured by photoelectron spectroscopy. *Applied Physics Letters* **68**, 2699–2701 (1996) (page 34).
  110. Nonnenmacher, M., O’Boyle, M. P. & Wickramasinghe, H. K. Kelvin probe force microscopy. *Applied Physics Letters* **58**, 2921–2923 (1991) (pages 34, 111).
  111. Soe, W. H., Manzano, C., De Sarkar, A., Chandrasekhar, N. & Joachim, C. Direct observation of molecular orbitals of pentacene physisorbed on Au(111) by scanning tunneling microscope. *Physical Review Letters* **102**, 100–103 (2009) (pages 34, 63, 75).
  112. Neaton, J. B., Hybertsen, M. S. & Louie, S. G. Renormalization of molecular electronic levels at metal-molecule interfaces. *Physical Review Letters* **97**, 216405 (2006) (page 34).
  113. Willenbockel, M. *et al.* The interplay between interface structure, energy level alignment and chemical bonding strength at organic-metal interfaces. en. *Physical Chemistry Chemical Physics: PCCP* **17**, 1530–1548 (2014) (pages 34–37, 67).
  114. Kim, K. K. *et al.* Synthesis and characterization of hexagonal boron nitride film as a dielectric layer for graphene devices. *ACS Nano* **6**, 8583–8590 (2012) (page 34).
  115. Fölsch, S., Helms, A. & Rieder, K. H. Epitaxy of ionic insulators on a vicinal metal substrate: KCl and RbI on Cu(211). *Applied Surface Science* **162**, 270–274 (2000) (page 35).
  116. Smith, D. A. & Mura, M. E. Polarizability of Molecular Orbitals. *The Journal of Physical Chemistry* **98**, 6903–6905 (1994) (page 37).
  117. Herden, T. *Combined Scanning Tunneling and Atomic Force Microscopy and Spectroscopy on Molecular Nanostructures* PhD thesis (Universitaet Konstanz, 2014), 1–5. arXiv: arXiv:1011.1669v3 (page 41).

## Bibliography

---

118. Liu, M. *et al.* Thinning segregated graphene layers on high carbon solubility substrates of rhodium foils by tuning the quenching process. *ACS Nano* **6**, 10581–10589 (2012) (page 41).
119. Franke, P., Neuschütz, D. & (SGTE), S. G.T. E. in *Binary Systems. Part 5: Binary Systems Supplement 1* 1–3 (Springer Berlin Heidelberg, Berlin, Heidelberg) (page 41).
120. Ooi, N., Rairkar, A., Lindsley, L. & Adams, J. B. Electronic structure and bonding in hexagonal boron nitride. *Journal of Physics: Condensed Matter* **18**, 97 (2006) (page 42).
121. Brugger, T. *et al.* Nanotexture switching of single-layer hexagonal boron nitride on rhodium by intercalation of hydrogen atoms. *Angewandte Chemie - International Edition* **49**, 6120–6124 (2010) (page 43).
122. Cun, H., Iannuzzi, M., Hemmi, A., Osterwalder, J. & Greber, T. Two-nanometer voids in single-layer hexagonal boron nitride: Formation via the "can-opener" effect and annihilation by self-healing. *ACS Nano* **8**, 7423–7431 (2014) (page 43).
123. Echenique, P. M., Flores, F. & Sols, F. Lifetime of image surface states. *Physical Review Letters* **55**, 2348–2350 (1985) (page 44).
124. Echenique, P. M. & Uranga, M. E. Image potential states at surfaces. *Surface Science* **247**, 125–132 (1991) (page 45).
125. Schubert, K. *et al.* Momentum-resolved electron dynamics of image-potential states on Cu and Ag surfaces. *Physical Review B - Condensed Matter and Materials Physics* **85**, 205431 (2012) (page 45).
126. Dose, V., Altmann, W., Goldmann, A., Kolac, U. & Rogozik, J. Image-potential states observed by inverse photoemission. *Physical Review Letters* **52**, 1919–1921 (1984) (page 45).
127. Garcia, N., Reihl, B., Frank, K. H. & Williams, A. R. Image states: Binding energies, effective masses, and surface corrugation. *Physical Review Letters* **54**, 591–594 (1985) (page 45).
128. Crampin, S. Lifetimes of stark-shifted image states. *Physical Review Letters* **95**, 046801 (2005) (page 45).
129. Binnig, G. *et al.* Tunneling spectroscopy and inverse photoemission: Image and field states. *Physical Review Letters* **55**, 991–994 (1985) (page 45).
130. Rosenblatt, D. P. *Construction of a low temperature STM and studies of large molecular systems* PAR PhD thesis (École Polytechnique Fédérale de Lausanne, 2016) (pages 46, 47).

131. Iannuzzi, M. & Hutter, J. Comparative study of the nature of chemical bonding of corrugated graphene on Ru(0001) and Rh(111) by electronic structure calculations. *Surface Science* **605**, 1360–1368 (2011) (page 48).
132. Van der Heide, P. *W-Ray Photoelectron Spectroscopy - An Introduction to Principles and Practices* (Wiley-Blackwell, 2012) (page 50).
133. Shi, Y. *et al.* Synthesis of few-layer hexagonal boron nitride thin film by chemical vapor deposition. *Nano Letters* **10**, 4134–4139 (2010) (page 50).
134. Díaz, J., Paolicelli, G., Ferrer, S. & Comin, F. Separation of the sp<sup>3</sup> and sp<sup>2</sup> components in the C1s photoemission spectra of amorphous carbon films. *Physical Review B* **54**, 8064–8069 (1996) (page 51).
135. Wang, B., Caffio, M., Bromley, C., Früchtl, H. & Schaub, R. Coupling epitaxy, chemical bonding, and work function at the local scale in transition metal-supported graphene. *ACS Nano* **4**, 5773–5782 (2010) (page 57).
136. Yang, Y. & Wang, C. Single-molecule studies on individual peptides and peptide assemblies on surfaces. *Philosophical transactions. Series A, Mathematical, physical, and engineering sciences* **371**, 20120311 (2013) (page 57).
137. Clarke, A. R. Molecular chaperones in protein folding and translocation. *Current Opinion in Structural Biology* **6**, 43–50 (1996) (page 57).
138. So, C. R. *et al.* Controlling self-assembly of engineered peptides on graphite by rational mutation. *ACS Nano* **6**, 1648–1656 (2012) (pages 57, 108).
139. Atanasoska, L. L., Buchholz, J. C. & Somorjai, G. A. Low-energy electron diffraction study of the surface structures of adsorbed amino acid monolayers and ordered films deposited on copper crystal surfaces. *Surface Science* **72**, 189–207 (1978) (pages 57, 64).
140. Barlow, S. M. & Raval, R. Complex organic molecules at metal surfaces: Bonding, organisation and chirality. *Surface Science Reports* **50**, 201–341 (2003) (pages 57, 59).
141. Forster, M., Dyer, M. S., Persson, M. & Raval, R. 2D random organization of racemic amino acid monolayers driven by nanoscale adsorption footprints: proline on Cu(110). *Angewandte Chemie (International ed. in English)* **49**, 2344–2348 (2010) (page 57).
142. Naitabdi, A. & Humblot, V. Chiral self-assemblies of amino-acid molecules: D- and L-methionine on Au(111) surface. *Applied Physics Letters* **97** (2010) (page 57).
143. Yitamben, E. N., Clayborne, A, Darling, S. B. & Guisinger, N. P. L-Tryptophan on Cu(111): engineering a molecular labyrinth driven by indole groups. *en. Nanotechnology* **26**, 235604 (2015) (pages 57, 63, 64, 67, 69, 70, 80).

## Bibliography

---

144. Rahsepar, F. R., Moghimi, N. & Leung, K. T. Surface-Mediated Hydrogen Bonding of Proteinogenic alpha-Amino Acids on Silicon. *Accounts of Chemical Research* **49**, 942–951 (2016) (page 57).
145. Ghiringhelli, L. M. & Delle Site, L. Phenylalanine near inorganic surfaces: Conformational statistics vs specific chemistry. *Journal of the American Chemical Society* **130**, 2634–2638 (2008) (pages 58, 80, 89).
146. Forster, M., Dyer, M. S., Persson, M. & Raval, R. Probing conformers and adsorption footprints at the single-molecule level in a highly organized amino acid assembly of (S)-proline on Cu(110). *Journal of the American Chemical Society* **131**, 10173–10181 (2009) (pages 59, 69, 71).
147. Hammer, B. & Norskov, J. K. *Why gold is the noblest of all the metals* 1995 (pages 60, 63).
148. Lutz, T. *et al.* Molecular orbital gates for plasmon excitation. *Nano Letters* **13**, 2846–2850 (2013) (page 61).
149. Altman, E. I. & Colton, R. J. Nucleation, growth, and structure of fullerene films on Au(111). *Surface Science* **279**, 49–67 (1992) (pages 61, 70, 72).
150. Chan, D. I., Prenner, E. J. & Vogel, H. J. Tryptophan- and arginine-rich antimicrobial peptides: Structures and mechanisms of action. *Biochimica et Biophysica Acta - Biomembranes* **1758**, 1184–1202 (2006) (pages 63, 75).
151. Schiffer, M., Chang, C. H. & Stevens, F. J. The functions of Trp residues in membrane proteins. *Prot. Engin.* **5**, 213–214 (1992) (page 63).
152. Zhao, X., Wang, H., Zhao, R. G. & Yang, W. S. Self-assembly of amino acids on the Cu(001) surface. *Materials Science and Engineering C* **16**, 41–50 (2001) (pages 63, 64).
153. Joshi, P. *et al.* Tryptophan-gold nanoparticle interaction: A first-principles quantum mechanical study. *Journal of Physical Chemistry C* **115**, 22818–22826 (2011) (pages 64, 67).
154. Davis, L. C., Everson, M. P., Jaklevic, R. C. & Shen, W. Theory of the local density of surface states on a metal: Comparison with scanning tunneling spectroscopy of a Au(111) surface. *Physical Review B* **43**, 3821–3830 (1991) (page 66).
155. Seljamäe-Green, R. T. *et al.* Assembly of a chiral amino acid on an unreactive surface: (S)-proline on Au(111). *Langmuir* **30**, 3495–3501 (2014) (pages 69, 71, 72).
156. Shi, L. *et al.* Ion Mobility-Mass Spectrometry Reveals the Energetics of Intermediates that Guide Polyproline Folding. *Journal of the American Society for Mass Spectrometry* **27**, 22–30 (2016) (pages 71, 80).

157. Schimmel, P. R. & Flory, P. J. Conformational energy and configurational statistics of poly-L-proline. *Chemistry* **58**, 52–59 (1967) (page 71).
158. Williamson, M. P. The structure and function of proline-rich regions in proteins. *Biochemical Journal* **297**, 249–260 (1994) (page 71).
159. Ma, K., Kan, L. S. & Wang, K. Polyproline II helix is a key structural motif of the elastic PEVK segment of titin. *Biochemistry* **40**, 3427–3438 (2001) (pages 71, 80).
160. Youn, Y. S. *et al.* Stereoselective attachment via N dative bonding: S-proline on Ge(100). *Journal of Physical Chemistry C* **115**, 710–713 (2011) (page 71).
161. Heimel, G. *et al.* Charged and metallic molecular monolayers through surface-induced aromatic stabilization. *Nature Chemistry* **5**, 187–194 (2013) (pages 75, 108).
162. Lagoute, J. & Fölsch, S. Interaction of single pentacene molecules with monatomic Cu Cu(111) quantum wires. *Journal of Vacuum Science & Technology B* **23**, 1726–1731 (2005) (page 75).
163. Seeman, N. C. Nucleic acid junctions and lattices. *Journal of Theoretical Biology* **99**, 237–247 (1982) (page 77).
164. Seeman, N. C. DNA in a material world. *Nature* **421**, 427–431 (2003) (page 77).
165. Krivov, S. V. & Karplus, M. Hidden complexity of free energy surfaces for peptide (protein) folding. *Proceedings of the National Academy of Sciences of the United States of America* **101**, 14766–70 (2004) (page 77).
166. R.B., M. Solid Phase Peptide Synthesis. I. The Synthesis of. *Journal of American Chemical Society* **85**, 2149–2154 (1963) (page 77).
167. Coin, I., Beyermann, M. & Bienert, M. Solid-phase peptide synthesis: from standard procedures to the synthesis of difficult sequences. *Nature Protocols* **2**, 3247–3256 (2007) (page 77).
168. Gazit, E. Self-assembled peptide nanostructures: the design of molecular building blocks and their technological utilization. *Chemical Society Reviews* **36**, 1263 (2007) (page 78).
169. Kim, S., Kim, J. H., Lee, J. S. & Park, C. B. *Beta-Sheet-Forming, Self-Assembled Peptide Nanomaterials towards Optical, Energy, and Healthcare Applications* 2015 (page 78).
170. Matson, J. B. & Stupp, S. I. Self-assembling peptide scaffolds for regenerative medicine. *Chem. Commun.* **48**, 26 (2012) (page 78).

## Bibliography

---

171. Ghadiri, M. R., Granja, J. R., Milligan, R. A., McRee, D. E. & Khazanovich, N. Self-assembling organic nanotubes based on a cyclic peptide architecture. *Nature* **366**, 324–327 (1993) (page 78).
172. Frederix, P. W. J. M. *et al.* Exploring the sequence space for (tri-)peptide self-assembly to design and discover new hydrogels. *Nature Chemistry* **7**, 30–37 (2014) (page 78).
173. Mann, S. *Biomimetic materials chemistry* 383 (VCH, 1996) (page 78).
174. Hlady, V. & Buijs, J. Protein adsorption on solid surfaces. *Current Opinion in Biotechnology* **7**, 72–77 (1996) (page 78).
175. Dupont-Gillain, C. *Proteins at Interfaces III State of the Art 2012* (eds Horbett, T., Brash, J. L. & Norde, W.) 453–469 (American Chemical Society, Washington, DC, 2012) (page 78).
176. Claridge, S. A. *et al.* Differentiating amino acid residues and side chain orientations in peptides using scanning tunneling microscopy. *Journal of the American Chemical Society* **135**, 18528–18535 (2013) (page 78).
177. So, C. R. *et al.* Molecular recognition and supramolecular self-assembly of a genetically engineered gold binding peptide on Au{111}. *ACS Nano* **3**, 1525–1531 (2009) (pages 78, 108).
178. Barth, J. V. Molecular architectonic on metal surfaces. *Annual review of physical chemistry* **58**, 375–407 (2007) (page 81).
179. Mamdouh, W., Mingdong, D., Kelly, R. E. A., Kantorovich, L. N. & Besenbacher, F. Coexistence of homochiral and heterochiral adenine domains at the liquid/solid interface. *Journal of Physical Chemistry B* **111**, 12048–12052 (2007) (page 81).
180. Elemans, J., Lei, S. & DeFeyter, S. Molecular and Supramolecular Networks on Surfaces: From Two-Dimensional Crystal Engineering to Reactivity. *Angewandte Chemie International Edition* **48**, 7298–7332 (2009) (page 81).
181. Wolynes, P. G. Biomolecular folding in vacuo!!!(?) *Proceedings of the National Academy of Sciences of the United States of America* **92**, 2426–2427 (1995) (pages 83, 108).
182. Hoeffling, M., Iori, F., Corni, S. & Gottschalk, K.-E. The conformations of amino acids on a gold(111) surface. *Chemphyschem : a European journal of chemical physics and physical chemistry* **11**, 1763–1767 (2010) (pages 89, 90).
183. Wanner, J., Kompa, K. L., Mueller, A. M., Witzel, B. & Uiterwaal, C. J. White-light-induced fragmentation of toluene. *Physical Review Letters* **88**, 230011–230014 (2002) (page 89).
184. Heimel, G. *et al.* Charged and metallic molecular monolayers through surface-induced aromatic stabilization. *Nature Chemistry* **5**, 187–194 (2013) (page 89).

185. Dougherty, D. a. Cation- $\pi$  interactions in chemistry and biology: a new view of benzene, Phe, Tyr, and Trp. *Science (New York, N.Y.)* **271**, 163–168 (1996) (page 92).
186. Mitchell, J. B., Nandi, C. L., McDonald, I. K., Thornton, J. M. & Price, S. L. Amino/aromatic interactions in proteins: is the evidence stacked against hydrogen bonding? *Journal of molecular biology* **239**, 315–31 (1994) (page 92).
187. Burley, S. & Petsko, G. in, 125–189 (1988) (page 92).
188. Chen, L. *et al.* Mechanism for negative differential resistance in molecular electronic devices: Local orbital symmetry matching. *Physical Review Letters* **99**, 1–4 (2007) (page 97).
189. Tanaka, H. & Kawai, T. Partial sequencing of a single DNA molecule with a scanning tunnelling microscope. *Nature nanotechnology* **4**, 518–522 (2009) (page 97).
190. Van der Vegte, E. W. & Hadziioannou, G. Scanning Force Microscopy with Chemical Specificity: An Extensive Study of Chemically Specific Tip Surface Interactions and the Chemical Imaging of Surface Functional Groups. *Langmuir* **13**, 4357–4368 (1997) (page 97).
191. Tanaka, H. & Kawai, T. Partial sequencing of a single DNA molecule with a scanning tunnelling microscope. *Nature nanotechnology* **4**, 518–522 (2009) (page 97).
192. Nojima, Y., Tanaka, H., Yoshida, Y. & Kawai, T. High-Resolution Scanning Tunneling Microscopy and Spectroscopy Studies of Deoxyribonucleic Acid and Fluorescein Isothiocyanate. *Japanese Journal of Applied Physics* **43**, 5526–5527 (2004) (page 97).
193. He, J., Lin, L., Zhang, P. & Lindsay, S. Identification of DNA basepairing via tunnel-current decay. *Nano Letters* **7**, 3854–3858 (2007) (page 97).
194. Di Ventra, M. & Taniguchi, M. Decoding {DNA}, {RNA} and peptides with quantum tunnelling. *Nature Nanotechnology* **11**, 117–126 (2016) (page 97).
195. Mohn, F., Schuler, B., Gross, L. & Meyer, G. Different tips for high-resolution atomic force microscopy and scanning tunneling microscopy of single molecules. *Applied Physics Letters* **102**, 073109 (2013) (page 97).
196. Yanov, I., Palacios, J. J. & Hill, G. Simple STM tip functionalization for rapid DNA sequencing: An ab initio green's function study. *Journal of Physical Chemistry A* **112**, 2069–2073 (2008) (page 97).
197. Yu, X., Wang, Z., Su, Z. & Wei, G. Design, fabrication, and biomedical applications of bioinspired peptide–inorganic nanomaterial hybrids. *J. Mater. Chem. B* **5**, 1130–1142 (2017) (page 107).

## Bibliography

---

198. Praetorius, F. & Dietz, H. Self-assembly of genetically encoded DNA-protein hybrid nanoscale shapes. *Science* **355** (2017) (page 107).
199. Abb, S. *Molecular Imaging of Biopolymers enabled by Electrospray Ion-Beam Deposition* PhD thesis (2017) (page 109).
200. Giessibl, F. J. \* REPORTS Surface by Atomic Force Microscopy. *Science* **267**, 68–71 (2013) (page 110).
201. Gross, L., Mohn, F., Moll, N., Liljeroth, P. & Meyer, G. The Chemical Structure of a Molecule Resolved by Atomic Force Microscopy. *Science* **325**, 1110–1114 (2009) (page 111).
202. Albrecht, F., Neu, M., Quest, C., Swart, I. & Repp, J. Formation and characterization of a molecule-metal-molecule bridge in real space. *Journal of the American Chemical Society* **135**, 9200–9203 (2013) (page 111).
203. Giessibl, F. J., Hembacher, S., Herz, M., Schiller, C. & Mannhart, J. Stability considerations and implementation of cantilevers allowing dynamic force microscopy with optimal resolution: the qPlus sensor. *Nanotechnology* **15**, S79–S86 (2004) (page 110).
204. Zhang, C., Feng, X., Cui, K. & Huang, Y. Plasmonic enhancement of spontaneous emission from wide-linewidth emitters with nanostrip metallic waveguide. *Journal of Applied Physics* **114** (2013) (page 110).
205. Schuler, B. *et al.* Contrast formation in Kelvin probe force microscopy of single pi-conjugated molecules. *Nano Letters* **14**, 3342–3346 (2014) (page 110).
206. Albrecht, F., Bischoff, F., Auwärter, W., Barth, J. V. & Repp, J. Direct Identification and Determination of Conformational Response in Adsorbed Individual Nonplanar Molecular Species Using Noncontact Atomic Force Microscopy. *Nano Letters* **16**, 1–3 (2016) (page 111).
207. Albrecht, F. *et al.* Probing Charges on the Atomic Scale by Means of Atomic Force Microscopy. *Physical Review Letters* **115**, 076101 (2015) (page 111).



## Personal Details

Name: Sebastian Koslowski  
Date of birth: 10.10.1987  
Address: Burgstrasse 31, 70569 Stuttgart

## Education

Present  
- 01/2014      **Dr. Sc. Physics**, *Ecole-Polytechnique-Federale de Lausanne (EPFL)*, Lausanne, Switzerland  
Group: Prof. Klaus Kern

01/2014 - present  
Student of the international Max-Planck-EPFL center for molecular nanosciences and technology

12/2012  
- 06/2010      **Master studies (M.Sc. (Physics))**, *Justus-Liebig-Universität, Giessen*,  
12/2011 - 12/2012  
**Masters thesis**, *Justus-Liebig-Universität Giessen*  
Group: Prof. Martin Eickhoff  
**Topic:** Development of opto-chemical sensors based on nanostructured semiconductor materials to probe the activity of biological systems

07/2011 - 10/2011  
**Stay abroad**, *University of Utah, Salt Lake City, USA*  
Group: Prof. Florian Solzbacher  
**Topic:** Optimization of the coating process of electrodes for neuronal implants

06/2010  
- 10/2007      **Bachelor studies (B.Sc. (Physics))**, *Justus-Liebig-Universität, Giessen*  
03/2010 - 06/2010  
**Bachelor Thesis**, *Justus-Liebig-Universität Giessen*  
Group: Prof. Martin Eickhoff  
**Topic:** Electrochemical sensors for harsh environments

07/2007      **Highschool entrance diploma**, *Willhelm-von-Oranien Schule, Dillenburg, Germany*

## **Publications**

**Koslowski, S.**, Rosenblatt D., Kabakchiev, A., Kuhnke, K., Kern, K., Schlickum, U.

Pentacene adsorption and electronic properties on thin dielectric decoupling layers

Submitted to: Beilstein Journal of Nanotechnology (2017)

Teubert, J., **Koslowski, S.**, Lippert, S., Schäfer, M., Wallys, J., Dimitrakopulos, G., Kehagias Th., Komninou Ph., Das A., Monroy E. *and* Eickhoff, M.

InGaN/GaN quantum dots as optical probes for the electric field at the GaN/electrolyte interface

*Journal of Applied Physics*, **114**, 074313 (2013)